# OLFACTORY INPUTS MODULATE RESPIRATION-RELATED ACTIVITY IN THE PREFRONTAL CORTEX AND FEAR BEHAVIOR

Andrew Henry Moberly

A DISSERTATION

in

Neuroscience

Presented to the Faculties of the University of Pennsylvania

in

Partial Fulfillment of the Requirements for the

Degree of Doctor of Philosophy

2018

**Supervisor of Dissertation:**

_____

Minghong Ma

Professor of Neuroscience

**Graduate Group Chairperson:**

_____

Joshua Gold

Professor of Neuroscience

**Dissertation Committee:**

Marc F Schmidt, Professor of Biology (Committee Chair)

Wenqin Luo, Associate Professor of Neuroscience

Jay A Gottfried, Professor of Neurology

ACKOWLEDGEMENTS

My advisor, Dr. **Minghong Ma,** provided me with immeasurable support over the course of my doctoral studies. More than anyone, she has shaped how I think about the brain and the scientific questions we need to ask in our efforts to understand it. As a mentor, she valued independent, creative, critical thinking above all. She gave me the freedom to pursue interesting scientific questions and, with an incredible degree of patience, ensured that we learned as much from our failures as from our successes. I couldn't ask for a better scientific role model and I would be happy to achieve even a modicum of the respect she garners from the entire neuroscience community.

I would like to thank my thesis committee: Drs. **Marc Schmidt**, **Diego Contreras**, **Jay Gottfried**, and **Wenqin Luo**. Their intellectual input has been incredibly helpful and I am grateful for the support they provided over the course of my thesis work. Our collaboration with Wenqin deserves a special mention; I benefited greatly from Wenqin's expertise thanks to the synergistic partnership between the Ma and Luo labs.

I am deeply thankful to the past members of the Ma lab including Drs. **Rosemary Challis** and **Yiqun Yu**, and the visiting students **Shaohau Zhao**, **Wenbin Yin**, **Liujing Zhuang**, and **Julia Mohrhardt**. Without their contributions this work would not have been possible. The current members of the Ma lab were instrumental in generating and analyzing data that are presented here including **Mary Schreck**, **Emma Janke**, and Drs. **Janardhan Bhattarai**, and **Yun-Feng Zhang**. As I mentioned above, I was lucky to receive assistance from many members of the Luo lab and I would like to specifically thank Drs. **Will Olsen**, **Kim Kridsada-Chu**, **Lian Ciu**, and **Ishmail Abdus-Saboor** for

their help and feedback over the years. I thank the veterinary staff and ULAR for providing the essential infrastructure for animal research at Penn. Thanks are also due to the experimental subjects for their contribution to this research.

It was an incredible privilege to be part of the Neuroscience Graduate Group at the University of Pennsylvania. I thank the individuals that tirelessly ensure the program produces exceptional research scientists. This includes the program coordinators past and present: **Jane Hoshi**, **Christine Clay**, and **Tom Hindman**, the program chair Dr. **Josh Gold**, and the many faculty members who dedicate their time to teaching Cores II, and III. The program is strong because it attracts talented, hardworking, brilliant students – many of whom I am proud to call my friends. I thank Drs. **Peter Dong**, **Greg Artiushin**, **Sarah Maguire**, **Kamesh Krishnamurthy**, **Chris Angelakos**, and **Preetika Gupta** for sharing their companionship, rapport, and countless laughs with me throughout my time in the neuroscience program. I also have to thank my partner **Jennifer Blackwell** who has been my constant companion through grad school. When we first met I was in awe of how intelligent and true-to-herself she was. Later, I learned she compliments me well because she is willing to kill the bugs that make it into the apartment.

My path to neuroscience research began when I signed up for a required undergraduate elective with the dubious placeholder title of: 'Advanced Topics in Psychobiology'. Luckily, it turned out to be a course called 'The Neuroscience of Smell' taught by Dr. **John McGann**. As a new faculty member in the department of Behavioral Neuroscience John gave me the opportunity to work in his lab doing state-of-the-art brain research, for which I am forever grateful. John's students were Drs. **Lindsey Czarnecki** and **Marley Kass** who became my first graduate student role models. Throughout

graduate school I have strived to follow in their footsteps and use their work-ethic and passion for science to guide my own research. I thank them for everything they taught me.

Of course, anything I have managed to achieve is entirely due to the love of my parents, **Linh and Jim Moberly** and sister **Alyssa Moberly**. Words do not suffice in thanking my family for their encouragement and support and I do my best to make them proud every day. Although it may be cliché, I'd like to invoke Newton's expression, "If I have seen further it is by standing on the shoulders of giants", and give my deepest thanks to all of the giants who have supported me.

ABSTRACT

OLFACTORY INPUTS MODULATE RESPIRATION-RELATED ACTIVITY IN THE PREFRONTAL CORTEX AND FEAR BEHAVIOR

Andrew H Moberly

Minghong Ma

Voluntary control of respiration, especially via rhythmic nasal breathing, alleviates negative feelings such as fear and is used clinically to manage certain types of panic attacks. However, the neural substrates that link nasal breathing to fear circuits remains unknown. Here we show that during conditioned fear-induced freezing behavior, mice breathe at a steady rate (~4 Hz) which is strongly correlated with a predominant 4 Hz oscillation observed in the olfactory bulb and the prelimbic prefrontal cortex (plPFC), a structure critical for the expression of conditioned fear behaviors. We demonstrate anatomical and functional connectivity between the olfactory pathway and plPFC via circuit tracing and optogenetic approaches. Disrupting olfactory inputs significantly reduces the 4 Hz oscillation in the plPFC suggesting that respiration-related signals from the olfactory system play a role in entraining this fear-related signal. Surprisingly, we find that without olfactory inputs, freezing times are significantly prolonged. Collectively, our results indicate that olfactory inputs modulate rhythmic activity in fear circuits and suggest a neural pathway that may underlie the behavioral benefits of respiration-entrained olfactory signals.

TABLE OF CONTENTS

## LIST OF TABLES

**LIST OF FIGURES**

# CHAPTER 1: INTRODUCTION

## The breathing rhythm

The respiratory rhythm persists throughout life, serving to regulate gas exchange, adjust pH and maintain homeostasis. Cycle-by-cycle control of breathing is initiated by intrinsically rhythmic pacemaker neurons in the brainstem that control descending drive to motoneurons. Accordingly, the cellular oscillators responsible for the breathing rhythm can persist in thin brainstem slices that include the ventrolateral medulla, specifically the preBötzinger Complex (Feldman et al., 2003; Feldman et al., 2013; Del Negro et al., 2018). Humans and other mammals generate distinct breathing patterns including eupnea (resting breathing), tachypnea (rapid breathing), apnea (breath-holding), gasping, and sighing. Correlates of these motor outputs are generated by cells in the preBötzinger with overlapping sets of neurons active during each type of rhythm (Kam et al., 2013). Since respiratory rhythms are remarkably dynamic they are necessarily influenced by a host of factors in order to capture the full repertoire of respiratory behavior (for example, changes in respiratory frequency and depth during sleep-wake, rest-exercise, and panic-calm states). These factors include physiological demands such as increased metabolic load, but also include *cognitive and emotional influences* (Bloch et al., 1991; Boiten et al., 1994; Boiten, 1998).

Historically, the link between emotion and respiration has been broadly divided into a few domains. *1*) Do distinct emotional states have characteristic breathing patterns? *2*) Can breathing patterns be used as a clinical diagnostic tool? (For example, apneas are associated with significant comorbidity including hypertension, insomnia, and

depression). *3*) Does conscious control of breathing affect mood? In support of the last point, it is commonly observed that patterns of slow and deep respiration are encountered in relaxed and restful states. Furthermore, various techniques that involve slow, deep nasal breathing such as yoga, *pranayama*, and other forms of mediation have been practiced throughout history to encourage physical and emotional well-being (Brown and Gerbarg, 2009; Jerath et al., 2015). Voluntarily-controlled, slow nasal breathing improves cognitive performance and reduces stress in adults and target patient populations even when it is used alone – that is, not just as a component of mindfulness, mediation, or yoga practice (Ma et al., 2017). On the other hand, fast, irregular breathing patterns, especially in the context of respiratory challenges, can induce panic attacks especially in patients with panic disorders (Nardi et al., 2004; Meuret et al., 2005).

A recently discovered excitatory pathway from a small subset of *Cdh9/Dbx1*-expressing neurons in the preBötzinger Complex to the locus coeruleus (LC) is one mechanism by which autonomic breathing influences higher brain regions (Yackle et al., 2017; Melnychuk et al., 2018). Since the LC is involved in attention and arousal and has extensive targets throughout the cortex, increased excitatory input from inspiration-related preBötC neurons during fast or irregular breathing could result in increased arousal and changes in neural activity throughout the brain (Loughlin et al., 1986). The connectivity between higher brain centers and brainstem breathing pacemakers is likely to be bidirectional. As evidence, electrically stimulating the amygdala, a limbic system structure essential for emotion, influences respiratory rates. Specifically, stimulation of the central nucleus of the amygdala increases respiratory rate in alert, awake cats but not in asleep animals (Harper et al., 1984; Masaoka and Homma, 2004). Direct amygdala

stimulation also effects human respiration but in these cases causes apneas as opposed to entraining breathing (Nobis et al., 2018).

From these lines of study, an emerging hypothesis is that the *breathing rhythm itself exerts a meaningful influence on emotion and cognition* (Philippot et al., 2002; Homma and Masaoka, 2008). One mechanism could be the direct influence of brainstem pacemaker centers on neuromodulatory or higher brain regions as seems to be the case with respiratory inputs that reach the LC. A complimentary way that the breathing rhythm could influence brain activity is via *breathing-related sensory signals* originating from the peripheral olfactory system. A sensory copy of the breathing rhythm propagates through the olfactory system and reaches downstream brain regions including limbic areas involved in emotion and memory (Zald and Pardo, 1997). A major goal for the field (and this thesis) is to determine the extent to which breathing signals influence neural activity and contribute to emotional processing.

### The olfactory periphery and the sensation of breathing

One neural substrate by which the breathing rhythm effects the neural circuits involved in emotion is likely to be signals originating from the sensation of nasal breathing. The neurons in the nasal epithelium, olfactory sensory neurons (OSNs), that signal the binding of odorants are intrinsically mechanosensitive and capable of representing the breathing signal even in the absence of explicit odorant stimulation (Ueki and Domino, 1961; Grosmaitre et al., 2007; Connelly et al., 2015). Nearly half of OSNs in an *ex vivo* mouse epithelial preparation respond to mechanical stimuli (i.e. puffs of odorant free Ringer's solution) delivered at low frequencies up to a maximum

frequency of 0.5 Hz. So, individual OSNs are unlikely to follow the full range of breathing rates which can be as fast as 12 Hz during sniffing bouts. Fortunately, there are about 20 million OSNs in the nasal epithelium converging onto about 2000 OB glomeruli (Moriya-Ito et al., 2015). So at the population level OSNs can represent the full range of breathing frequencies – even if only subsets become activated during a given portion of the breathing cycle. Under *in vivo* physiological conditions, OSNs are also activated by airflow (Iwata et al., 2017; Wu et al., 2017).

Rhythmic, odor-independent activation of OSNs contributes to oscillatory activity downstream of the nasal epithelium. OSNs send axonal projections to the olfactory bulb (OB) in the forebrain where OSNs that express the same olfactory receptor type converge onto one or two roughly spherical structures called glomeruli. Olfactory glomeruli consist of incoming OSN axons and the apical dendrites of the main projection neurons of the OB: mitral and tufted cells. The transformation of information that takes place between OSNs and bulbar output neurons is complex and mediated by a heterogeneous population of interneurons, but in its simplest form mitral and tufted cells receive inputs from OSNs and in turn project to higher brain areas (Wachowiak and Shipley, 2006). These include the olfactory cortex, the ventral striatum, and components of the limbic system. Note that unlike other sensory systems there is no thalamic relay between the olfactory bulb and olfactory cortex (Haberly and Price, 1977). Direct olfactory projections to the amygdala and entorhinal cortex are hypothesized to support the ability of odors to evoke particularly strong feelings and memories – the so-called Proust Phenomenon, named after the French novelist who described experiencing long-lost childhood memories following an odor stimulus. We propose that since OSNs are rhythmically activated by

airflow, the breathing rhythm itself can influence limbic circuits via a reafferent signal sensed by the periphery and propagated throughout the brain (**Figure 1.1**).

### Rhythmic, breathing-related in the olfactory pathway

In nervous tissue, transmembrane currents contribute to extracellular fields that can be recorded at different scales, from single units to spatially distributed populations (Buzsaki et al., 2012). Oscillations are ubiquitous in neurophysiological systems and are routinely interrogated at all of these scales. Most of the work described here employs population-level measures such as the electroencephalogram (EEG) or local field potential (LFP). The LFP signal recorded from an implanted microelectrode reflects the overall synaptic activity of the local neuronal populations and can be characterized using a classification scheme that takes into account the dominant frequency of the signal (Kajikawa and Schroeder, 2011). Historically, the classification of brain rhythms was driven by clinical considerations. As such, distinctions between frequency bands were drawn before much was known about the mechanisms that contribute to them. The internationally agreed characterization using in clinical neurophysiology is: delta (0.1-3.5 Hz), theta (4-7.5 Hz), alpha (8-13 Hz), beta (14-30 Hz), and gamma (>30 Hz). There exist other identified frequencies ranging from infraslow to ultrafast over four orders of magnitude and the spectral features of these rhythms are similar across mammals, regardless of brain size (Buzsaki et al., 2013; Cole and Voytek, 2017).

Using measures of synchrony at the network level we can ask: to what extent is rhythmic activity in the brain organized by breathing? Recent studies suggest that the contribution of breathing to neural dynamics has been greatly underappreciated. But

interestingly, rhythmic neural activity related to breathing was observed early in the history of neurophysiology. In 1942 Lord Adrian described waves of activity recorded from the olfactory bulb in the anesthetized hedgehog (Adrian, 1942). He noted that the stimulus producing this activity was simply room-air devoid of any particular "smell distinct enough to be appreciated by the human nose". Instead of being essential for odor coding, Adrian suggested that the rhythmic activity was caused by uniform mechanical stimulation via inhalation. A similar phenomenon was found in EEGs recorded from the bullfrog forebrain (Hobson, 1967). Here too, synchronous waves of activity were evoked by air entering the nasal cavity.

In modern experiments, if extracellular electrodes are implanted in the OB while respiration is simultaneously measured, the most obvious feature of the extracellular signal is a 2-12 Hz oscillation that closely follows breathing (Kay et al., 2009; Rojas-Libano et al., 2014). As suggested, the mechanosensitivity of OSNs in the nose provides a potential substrate by which airflow can entrain the activity of downstream networks to the respiratory rhythm. Theoretically, a coordinated volley of impulses arriving at the OB with each inspiration could modulate gain parameters of the bulbar network which would be reflected in LFP oscillations (Freeman, 1972).

So, if OSNs are rendered unable to detect airflow is the relationship between breathing and oscillatory activity in the olfactory system disrupted? The nucleotide binding subunit of the cyclic-nucleotide gated (CNG) channel is necessary for both odorant signal transduction as well as mechanical responses in OSNs. Targeted deletion of the Cnga2 gene results in general anosmia from the loss of odor evoked signals but also decouples OB-LFPs from respiration (Brunet et al., 1996; Grosmaitre et al., 2007).

Respiration-related neural activity is also documented downstream of the OB (Buonviso et al., 2006). Given that high amplitude, breathing-patterned oscillations dominate the OB it is not surprising that LFPs in the olfactory tubercle, piriform cortex, and mediodorsal thalamus, all of which receive direct input from the OB, are highly correlated with breathing (Fontanini et al., 2003; Fontanini and Bower, 2005; Carlson et al., 2014; Courtiol and Wilson, 2016). In these cases, respiration-related activity is likely to have a peripheral origin because neural activity is decoupled from breathing if nasal airflow is bypassed. Also, in anesthetized, tracheotomized animal preparations, neural activity can be re-entrained to artificial nasal airflow (Onoda and Mori, 1980; Phillips et al., 2012). In our own experiments, the direct role of OSNs in entraining olfactory (and non-olfactory) networks is demonstrated via artificially activating OSNs while simultaneously observing the effects on field activity in various brain regions (see **Chapter 2**).

One interesting question raised by these results is: do breathing related signals confound odor-related signals? Changes in breathing rate inherently produce large signals in many glomeruli via mechanosensory inputs. Does the brain have difficulty interpreting whether increased activity is due to stronger mechanical stimulation (i.e. a deeper breath) or an odorant? Studies suggest that the olfactory system uses a phase-based strategy to readily discriminate between odor and sniff-induced mechanical signals. Odor stimuli but not airflow stimuli produce phase-shifts in sniff-coupled oscillations (Iwata et al., 2017). Under artificial sniffing conditions increased nasal airflow speed does not change the phase of glomerular oscillations. On the other hand, odorants cause phase shifts in ocillatory patterns before and after stimulation. A similar mechanism may be used in the

whisker system to discriminate between self-generated whisking and touch (Severson et al., 2017).

### Breathing-related activity beyond the olfactory system

Recently, several studies have identified signatures of respiration in cortical and subcortical regions that do not receive direct input from the OB (**Table 1.1**). These results suggest that the breathing rhythm is a global signal in the brain, instead of one just subserving olfactory sensory processing. One such region is the rodent hippocampus which has been extensively studied in the context of brain rhythms. Recordings from the rodent hippocampus are dominated by a high amplitude rhythm termed hippocampal 'theta' which has a frequency of 6-8 Hz but whose range has been broadened to include higher frequencies that appear during running and lower frequencies that appear under anesthesia (Vanderwolf, 1969; Hasselmo, 2005). The rhythm is entrained by the medial septal nuclei and sensitive to cholinergic transmission (Buzsaki, 2002; Hasselmo et al., 2002; Vertes et al., 2004). Even though the frequency of hippocampal theta overlaps with the normal breathing rates of rodents, respiration-related signals in the hippocampus are distinct from hippocampal theta. The hippocampal theta rhythm is important for temporally organizing cell ensembles (groups of cells that represent an information processing unit) while the role of the simultaneously present respiratory-rhythm remains largely unknown (Yanovsky et al., 2014; Lockmann et al., 2016; Nguyen Chi et al., 2016). A potential source of respiratory-related activity in the hippocampus is olfactory afferents that target layer I of the entorhinal cortex where they synapse onto the dendrites of layer II/III cells. These in turn project to the hippocampal formation, mainly the

dentate gyrus, which expresses the highest levels of respiratory-coupled activity. The olfactory-hippocampal pathway is implicated in olfactory memory formation and there are reports of synchronization between the OB and hippocampus during sniffing in odor-guided cognitive tasks (Macrides et al., 1982; Kay, 2005; Martin et al., 2007). However, since respiration was not directly monitored in these cases it is unclear which 'theta' range activity (e.g. respiratory-related or hippocampal theta) is becoming synchronized because the OB expresses its own 'theta' that originates from the hippocampus (Nguyen Chi et al., 2016). Respiration-related inputs from the olfactory system also modulate the timing of sharp wave ripple events in the hippocampal network, a network property that is implicated in coordinating cell assemblies during hippocampal playback and memory consolidation (van de Ven et al., 2016; Liu et al., 2017).

But even brain regions further removed from olfactory inputs express respiration-coupled activity. These include the mouse whisker (or barrel) cortex, prefrontal cortex, and orbitofrontal cortex (Ito et al., 2014; Biskamp et al., 2017; Zhong et al., 2017; Koszeghy et al., 2018). The breathing signal in whisker cortex is particularly interesting because rhythmic orofacial motor outputs (including licking) are coordinated in time (Welzl and Bures, 1977; Deschenes et al., 2012). Vibrissa protractions are locked to inspiration across all frequencies of breathing and premotor whisking nuclei in the medulla receive rhythmic drive from the pre-Bötzinger complex (Moore et al., 2013; Kleinfeld et al., 2014a). On the sensory side, an afferent copy of respiratory activity that reaches the whisker cortex (possibly via basal forebrain cholinergic inputs) may be a mechanism that helps to bind somatosensory inputs from the two modalities (Kleinfeld et al., 2014b).

The idea that the respiratory rhythm serves as a "common clock" used to coordinate neural activity across the brain (and especially the cortex) has gained popularity due to a few features of the signal. *1)* It is omnipresent throughout the lifespan of the animal. *2)* The rhythm is widely expressed in cortical and subcortical structures. *3)* It overlaps in frequency with behaviorally relevant features (e.g. whisking and licking). *4)* Its low frequency enables it to organize faster rhythms (Heck et al., 2017; Tort et al., 2018). On this last point, note that the interactions between neural oscillators are often hierarchical; the phase of slower oscillations modulates the power of faster rhythms in a process known as 'cross-frequency coupling' (Sauseng and Klimesch, 2008; Hyafil et al., 2015). For example, hippocampal theta can modulate the power of gamma oscillations in the neocortex (Watson and Buzsaki, 2015). The breathing rhythm similarly modulates the power of gamma oscillations in the barrel cortex and prefrontal cortex (Ito et al., 2014; Biskamp et al., 2017).

Perhaps another advantage of using the sensation of breathing to coordinate brain activity is that the olfactory system rapidly senses the breathing cycle. Mice are able to use breathing phase to distinguish differences in olfactory input of 50 milliseconds (Smear et al., 2011). Changes in respiration rate result in heart-rate and blood pressure modulation that can be sensed by baroreceptors and thus influence EEG activity generated by the cortex (Rau et al., 1993). However, the time scale of these changes in relation to respiration is likely to be slower than those coming from the peripheral olfactory system.

### A proposed functional role for synchronized activity between neural networks

How might low-frequency rhythms coordinate neural activity across distant brain regions? In many networks, cellular excitability is modulated by low frequency rhythms that are imposed by another network or emerge from the intrinsic properties of the network itself (Jensen and Colgin, 2007). Since neurons are robust coincidence detectors, inputs that are in-phase with periods of high membrane excitability are conferred an advantage vs those that arrive out of phase. For example, if high neuronal excitability is associated with the peak of LFP oscillations, inputs time-locked to the peak of the LFP waveform will be processed faster or more efficiently than inputs arriving at the trough. In this manner, slow oscillations can enhance network communication over long distances by biasing spiking probability (Salinas and Sejnowski, 2001; Varela et al., 2001; Voytek and Knight, 2015). Spikes leaving one brain area may arrive at a connected brain area at a time when it is maximally excitable (i.e. spikes are in-phase with ongoing oscillatory activity). On the other hand, a shift in the relative phase of the oscillation could result in spikes arriving when the receiving area is less excitable, decreasing communication efficacy (Canolty and Knight, 2010). To put it another way, for a sender to communicate a message effectively to a receiver, the sender's output should be timed such that it arrives when the receiver is most excitable.

Within this theoretical framework, it has been proposed that specific brain regions become transiently synchronized when communication needs to be facilitated, e.g. during specific behavioral tasks that recruit working or long-term memory, sensory systems, reward pathways, etc. (Benchenane et al., 2010; Benchenane et al., 2011; Fujisawa and Buzsaki, 2011; Schwindel and McNaughton, 2011). This has been conceptualized in

influential theoretical frameworks like the ‘communication through coherence’ hypothesis or the ‘binding by synchrony’ theory (Eckhorn et al., 1990; Engel et al., 1999; Fries, 2005). In experiments explicitly investigating these hypotheses (such as those described below), synchronization, or phase locking, between brain regions is measured by the consistency of the phase relationships (coherence) between extracellular neural signals. These signals can be simultaneously recorded LFPs or extracellular spiking events and field potentials recorded in different regions (spike-field coherence) High coherence has become synonymous with the terms ‘phase-locking’ and ‘synchrony’ (Vinck et al., 2012).

### Synchronized brain networks during specific behavioral states

This proposed theoretical framework is popular in part due to numerous instances where neural activity in specific brain regions becomes transiently synchronized during behavior. The consensus is that the brain uses oscillations to link ongoing neural processes in multiple brain regions utilizing a wide range of frequencies, from less than 1 Hz during sleep to gamma range activity reaching 80-100 Hz that coordinates the activity of small, local networks (Buzsaki and Wang, 2012). In rodents, the hippocampus and medial prefrontal cortex are considered hubs of intra-structure communication. Simultaneous extracellular recordings from these areas in freely behaving animals unequivocally show that frequency-specific synchronization occurs during behavioral and cognitive tasks where information from multiple brain regions must be integrated. For example, in spatial working memory tasks where rats are required to ‘hold in mind’ maze

locations that are rewarded, the hippocampus (CA1) and medial prefrontal cortex express coherent theta-range activity during ‘peak decision-making load’ (Jones and Wilson, 2005). Synchronization at this frequency also occurs between the hippocampus and caudoputamen during decision periods in a T-maze task (DeCoteau et al., 2007; Tort et al., 2008; Benchenane et al., 2010). An extensive study analyzing LFPs acquired simultaneously from the medial prefrontal cortex, hippocampus and ventral tegmental area showed that 4 Hz oscillations (distinct from hippocampal theta) transiently synchronize these regions while rats hold stimuli in working memory (Fujisawa and Buzsaki, 2011). In another delayed non-match to sample working memory task nearly 50% of prefrontal cells were phase locked to hippocampal theta on correct choices compared to less than 20% on error trials. Because the degree of synchronization can be used to predict task performance it suggests that theta-phase locking between these regions serves a functional role in goal-directed behaviors like navigation and working memory. Loss of function experiments show a similar relationship: mice that have difficulty acquiring a delayed-non-match-to-place task have reduced theta-frequency synchronization between prefrontal and hippocampal networks (Tamura et al., 2017).

In human experiments, spatial resolution is oftentimes limited by the use of noninvasive scalp recordings. But in select cases patients undergoing presurgical evaluations for intractable epilepsy are implanted with electrodes that record the intracranial electroencephalogram (iEEG). One such study reported increased theta coherence between electrodes over the prefrontal cortex and medial temporal lobe during a free-recall task compared to baseline conditions (Anderson et al., 2010). Also, in

monkey extrastriate cortex, single units are phase locked to theta range activity during a working memory task (Lee et al., 2005).

### Synchronized networks during emotional processing

Emotion and memory circuits in the brain are highly overlapping and involve the prefrontal cortex, amygdala and other limbic regions (Greenberg et al., 2013). As mentioned, theta synchrony between the hippocampus, prefrontal cortex, and striatum is implicated in working memory and spatial learning. Synchrony has also been observed between the hippocampus and amygdala during fear behaviors (Seidenbecher et al., 2003; Adhikari et al., 2010, 2011; Likhtik et al., 2014). Thus, low-frequency rhythms may also play a role in coordinating brain activity during emotional processing.

In rodent models, the circuits involved in emotion are often studied in the context of learned fear behaviors (Maren, 2001). In these experiments, an innocuous stimulus (the unconditioned stimulus or US) is paired with a conditioned stimulus (the CS), typically a mild foot shock. After pairing, the US takes on fear-eliciting properties which are inferred by quantifying behavioral freezing. Conditioned “fear” has come to mean the defensive freezing behavior observed by investigators even though the experimenter has no true knowledge of the subjective (i.e. fearful) state of the animal. Nonetheless, this paradigm has been successful in uncovering the brain circuits and neural dynamics involved in fear, learning and memory, and sensory processing (Gourley and Taylor, 2016).

As in the case of spatial and working memory, a critical component of the fear circuit is the medial prefrontal cortex (which, as a high level, integrative structure is

involved in virtually all cognitive functions). The mPFC receives input from the amygdala, hippocampus, nucleus accumbens, and other limbic regions that convey the salience, appetitiveness or aversiveness of stimuli (McDonald, 1991; Herry and Johansen, 2014) and is further divided into anatomically and functionally distinct subcompartments. From dorsal to ventral these include: the anterior cingulate cortex (ACC), the prelimbic cortex (PL), and infralimbic cortex (IL) (Heidbreder and Groenewegen, 2003). Of these subregions, the PL is considered essential for fear conditioning because lesions of the PL impair the expression of learned fear behaviors (Vidal-Gonzalez et al., 2006; Corcoran and Quirk, 2007). Following fear conditioning, if the CS is repeatedly presented in the absence of the US, defensive freezing behavior decreases. This new learning process, termed fear extinction conditioning, is impaired by lesions of the IL (Laurent and Westbrook, 2009; Lesting et al., 2013; Giustino and Maren, 2015). Thus, the prefrontal cortex appears functionally segregated when it comes to fear behavior and fear learning.

These lesion studies in conjunction with inactivation, and optogenetic activation experiments confirm that fear behaviors rely on a functional network of structures (including the hippocampus, amygdala, and medial prefrontal cortex) that is conserved across mammalian species (Chan et al., 2011). Therefore, it is important to understand the intra and inter-regional temporal dynamics that mediate fear learning and freezing behavior. Recent studies reveal that low-frequency (~4 Hz) oscillations organize neuronal activation in the mPFC – specifically those amygdalar projections that encode associative fear memories (Courtin et al., 2014; Dejean et al., 2016). Furthermore, this 4 Hz oscillation (which is distinct from hippocampal theta) also couples the mPFC with the basolateral amygdala specifically during periods of behavioral freezing. In fact, the onset

and offset of freezing periods can be well predicted by the emergence of this low frequency oscillation (Karalis et al., 2016).

Given that the close link between the olfactory system and limbic structures and the recent interest in afferent breathing signals from the nose, we investigated the role of respiratory/olfactory rhythms during the expression of fear behavior (Moberly et al., 2018). We were motivated by the tight link between emotion and respiration observed in both rodents and humans and the observation that low frequency rhythms in the range of normal breathing rates emerge in the prefrontal cortex and amygdala during the expression of learned fear. We found that mice regulate their breathing during freezing behavior and that the breathing rhythm is highly correlated with respiratory-related oscillations in the OB and plPFC. Furthermore, both gain of function and loss of function (i.e. removal of olfactory input) experiments demonstrate that olfactory reafferents significantly entrain low frequency, respiration-related activity in the plPFC. Tracing and slice physiology experiments uncovered a functional pathway connecting the anterior olfactory nucleus/taenia tecta and the plPFC that could support frequency-specific coupling observed during conditioned fear behavior.

The removal of olfactory inputs (which eliminate odor-evoked activity as well as reafferent breathing signals) results in behavioral changes – especially related to anxiety and depression. In fact, removal of the olfactory bulbs in both rats and mice was long used to model depression since the behavioral changes caused by bilateral bulbectomy can be reversed by chronic antidepressant treatment (Richardson and Jesberger, 1987; Cryan and Mombereau, 2004; Song and Leonard, 2005). Likewise, disruption of OSNs results in behavioral changes related to emotional processing; anxiety-like behaviors are

observed in Cnga2 null animals, the same animals in which olfactory bulb LFPs are decoupled from breathing but not Trpc2 (VNO-deficient mice) (Glinka et al., 2012; Chen et al., 2014). Likewise, human patients with disrupted nasal airflow have altered behavior. Long-lasting nasal congestion caused by allergic rhinitis or chronic rhinosinusitis (CRS) can impair both odor-evoked and nasal airflow-related signals (Nathan, 2007) and a significant proportion of patients with CRS have comorbidities including depression, cognitive dysfunction, anxiety, and sleep disturbances (Litvack et al., 2011; Tomoum et al., 2015; Schlosser et al., 2016). It is unknown to what extent the loss of respiratory entrainment contributes to these psychiatric symptoms in human patients.

Resting breathing rates in humans are much slower (0.1-0.3 Hz) compared to mice, however, neural oscillations in the human brain are influenced by the respiratory rhythm. Patients with intracranial electrodes for seizure localization have activity in the hippocampus, amygdala, and the medial and lateral orbital frontal cortex correlated with the breathing rhythm and modulated by voluntary breathing. If breathing is through the mouth as opposed to nasal there is a significant reduction in respiratory phase-locked oscillations in the brain (Zelano et al., 2016). Non-neural artifacts such as rhythmic intracranial pressure and breathing-related changes in cerebral perfusion are unlikely to contribute to coherence between iEEG signals and respiration because phase-locking is specific to electrodes that contact grey matter and not white matter or cerebrospinal fluid spaces (Herrero et al., 2018).

The regularity with which these oscillations are observed suggests meaning. But what functional role does entrainment of these non-olfactory regions, especially

hippocampus and amygdala (i.e. memory and emotional processing), serve? Zelano et al. asked if performance in an object recall task is influenced by respiratory phase. Interestingly, recall was improved for pictures that were encoded during inspiration and pictures that were retrieved during inspiration. In an emotional processing task, fearful faces were identified faster if encountered during the inhalation phase of nasal breathing. This suggests that respiration-related activity (despite being at dramatically slower frequency in humans compared to rodents) in the hippocampus and limbic system shapes cognition. And in cases where respiration-related activity is disrupted dysfunction may occur.

In our mouse experiments we find that learned fear behavior is also altered by removing olfactory sensory inputs and thereby disrupting respiration-entrained oscillations in the limbic system. Mice with ablated OSNs as well as mice with inactivated OB networks show increased levels of freezing despite alterations to the 4 Hz LFP signal in the plPFC. These results raise questions regarding the causal relationship between oscillatory activity in prefrontal cortex and fear behavior. Furthermore, they emphasize the need for future experiments to clarify the functional significance of respiration-related rhythms not only in the prefrontal cortex, but other cortical and subcortical regions where they are expressed.

**Figure 1.1. Breathing signals originating from the nose entrain olfactory centers as well as other cortical and subcortical brain regions.** A reafferent breathing signal is detected by mechanosensitive olfactory sensory neurons (OSNs) in the nose and propagated to olfactory areas including the olfactory bulb (OB), anterior olfactory nucleus/taenia tecta (AON/TT), piriform cortex (PC), and amygdala (AM). The breathing signal also reaches non-olfactory regions such as the prelimbic prefrontal cortex (plPFC), barrel cortex (BC), and dentate gyrus (DG) in the hippocampus. Some of these regions in turn communicate with midbrain (such as the periaqueductal gray, PAG) or brainstem centers related to the generation of motor breathing output. Note that many connections are reciprocal, but this is not shown for simplicity.

**Figure 1.1.**

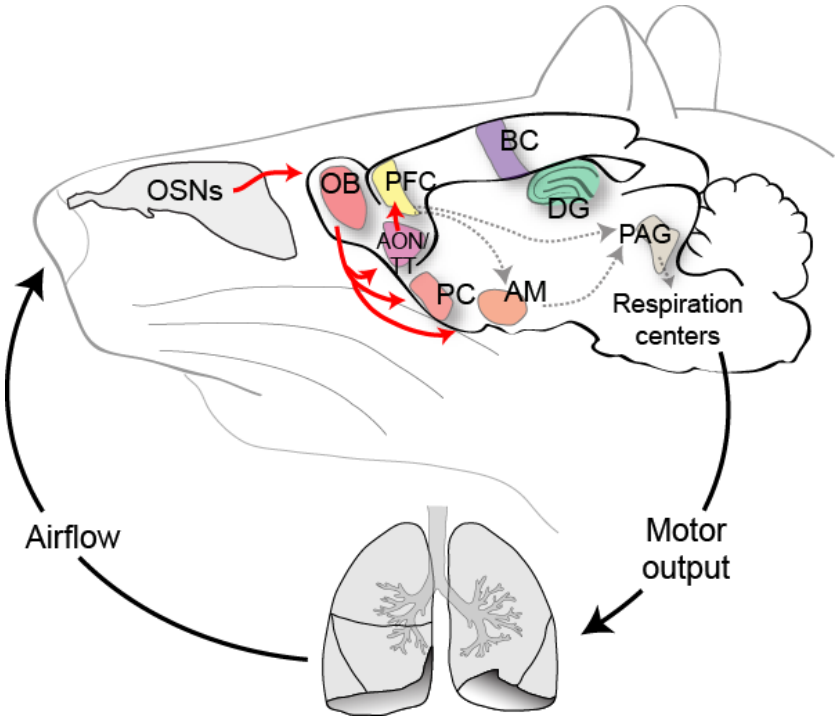
OSNs
OB
PFC
BC
DG
PAG
AON/
TT
PC
AM
Respiration
centers
Airflow
Motor
output

**Table 1.1. Respiration-related neural activity observed across brain regions and species.**

| **Author and date** | Brain region | Recording method | Species |
|---|---|---|---|
| Adrian E.D., 1942 | Olfactory bulb, piriform cortex | EEG | Hedgehog |
| Hobson J.A., 1967 | Frontal regions | Surface EEG | Frog |
| Poe G.R., 1996[1] | Hippocampus | Intrinsic imaging, EEG | Cat |
| Fontanini A., 2003 | Piriform cortex | LFP, in vivo whole cell | Mouse |
| Carlson K.S., 2014 | Olfactory tubercle | LFP | Mouse |
| Ito J., 2014 | Barrel cortex | LFP, single unit | Mouse |
| Yanovsky Y., 2014 | Hippocampus | LFP, single unit | Rat |
| Courtiol E., 2016 | Mediodorsal thalamus | LFP, single unit | Rat |
| Heck D.H., 2016 | Neocortex | ECoG | Human |
| Lockmann A.L.V., 2016 | Hippocampus | LFP, single unit | Mouse |
| Zelano C., 2016 | Piriform cortex, hippocampus | Intracranial EEG | Human |
| Biskamp J. 2017 | Prefrontal cortex | LFP, single unit | Mouse |
| Herrero J.L., 2018 | Amygdala, hippocampus, Insula | Intracranial EEG | Human |
| Karalis N., 2018 | Nucleus accumbens, basolateral amygdala, thalamus | LFP, single unit | Mouse |
| Koszeghy A., 2018 | Orbitofrontal cortex | LFP, single unit | Mouse |

## References


Adhikari A, Topiwala MA, Gordon JA (2010) Synchronized activity between the ventral hippocampus and the medial prefrontal cortex during anxiety. Neuron 65:257-269.

Adhikari A, Topiwala MA, Gordon JA (2011) Single units in the medial prefrontal cortex with anxiety-related firing patterns are preferentially influenced by ventral hippocampal activity. Neuron 71:898-910.

Adrian ED (1942) Olfactory reactions in the brain of the hedgehog. J Physiol 100:459-473.

Anderson KL, Rajagovindan R, Ghacibeh GA, Meador KJ, Ding M (2010) Theta oscillations mediate interaction between prefrontal cortex and medial temporal lobe in human memory. Cereb Cortex 20:1604-1612.

Benchenane K, Tiesinga PH, Battaglia FP (2011) Oscillations in the prefrontal cortex: a gateway to memory and attention. Curr Opin Neurobiol 21:475-485.

Benchenane K, Peyrache A, Khamassi M, Tierney PL, Gioanni Y, Battaglia FP, Wiener SI (2010) Coherent theta oscillations and reorganization of spike timing in the hippocampal- prefrontal network upon learning. Neuron 66:921-936.

Biskamp J, Bartos M, Sauer JF (2017) Organization of prefrontal network activity by respiration-related oscillations. Sci Rep 7:45508.

Bloch S, Lemeignan M, Aguilerat N (1991) Specific Respiratory Patterns Distinguish among Human Basic Emotions. Int J Psychophysiol 11:141-154.

Boiten FA (1998) The effects of emotional behaviour on components of the respiratory cycle. Biol Psychol 49:29-51.

Boiten FA, Frijda NH, Wientjes CJE (1994) Emotions and Respiratory Patterns - Review and Critical Analysis. Int J Psychophysiol 17:103-128.

Brown RP, Gerbarg PL (2009) Yoga breathing, meditation, and longevity. Ann N Y Acad Sci 1172:54-62.

Brunet LJ, Gold GH, Ngai J (1996) General anosmia caused by a targeted disruption of the mouse olfactory cyclic nucleotide-gated cation channel. Neuron 17:681-693.

Buonviso N, Amat C, Litaudon P (2006) Respiratory modulation of olfactory neurons in the rodent brain. Chem Senses 31:145-154.

Buzsaki G (2002) Theta oscillations in the hippocampus. Neuron 33:325-340.

Buzsaki G, Wang XJ (2012) Mechanisms of gamma oscillations. Annu Rev Neurosci 35:203-225.

Buzsaki G, Anastassiou CA, Koch C (2012) The origin of extracellular fields and currents--EEG, ECoG, LFP and spikes. Nat Rev Neurosci 13:407-420.

Buzsaki G, Logothetis N, Singer W (2013) Scaling Brain Size, Keeping Timing: Evolutionary Preservation of Brain Rhythms. Neuron 80:751-764.

Canolty RT, Knight RT (2010) The functional role of cross-frequency coupling. Trends Cogn Sci 14:506-515.

Carlson KS, Dillione MR, Wesson DW (2014) Odor- and state-dependent olfactory tubercle local field potential dynamics in awake rats. J Neurophysiol 111:2109-2123.

Chan T, Kyere K, Davis BR, Shemyakin A, Kabitzke PA, Shair HN, Barr GA, Wiedenmayer CP (2011) The role of the medial prefrontal cortex in innate fear regulation in infants, juveniles, and adolescents. The Journal of neuroscience : the official journal of the Society for Neuroscience 31:4991-4999.

Chen YM, Liu XF, Jia XL, Zong W, Ma YY, Xu FQ, Wang JH (2014) Anxiety- and depressive-like behaviors in olfactory deficient Cnga2 knockout mice. Behav Brain Res 275:219-224.

Cole SR, Voytek B (2017) Brain Oscillations and the Importance of Waveform Shape. Trends Cogn Sci 21:137-149.

Connelly T, Yu YQ, Grosmaitre X, Wang J, Santarelli LC, Savigner A, Qiao X, Wang ZS, Storm DR, Ma MH (2015) G protein-coupled odorant receptors underlie mechanosensitivity in mammalian olfactory sensory neurons. P Natl Acad Sci USA 112:590-595.

Corcoran KA, Quirk GJ (2007) Activity in prelimbic cortex is necessary for the expression of learned, but not innate, fears. The Journal of neuroscience : the official journal of the Society for Neuroscience 27:840-844.

Courtin J, Chaudun F, Rozeske RR, Karalis N, Gonzalez-Campo C, Wurtz H, Abdi A, Baufreton J, Bienvenu TC, Herry C (2014) Prefrontal parvalbumin interneurons shape neuronal activity to drive fear expression. Nature 505:92-96.

Courtiol E, Wilson DA (2016) Neural Representation of Odor-Guided Behavior in the Rat Olfactory Thalamus. The Journal of neuroscience : the official journal of the Society for Neuroscience 36:5946-5960.

Cryan JF, Mombereau C (2004) In search of a depressed mouse: utility of models for studying depression-related behavior in genetically modified mice. Mol Psychiatr 9:326-357.

DeCoteau WE, Thorn C, Gibson DJ, Courtemanche R, Mitra P, Kubota Y, Graybiel AM (2007) Learning-related coordination of striatal and hippocampal theta rhythms during acquisition of a procedural maze task. P Natl Acad Sci USA 104:5644-5649.

Dejean C, Courtin J, Karalis N, Chaudun F, Wurtz H, Bienvenu TC, Herry C (2016) Prefrontal neuronal assemblies temporally control fear behaviour. Nature 535:420-424.

Del Negro CA, Funk GD, Feldman JL (2018) Breathing matters. Nat Rev Neurosci 19:351-367.

Deschenes M, Moore J, Kleinfeld D (2012) Sniffing and whisking in rodents. Curr Opin Neurobiol 22:243-250.

Eckhorn R, Reitboeck HJ, Arndt M, Dicke P (1990) Feature Linking via Synchronization among Distributed Assemblies: Simulations of Results from Cat Visual Cortex. Neural Comput 2:293-307.

Engel AK, Fries P, Konig P, Brecht M, Singer W (1999) Temporal binding, binocular rivalry, and consciousness. Conscious Cogn 8:128-151.

Feldman JL, Mitchell GS, Nattie EE (2003) Breathing: Rhythmicity, plasticity, chemosensitivity. Annu Rev Neurosci 26:239-266.

Feldman JL, Del Negro CA, Gray PA (2013) Understanding the Rhythm of Breathing: So Near, Yet So Far. Annu Rev Physiol 75:423-452.

Fontanini A, Bower JM (2005) Variable coupling between olfactory system activity and respiration in ketamine/xylazine anesthetized rats. J Neurophysiol 93:3573-3581.

Fontanini A, Spano P, Bower JM (2003) Ketamine-xylazine-induced slow (< 1.5 Hz) oscillations in the rat piriform (olfactory) cortex are functionally correlated with respiration. The Journal of neuroscience : the official journal of the Society for Neuroscience 23:7993-8001.

Freeman WJ (1972) Measurement of oscillatory responses to electrical stimulation in olfactory bulb of cat. J Neurophysiol 35:762-779.

Fries P (2005) A mechanism for cognitive dynamics: neuronal communication through neuronal coherence. Trends Cogn Sci 9:474-480.

Fujisawa S, Buzsaki G (2011) A 4 Hz Oscillation Adaptively Synchronizes Prefrontal, VTA, and Hippocampal Activities. Neuron 72:153-165.

Giustino TF, Maren S (2015) The Role of the Medial Prefrontal Cortex in the Conditioning and Extinction of Fear. Front Behav Neurosci 9.

Glinka ME, Samuels BA, Diodato A, Teillon J, Mei DF, Shykind BM, Hen R, Fleischmann A (2012) Olfactory Deficits Cause Anxiety-Like Behaviors in Mice. J Neurosci 32:6718-6725.

Gourley SL, Taylor JR (2016) Going and stopping: Dichotomies in behavioral control by the prefrontal cortex. Nat Neurosci 19:656-664.

Greenberg T, Carlson JM, Cha J, Hajcak G, Mujica-Parodi LR (2013) Ventromedial prefrontal cortex reactivity is altered in generalized anxiety disorder during fear generalization. Depress Anxiety 30:242-250.

Grosmaitre X, Santarelli LC, Tan J, Luo MM, Ma MH (2007) Dual functions of mammalian olfactory sensory neurons as odor detectors and mechanical sensors. Nat Neurosci 10:348-354.

Haberly LB, Price JL (1977) The axonal projection patterns of the mitral and tufted cells of the olfactory bulb in the rat. Brain Res 129:152-157.

Harper RM, Frysinger RC, Trelease RB, Marks JD (1984) State-dependent alteration of respiratory cycle timing by stimulation of the central nucleus of the amygdala. Brain Res 306:1-8.

Hasselmo ME (2005) What is the function of hippocampal theta Rhythm? Linking behavioral data to phasic properties of field potential and unit recording data. Hippocampus 15:936-949.

Hasselmo ME, Hay J, Ilyn M, Gorchetchnikov A (2002) Neuromodulation, theta rhythm and rat spatial navigation. Neural Netw 15:689-707.

Heck DH, McAfee SS, Liu Y, Babajani-Feremi A, Rezaie R, Freeman WJ, Wheless JW, Papanicolaou AC, Ruszinko M, Kozma R (2017) Breathing as a Fundamental Rhythm of Brain Function. Front Neural Circuit 10.

Heidbreder CA, Groenewegen HJ (2003) The medial prefrontal cortex in the rat: evidence for a dorso-ventral distinction based upon functional and anatomical characteristics. Neurosci Biobehav Rev 27:555-579.

Herrero JL, Khuvis S, Yeagle E, Cerf M, Mehta AD (2018) Breathing above the brain stem: volitional control and attentional modulation in humans. J Neurophysiol 119:145-159.

Herry C, Johansen JP (2014) Encoding of fear learning and memory in distributed neuronal circuits. Nat Neurosci 17:1644-1654.

Hobson JA (1967) Respiration and Eeg Synchronization in Frog. Nature 213:988-&.

Homma I, Masaoka Y (2008) Breathing rhythms and emotions. Exp Physiol 93:1011-1021.

Hyafil A, Giraud AL, Fontolan L, Gutkin B (2015) Neural Cross-Frequency Coupling: Connecting Architectures, Mechanisms, and Functions. Trends Neurosci 38:725-740.

Ito J, Roy S, Liu Y, Cao Y, Fletcher M, Lu L, Boughter JD, Grun S, Heck DH (2014) Whisker barrel cortex delta oscillations and gamma power in the awake mouse are linked to respiration. Nat Commun 5.

Iwata R, Kiyonari H, Imai T (2017) Mechanosensory-Based Phase Coding of Odor Identity in the Olfactory Bulb. Neuron 96:1139-1152 e1137.

Jensen O, Colgin LL (2007) Cross-frequency coupling between neuronal oscillations. Trends Cogn Sci 11:267-269.

Jerath R, Crawford MW, Barnes VA, Harden K (2015) Self-Regulation of Breathing as a Primary Treatment for Anxiety. Appl Psychophys Biof 40:107-115.

Jones MW, Wilson MA (2005) Theta rhythms coordinate hippocampal-prefrontal interactions in a spatial memory task. PLoS Biol 3:e402.

Kajikawa Y, Schroeder CE (2011) How Local Is the Local Field Potential? Neuron 72:847-858.

Kam K, Worrell JW, Janczewski WA, Cui Y, Feldman JL (2013) Distinct Inspiratory Rhythm and Pattern Generating Mechanisms in the preBotzinger Complex. J Neurosci 33:9235-9245.

Karalis N, Dejean C, Chaudun F, Khoder S, Rozeske RR, Wurtz H, Bagur S, Benchenane K, Sirota A, Courtin J, Herry C (2016) 4-Hz oscillations synchronize prefrontal-amygdala circuits during fear behavior. Nat Neurosci 19:605-612.

Kay LM (2005) Theta oscillations and sensorimotor performance. P Natl Acad Sci USA 102:3863-3868.

Kay LM, Beshel J, Brea J, Martin C, Rojas-Libano D, Kopell N (2009) Olfactory oscillations: the what, how and what for. Trends Neurosci 32:207-214.

Kleinfeld D, Moore JD, Wang F, Deschenes M (2014a) The Brainstem Oscillator for Whisking and the Case for Breathing as the Master Clock for Orofacial Motor Actions. Cold Spring Harb Symp Quant Biol 79:29-39.

Kleinfeld D, Deschenes M, Wang F, Moore JD (2014b) More than a rhythm of life: breathing as a binder of orofacial sensation. Nat Neurosci 17:647-651.

Koszeghy A, Lasztoczi B, Forro T, Klausberger T (2018) Spike-Timing of Orbitofrontal Neurons Is Synchronized With Breathing. Front Cell Neurosci 12:105.

Laurent V, Westbrook RF (2009) Inactivation of the infralimbic but not the prelimbic cortex impairs consolidation and retrieval of fear extinction. Learn Mem 16:520-529.

Lee H, Simpson GV, Logothetis NK, Rainer G (2005) Phase locking of single neuron activity to theta oscillations during working memory in monkey extrastriate visual cortex. Neuron 45:147-156.

Lesting J, Daldrup T, Narayanan V, Himpe C, Seidenbecher T, Pape HC (2013) Directional theta coherence in prefrontal cortical to amygdalo-hippocampal pathways signals fear extinction. PLoS One 8:e77707.

Likhtik E, Stujenske JM, Topiwala MA, Harris AZ, Gordon JA (2014) Prefrontal entrainment of amygdala activity signals safety in learned fear and innate anxiety. Nat Neurosci 17:106-113.

Litvack JR, Mace J, Smith TL (2011) Role of Depression in Outcomes of Endoscopic Sinus Surgery. Otolaryng Head Neck 144:446-451.

Liu Y, McAfee SS, Heck DH (2017) Hippocampal sharp-wave ripples in awake mice are entrained by respiration. Sci Rep 7:8950.

Lockmann ALV, Laplagne DA, Leao RN, Tort ABL (2016) A Respiration-Coupled Rhythm in the Rat Hippocampus Independent of Theta and Slow Oscillations. J Neurosci 36:5338-5352.

Loughlin SE, Foote SL, Bloom FE (1986) Efferent projections of nucleus locus coeruleus: topographic organization of cells of origin demonstrated by three-dimensional reconstruction. Neuroscience 18:291-306.

Ma X, Yue ZQ, Gong ZQ, Zhang H, Duan NY, Shi YT, Wei GX, Li YF (2017) The Effect of Diaphragmatic Breathing on Attention, Negative Affect and Stress in Healthy Adults. Front Psychol 8.

Macrides F, Eichenbaum HB, Forbes WB (1982) Temporal relationship between sniffing and the limbic theta rhythm during odor discrimination reversal learning. The Journal of neuroscience : the official journal of the Society for Neuroscience 2:1705-1717.

Maren S (2001) Neurobiology of Pavlovian fear conditioning. Annu Rev Neurosci 24:897-931.

Martin C, Beshel J, Kay LM (2007) An olfacto-hippocampal network is dynamically involved in odor-discrimination learning. J Neurophysiol 98:2196-2205.

Masaoka Y, Homma I (2004) Amygdala and emotional breathing in humans. Adv Exp Med Biol 551:9-14.

McDonald AJ (1991) Organization of amygdaloid projections to the prefrontal cortex and associated striatum in the rat. Neuroscience 44:1-14.

Melnychuk MC, Dockree PM, O'Connell RG, Murphy PR, Balsters JH, Robertson IH (2018) Coupling of respiration and attention via the locus coeruleus: Effects of meditation and pranayama. Psychophysiology:e13091.

Meuret AE, Ritz T, Wilhelm FH, Roth WT (2005) Voluntary hyperventilation in the treatment of panic disorder--functions of hyperventilation, their implications for breathing training, and recommendations for standardization. Clin Psychol Rev 25:285-306.

Moberly AH, Schreck M, Bhattarai JP, Zweifel LS, Luo W, Ma M (2018) Olfactory inputs modulate respiration-related rhythmic activity in the prefrontal cortex and freezing behavior. Nat Commun 9:1528.

Moore JD, Deschenes M, Furuta T, Huber D, Smear MC, Demers M, Kleinfeld D (2013) Hierarchy of orofacial rhythms revealed through whisking and breathing. Nature 497:205-+.

Moriya-Ito K, Tanaka I, Umitsu Y, Ichikawa M, Tokuno H (2015) The olfactory bulb and the number of its glomeruli in the common marmoset (Callithrix jacchus). Neurosci Res 93:158-163.

Nardi AE, Lopes FL, Valenca AM, Nascimento I, Mezzasalma MA, Zin WA (2004) Psychopathological description of hyperventilation-induced panic attacks: a comparison with spontaneous panic attacks. Psychopathology 37:29-35.

Nathan RA (2007) The burden of allergic rhinitis. Allergy Asthma Proc 28:3-9.

Nguyen Chi V, Muller C, Wolfenstetter T, Yanovsky Y, Draguhn A, Tort AB, Brankack J (2016) Hippocampal Respiration-Driven Rhythm Distinct from Theta Oscillations in Awake Mice. The Journal of neuroscience : the official journal of the Society for Neuroscience 36:162-177.

Nobis WP, Schuele S, Templer JW, Zhou GY, Lane G, Rosenow JM, Zelano C (2018) Amygdala-stimulation-induced apnea is attention and nasal-breathing dependent. Ann Neurol 83:460-471.

Onoda N, Mori K (1980) Depth distribution of temporal firing patterns in olfactory bulb related to air-intake cycles. J Neurophysiol 44:29-39.

Philippot P, Chapelle G, Blairy S (2002) Respiratory feedback in the generation of emotion. Cognition Emotion 16:605-627.

Phillips ME, Sachdev RN, Willhite DC, Shepherd GM (2012) Respiration drives network activity and modulates synaptic and circuit processing of lateral inhibition in the olfactory bulb. The Journal of neuroscience : the official journal of the Society for Neuroscience 32:85-98.

Rau H, Pauli P, Brody S, Elbert T, Birbaumer N (1993) Baroreceptor stimulation alters cortical activity. Psychophysiology 30:322-325.

Richardson JS, Jesberger JA (1987) Validity of the Olfactory Bulbectomized Rat as a Model of Primary Depression. Int J Neurosci 32:593-593.

Rojas-Libano D, Frederick DE, Egana JI, Kay LM (2014) The olfactory bulb theta rhythm follows all frequencies of diaphragmatic respiration in the freely behaving rat. Front Behav Neurosci 8:214.

Salinas E, Sejnowski TJ (2001) Correlated neuronal activity and the flow of neural information. Nat Rev Neurosci 2:539-550.

Sauseng P, Klimesch W (2008) What does phase information of oscillatory brain activity tell us about cognitive processes? Neurosci Biobehav Rev 32:1001-1013.

Schlosser RJ, Hyer JM, Smith TL, Mace JC, Cortese BM, Uhde TW, Rudmik L, Soler ZM (2016) Depression-Specific Outcomes After Treatment of Chronic Rhinosinusitis. Jama Otolaryngol 142:370-376.

Schwindel CD, McNaughton BL (2011) Hippocampal-cortical interactions and the dynamics of memory trace reactivation. Prog Brain Res 193:163-177.

Seidenbecher T, Laxmi TR, Stork O, Pape HC (2003) Amygdalar and hippocampal theta rhythm synchronization during fear memory retrieval. Science 301:846-850.

Severson KS, Xu D, Van de Loo M, Bai L, Ginty DD, O'Connor DH (2017) Active Touch and Self-Motion Encoding by Merkel Cell-Associated Afferents. Neuron 94:666-676 e669.

Smear M, Shusterman R, O'Connor R, Bozza T, Rinberg D (2011) Perception of sniff phase in mouse olfaction. Nature 479:397-U149.

Song C, Leonard BE (2005) The olfactory bulbectomised rat as a model of depression. Neurosci Biobehav Rev 29:627-647.

Tamura M, Spellman TJ, Rosen AM, Gogos JA, Gordon JA (2017) Hippocampal-prefrontal theta-gamma coupling during performance of a spatial working memory task. Nat Commun 8:2182.

Tomoum MO, Klattcromwell C, DelSignore A, Ebert C, Senior BA (2015) Depression and anxiety in chronic rhinosinusitis. Int Forum Allergy Rh 5:674-681.

Tort AB, Kramer MA, Thorn C, Gibson DJ, Kubota Y, Graybiel AM, Kopell NJ (2008) Dynamic cross-frequency couplings of local field potential oscillations in rat striatum and hippocampus during performance of a T-maze task. P Natl Acad Sci USA 105:20517-20522.

Tort ABL, Brankack J, Draguhn A (2018) Respiration-Entrained Brain Rhythms Are Global but Often Overlooked. Trends Neurosci 41:186-197.

Ueki S, Domino EF (1961) Some Evidence for a Mechanical Receptor in Olfactory Function. J Neurophysiol 24:12-&.

van de Ven GM, Trouche S, McNamara CG, Allen K, Dupret D (2016) Hippocampal Offline Reactivation Consolidates Recently Formed Cell Assembly Patterns during Sharp Wave-Ripples. Neuron 92:968-974.

Vanderwolf CH (1969) Hippocampal electrical activity and voluntary movement in the rat. Electroencephalogr Clin Neurophysiol 26:407-418.

Varela F, Lachaux JP, Rodriguez E, Martinerie J (2001) The brainweb: Phase synchronization and large-scale integration. Nature Reviews Neuroscience 2:229-239.

Vertes RP, Hoover WB, Viana Di Prisco G (2004) Theta rhythm of the hippocampus: subcortical control and functional significance. Behav Cogn Neurosci Rev 3:173-200.

Vidal-Gonzalez I, Vidal-Gonzalez B, Rauch SL, Quirk GJ (2006) Microstimulation reveals opposing influences of prelimbic and infralimbic cortex on the expression of conditioned fear. Learn Mem 13:728-733.

Vinck M, Battaglia FP, Womelsdorf T, Pennartz C (2012) Improved measures of phase-coupling between spikes and the Local Field Potential. J Comput Neurosci 33:53-75.

Voytek B, Knight RT (2015) Dynamic network communication as a unifying neural basis for cognition, development, aging, and disease. Biol Psychiatry 77:1089-1097.

Wachowiak M, Shipley MT (2006) Coding and synaptic processing of sensory information in the glomerular layer of the olfactory bulb. Semin Cell Dev Biol 17:411-423.

Watson BO, Buzsaki G (2015) Sleep, Memory & Brain Rhythms. Daedalus-Us 144:67-82.

Welzl H, Bures J (1977) Lick-Synchronized Breathing in Rats. Physiol Behav 18:751-753.

Wu RQ, Liu Y, Wang L, Li B, Xu FQ (2017) Activity Patterns Elicited by Airflow in the Olfactory Bulb and Their Possible Functions. J Neurosci 37:10700-10711.

Yackle K, Schwarz LA, Kam K, Sorokin JM, Huguenard JR, Feldman JL, Luo L, Krasnow MA (2017) Breathing control center neurons that promote arousal in mice. Science 355:1411-1415.

Yanovsky Y, Ciatipis M, Draguhn A, Tort AB, Brankack J (2014) Slow oscillations in the mouse hippocampus entrained by nasal respiration. The Journal of neuroscience : the official journal of the Society for Neuroscience 34:5949-5964.

Zald DH, Pardo JV (1997) Emotion, olfaction, and the human amygdala: amygdala activation during aversive olfactory stimulation. P Natl Acad Sci USA 94:4119-4124.

Zelano C, Jiang HD, Zhou GY, Arora N, Schuele S, Rosenow J, Gottfried JA (2016) Nasal Respiration Entrains Human Limbic Oscillations and Modulates Cognitive Function. J Neurosci 36:12448-12467.

Zhong W, Ciatipis M, Wolfenstetter T, Jessberger J, Muller C, Ponsel S, Yanovsky Y, Brankack J, Tort ABL, Draguhn A (2017) Selective entrainment of gamma subbands by different slow network oscillations. P Natl Acad Sci USA 114:4519-4524.

# CHAPTER 2: MANIPULATING OLFACTORY SENSORY NEURON ACTIVITY *IN VITRO* AND *IN VIVO*

## Optogenetics provides spatial-temporal control over neural populations

Our understanding of brain function has been greatly advanced by the development of methods for manipulating the activity of specific neuronal populations. For example, Wilder Penfield used extracellular electrical microstimulation to link cortical regions with specific cognitive and motor outputs (Penfield, 1961). Among other things, this technique verified the presence of sensory-motor maps in the brain (Catani, 2017). However, the success of these experiments depended on the activation of large anatomical clusters of neurons that share functional properties (cortical homunculi in this example). Since electrical stimulation activates all neuronal processes in the stimulation field, there is a risk of activating non-specific fibers of passage or causing multi-synaptic effects. This makes inferring the causal effect of neuronal activation on downstream brain regions or behavior difficult. To circumvent this problem, genetic techniques have been developed to activate neurons with high temporal and cellular precision. Optogenetics is the field standard for activating or inhibiting circuits using high-speed, light-sensitive neuromodulatory opsins that are selectively expressed in genetically identified neurons (Deisseroth, 2011). For example, in neurons expressing the light-gated cation channel channelrhodopsin-2 (ChR2) neuronal spiking is controlled with millisecond precision with blue light (473 nm) stimulation (Boyden et al., 2005; Fenno et al., 2011).

We took advantage of this approach to investigate the effect of olfactory sensory neuron (OSN) activation on downstream olfactory and non-olfactory networks. Since the

breathing rhythm, and especially airflow through the nasal passage, is correlated with local field potential (LFP) activity in numerous brain regions, we hypothesized that activation of OSNs in an odor-independent manner entrains the olfactory bulb and other regions receiving an afferent copy of the breathing signal. We reasoned that artificial activation of OSNs at frequencies non-congruous with breathing would entrain LFPs recorded from regions known to express respiratory-related rhythms including the olfactory bulb (OB), hippocampus (HP), and barrel cortex (BC).

To test this we generated *OMP-ChR2* heterozygous mice by crossing OMP-Cre mice (which express Cre recombinase under the promoter of the olfactory marker protein gene in mature OSNs (Li et al., 2004) with a Rosa-CAG-LSL-ChR2(H134R)-EYFP-WPRE line where a loxp-flanked STOP cassette normally prevents transcription of the downstream ChR2-EYFP fusion gene (Madisen et al., 2012). Our ultimate goal was to activate OSNs in the nasal epithelium of freely behaving animals while simultaneously recording extracellular field potentials from the brain. However, even though optogenetic activation of OSNs in the nose has been used in the context of odor-coding behaviors the physiological effects of intranasal stimulation are uncharacterized. For example, mice discriminate between optogenetic OSN activation that occurs at different phases of the breathing cycle (Smear et al., 2011; Smear et al., 2013; Wilson et al., 2017). But it is not known to what extent light stimulation delivered to the nose can activate widespread OSNs.

## Results

We took two steps to characterize the effects of *in vivo* OSN stimulation. First, we dissected out the nasal epithelium (septal) from OMP-ChR2 mice and placed it on a high-density microelectrode array typically used to record from retinal ganglion cells (Multi Channel Systems GmbH, Reutlingen Germany). In this ex-vivo epithelial preparation, spontaneous, extracellular events were recorded from a subset of electrode contacts (18 out of 60 channels, **Figure 2.1**). Wide-field illumination of the MEA with blue LED light produced activity on a total of 24 electrode contacts suggesting that spontaneously active OSNs expressing ChR2 can be activated by light. Next, we stimulated OSNs in anesthetized OMP-ChR2 mice to look at light-evoked OSN activity in the olfactory bulb (**Figure 2.2**). In extracellular recordings from the OB of anesthetized rodents the spontaneous activity of mitral and tufted units is temporally modulated by the breathing rhythm (Chaput, 1986; Ravel and Pager, 1990; Cury and Uchida, 2010; Shusterman et al., 2011). We find presumptive mitral/tufted cells based on phase-locked firing to respiration and dorsal-ventral recording depth (Davison and Katz, 2007). These units are normally active during a specific phase of the respiratory cycle but become entrained to light stimuli delivered to the nasal epithelium.

Finally, we implanted chronic extracellular LFP electrodes in the OB, HP, and BC and recorded oscillatory activity from these regions during OSN stimulations in freely behaving and anesthetized mice (**Figure 2.3**). OSN photostimulation at 10 Hz induced a 10 Hz rhythm in the OB. This is perhaps unsurprising given the massive level of convergence of OSN axons onto glomeruli and the artificial nature of simultaneously activating them. OSN stimulation also evoked responses in the HP and the BC. Using

spectral decomposition, we analyzed the power in the wideband LPF signals acquired during 10 Hz OSN stimulation and found increased power at the stimulation frequency in mice expressing OMP-ChR2, but not in ChR2 negative mice.

Respiratory-related activity is observed in the HP of both awake and anesthetized mice (Yanovsky et al., 2014; Lockmann et al., 2016; Nguyen Chi et al., 2016). Loss of function experiments demonstrate that respiration-patterned oscillations in the HP depend on airflow into the nasal cavity. Entrainment is likely via due to connectivity between the OB and entorhinal cortex. Here, we use a gain of function activation experiments to show that OSN activity (although artificial) can influence the endogenous activity in the OB which likely drives synchronous output to downstream olfactory cortex. Further cortico-cortical connections could support the further expansion of the signal throughout the brain.

Unlike the HP the mouse barrel cortex does not receive inputs from olfactory cortex (DeNardo et al., 2015). So how do peripherally generated, respiration-entrained signals reach somatosensory regions? Retrograde labeling experiments suggest a potential pathway may be basal forebrain neurons that project widely throughout the cortex (Sarter et al., 1999; Ito et al., 2014). The basal forebrain is a collection of structures including the medial septum, ventral pallidum, diagonal band nuclei, and substantia innominate each of which contains multiple cell types that differ in transmitter content and electrophysiological properties. Of these, large choline acetyl transferase containing (ChAT) neurons (about 20% of the basal forebrain) have been intensively studied due to their role in cortical modulation (Houser et al., 1985; Li et al., 2018). Intriguingly, Manns et al. found units in the basal forebrain including GABAergic,

glutamatergic, and cholinergic projection neurons that 'discharge rhythmically in correlation with rhythmic slow activity recorded in the prefrontal, enthorinal, piriform cortex, and olfactory bulb'. This activity presumably corresponds to the respiratory rhythm although respiration was not explicitly monitored. Some units in the horizontal band nuclei (some of which are presumably $ChAT^{+}$) are modulated by olfactory input (electrical stimulation of the lateral olfactory tract) and the activity of some single units in the medial septum/diagonal band is phase-locked to the sniffing cycle (Linster and Hasselmo, 2000; Tsanov et al., 2014).

Thus, one possibility is that respiratory-related olfactory signals reach basal forebrain cells that can influence cortical activity in the somatosensory, prefrontal, orbitofrontal cortices. We traced the output of the OB via injections of AAV-Cre into the olfactory bulbs of ROSA26iap mice. There are cases where ChAT-expressing cells in the olfactory tubercle (a forebrain structure just lateral to the diagonal band and ventrolateral to the substantia innominata) overlap with olfactory bulb outputs (**Figure 2.4**). Whether this represents a functional connection and the extent to which respiratory-related olfactory inputs can modulate cholinergic neurons remains to be investigated.

**Figure 2.1. The use of MEA for the analysis of the electrophysiological properties of OSNs expressing ChR2. A.** Schematic of the MEA culture dish used to record from an *ex-vivo* olfactory epithelium preparation. Electrodes are spaced 200 um apart and have a diameter of 30 um. **B.** Representative example of a simultaneous recording of the electrical activity from three channels showing spontaneous (left) and light evoked (right) responses. Threshold-detected waveforms from Channel 57 in both spontaneous and light-evoked conditions are overlaid above the raw traces. **C.** Raster plot depicting the signal from all 60 electrodes over 30 seconds during simultaneous (left) and light evoked (right) activity. Each line corresponds to an electrode and each dot represents a threshold crossing event. The far right shows light-evoked activity on an expanded time base. Light-evoked activity could be picked up on 24/60 electrodes.

**Figure 2.1.**

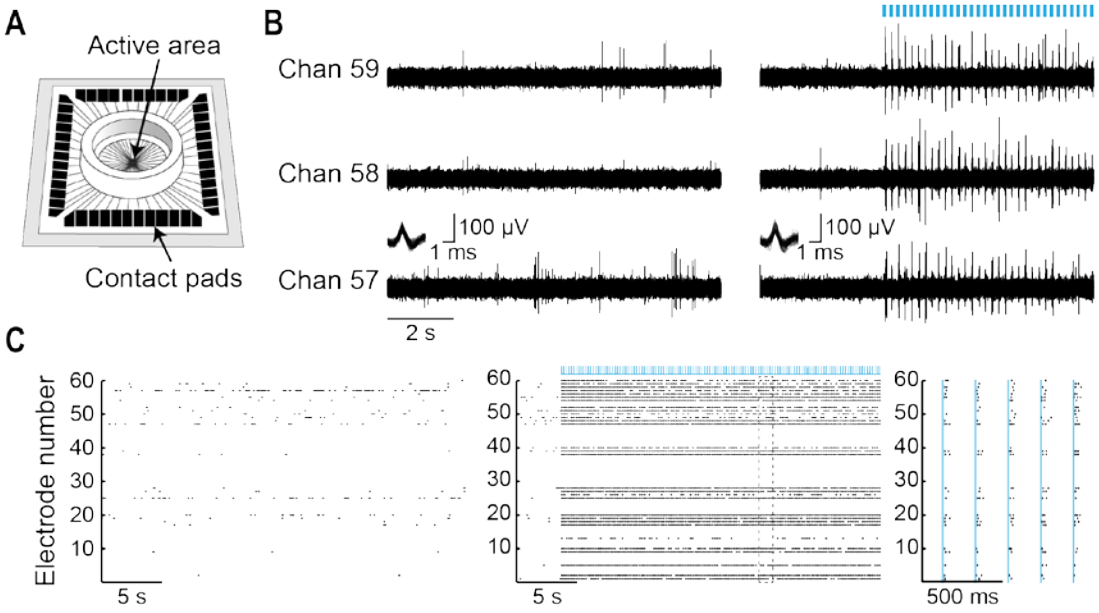
A
Active area
Contact pads
B
Chan 59
Chan 58
Chan 57
100 µV
1 ms
100 µV
1 ms
2 s
C
Electrode number
60
50
40
30
20
10
5 s
5 s
500 ms

**Figure 2.2. Stimulating OSNs influences OB activity *in vivo*. A.** Top, schematic of the recording setup. OSNs are stimulated via an optic fiber in the nasal cavity of an anesthetized OMP-ChR2 mouse while extracellular activity is recorded from the OB. Bottom, coronal section through the olfactory bulbs. Fos staining suggests that this intra-nasal stimulation approach mostly activates OSNs in the medial aspect of the sensory epithelium that project to medial OB glomeruli. D, dorsal, M, medial **B.** Representative examples of extracellular activity from putative mitral/tufted cells in the olfactory bulb during OSN stimulation. Respiration is simultaneously monitored with a chest strap. Normally the units are active during a specific phase of the respiratory cycle. During OSN activation (2 Hz top, 5 Hz bottom, indicated in blue) the units become entrained to light stimulation.

**Figure 2.2.**

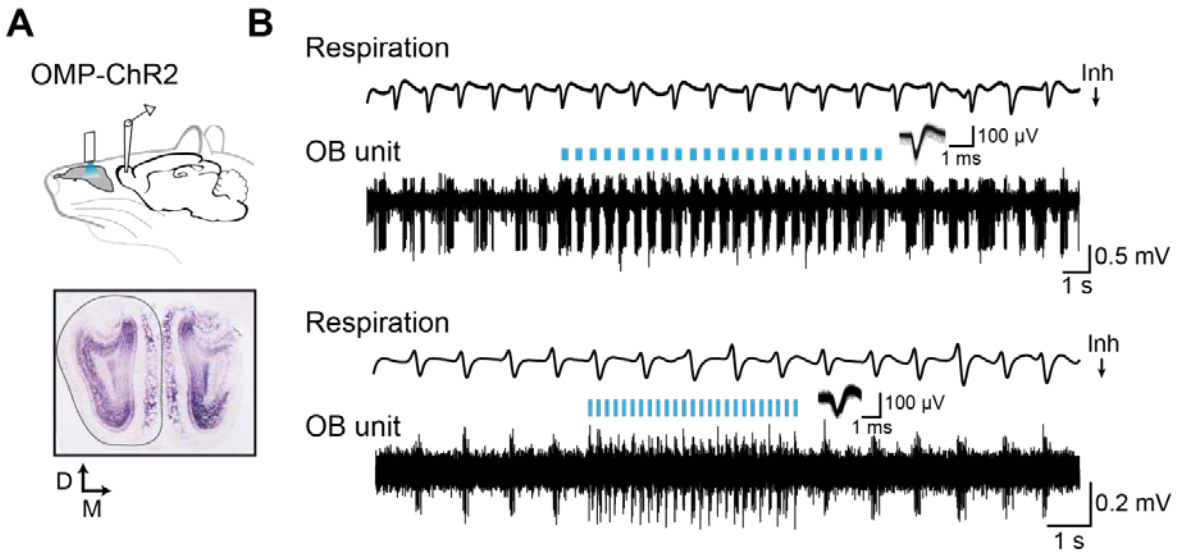
A
OMP-ChR2
D
M
B
Respiration
Inh
OB unit
100 µV
1 ms
0.5 mV
1 s
Respiration
Inh
OB unit
100 µV
1 ms
0.2 mV
1 s

**Figure 2.3. Stimulating OSNs influences LFP activity in multiple brain regions in vivo. A.** Representative simultaneous extracellular LFP recordings taken from an OMP-ChR2 mouse. Recordings are from the olfactory bulb (OB), hippocampus (HP) and barrel cortex (BC) during OSN stimulation (10 Hz) delivered via an intranasal fiber optic cannula. Insets show the averaged responses to a single 5 ms light pulses. All regions show light-evoked responses during both normal behavior (top) and under ketamine-xylazine anesthesia (bottom) ruling out motor artifacts that may be associated with light stimulation. **B**. Frequency spectra of LFP signals from the OB, HP, and BC during OSN stimulation. Spectral power at the OSN stimulation frequency (10 Hz, indicated by the vertical blue line) is increased in mice expressing ChR2 (top) but not in control mice that do not express ChR2 (bottom).

**Figure 2.3**

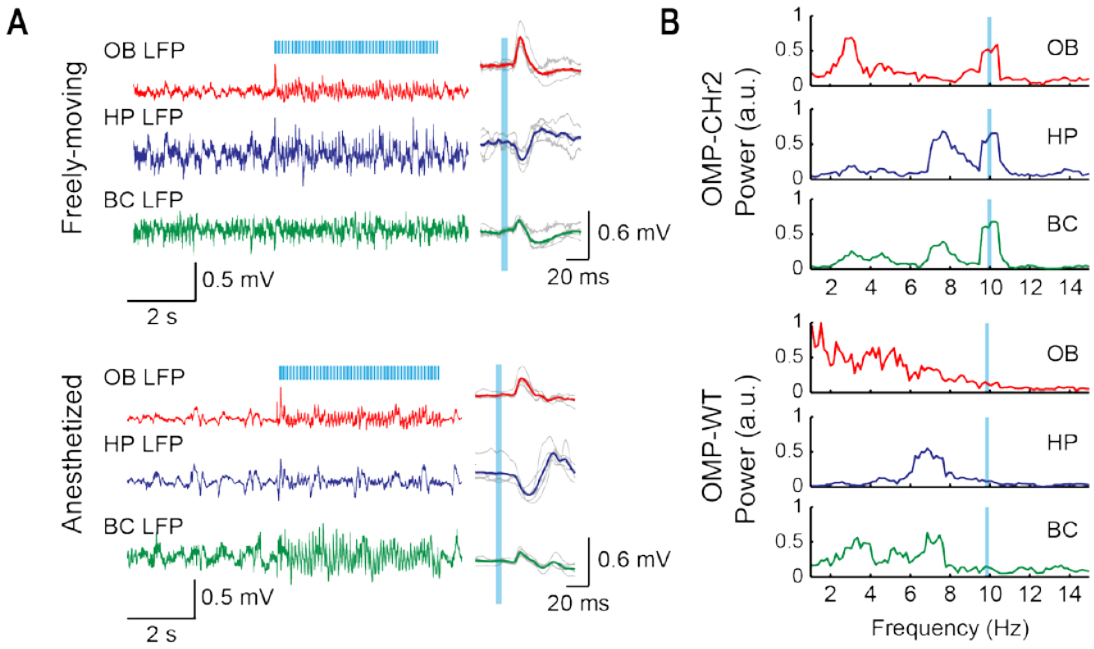
A
Freely-moving
OB LFP
HP LFP
BC LFP
0.5 mV
2 s
0.6 mV
20 ms
Anesthetized
OB LFP
HP LFP
BC LFP
0.5 mV
2 s
0.6 mV
20 ms
B
OMP-CHr2
Power (a.u.)
OB
HP
BC
OMP-WT
Power (a.u.)
OB
HP
BC
Frequency (Hz)

**Figure 2.4. Expression of ChAT in the olfactory tubercle**. **A-B**. An example coronal section from an adult Rosa26$^{iAP}$ mouse that received an intrabulbar injection of AAV-Cre to label the output of the olfactory bulb. A ChAT$^{+}$ cell (expanded in **B**) with an elaborate dendritic morphology is located in the olfactory tubercle where there are overlapping AP$^{+}$ fibers. Scale bar: 0.1 mm.

**Figure 2.4.**

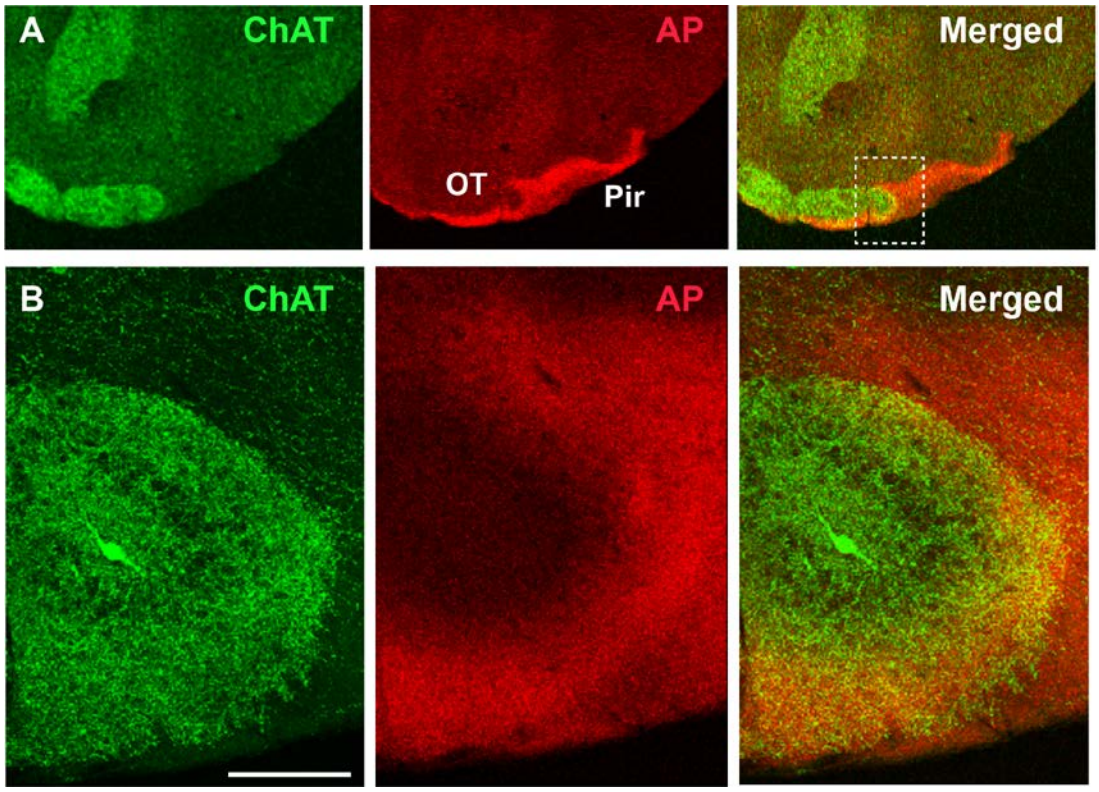

## References


Boyden ES, Zhang F, Bamberg E, Nagel G, Deisseroth K (2005) Millisecond-timescale, genetically targeted optical control of neural activity. Nat Neurosci 8:1263-1268.

Catani M (2017) A little man of some importance. Brain 140:3055-3061.

Chaput MA (1986) Respiratory-phase-related coding of olfactory information in the olfactory bulb of awake freely-breathing rabbits. Physiol Behav 36:319-324.

Cury KM, Uchida N (2010) Robust odor coding via inhalation-coupled transient activity in the mammalian olfactory bulb. Neuron 68:570-585.

Davison IG, Katz LC (2007) Sparse and selective odor coding by mitral/tufted neurons in the main olfactory bulb. The Journal of neuroscience : the official journal of the Society for Neuroscience 27:2091-2101.

Deisseroth K (2011) Optogenetics. Nat Methods 8:26-29.

DeNardo LA, Berns DS, DeLoach K, Luo L (2015) Connectivity of mouse somatosensory and prefrontal cortex examined with trans-synaptic tracing. Nat Neurosci 18:1687-1697.

Fenno L, Yizhar O, Deisseroth K (2011) The development and application of optogenetics. Annu Rev Neurosci 34:389-412.

Houser CR, Crawford GD, Salvaterra PM, Vaughn JE (1985) Immunocytochemical localization of choline acetyltransferase in rat cerebral cortex: a study of cholinergic neurons and synapses. J Comp Neurol 234:17-34.

Ito J, Roy S, Liu Y, Cao Y, Fletcher M, Lu L, Boughter JD, Grun S, Heck DH (2014) Whisker barrel cortex delta oscillations and gamma power in the awake mouse are linked to respiration. Nat Commun 5.

Li J, Ishii T, Feinstein P, Mombaerts P (2004) Odorant receptor gene choice is reset by nuclear transfer from mouse olfactory sensory neurons. Nature 428:393-399.

Li X, Yu B, Sun Q, Zhang Y, Ren M, Zhang X, Li A, Yuan J, Madisen L, Luo Q, Zeng H, Gong H, Qiu Z (2018) Generation of a whole-brain atlas for the cholinergic system and mesoscopic projectome analysis of basal forebrain cholinergic neurons. P Natl Acad Sci USA 115:415-420.

Linster C, Hasselmo ME (2000) Neural activity in the horizontal limb of the diagonal band of broca can be modulated by electrical stimulation of the olfactory bulb and cortex in rats. Neurosci Lett 282:157-160.

Lockmann ALV, Laplagne DA, Leao RN, Tort ABL (2016) A Respiration-Coupled Rhythm in the Rat Hippocampus Independent of Theta and Slow Oscillations. J Neurosci 36:5338-5352.

Madisen L et al. (2012) A toolbox of Cre-dependent optogenetic transgenic mice for light-induced activation and silencing. Nat Neurosci 15:793-802.

Nguyen Chi V, Muller C, Wolfenstetter T, Yanovsky Y, Draguhn A, Tort AB, Brankack J (2016) Hippocampal Respiration-Driven Rhythm Distinct from Theta Oscillations in Awake Mice. The Journal of neuroscience : the official journal of the Society for Neuroscience 36:162-177.

Penfield W (1961) Activation of the Record of Human Experience: Summary of the Lister Oration delivered at the Royal College of Surgeons of England on 27th April 1961. Ann R Coll Surg Engl 29:77-84.

Ravel N, Pager J (1990) Respiratory patterning of the rat olfactory bulb unit activity: nasal versus tracheal breathing. Neurosci Lett 115:213-218.

Sarter M, Bruno JP, Turchi J (1999) Basal forebrain afferent projections modulating cortical acetylcholine, attention, and implications for neuropsychiatric disorders. Ann N Y Acad Sci 877:368-382.

Shusterman R, Smear MC, Koulakov AA, Rinberg D (2011) Precise olfactory responses tile the sniff cycle. Nat Neurosci 14:1039-U1136.

Smear M, Shusterman R, O'Connor R, Bozza T, Rinberg D (2011) Perception of sniff phase in mouse olfaction. Nature 479:397-U149.

Smear M, Resulaj A, Zhang J, Bozza T, Rinberg D (2013) Multiple perceptible signals from a single olfactory glomerulus. Nat Neurosci 16:1687-1691.

Tsanov M, Chah E, Reilly R, O'Mara SM (2014) Respiratory cycle entrainment of septal neurons mediates the fast coupling of sniffing rate and hippocampal theta rhythm. Eur J Neurosci 39:957-974.

Wilson CD, Serrano GO, Koulakov AA, Rinberg D (2017) A primacy code for odor identity. Nat Commun 8:1477.

Yanovsky Y, Ciatipis M, Draguhn A, Tort AB, Brankack J (2014) Slow oscillations in the mouse hippocampus entrained by nasal respiration. The Journal of neuroscience : the official journal of the Society for Neuroscience 34:5949-5964.

# CHAPTER 3: OLFACTORY INPUTS MODULATE RESPIRATION-RELATED ACTIVITY IN THE PREFRONTAL CORTEX AND FEAR BEHAVIOR

## Introduction

We found that OSN stimulation influenced oscillations in the barrel cortex and hippocampus, consistent with the hypothesis that olfactory sensory inputs can modulate the rhythmic activity of distinct brain areas. But what are the functions of LFP oscillations that are normally entrained by nasal breathing? Do they have similar roles in the different regions they are expressed in (e.g. sensory binding in the whisker cortex vs memory organization in the hippocampus)? Given the close relationship between the olfactory system and limbic brain regions mediating emotion and memory, we hypothesized that respiratory-related signals from the olfactory system can influence fear circuits. We focused on the prelimbic prefrontal cortex (plPFC) a region critical for the expression of conditioned fear behavior even though respiratory-related signals reach other limbic regions as well including the nucleus accumbens and amygdala (Karalis and Sirota, 2018).

Since neural rhythms are modulated by respiration in both anesthetized and awake states we reasoned that the 4 Hz activity coupling the plPFC and basolateral amygdala during conditioned freezing is likewise related to respiration. Respiratory-related coupling in the rodent brain is often significantly modulated by sensory signals originating from the olfactory system; they are reduced following removal of the olfactory bulb (Ito et al., 2014) or removing nasal airflow via tracheotomy, (Yanovsky et

al., 2014). We tested if the 4 Hz rhythm was similarly influenced by peripheral olfactory sensory signals by ablating OSNs and inactivating the OB.

### Distinct respiration patterns during freezing

Rodent waking-state respiratory rates are variable, transitioning to as high as 12 Hz while animals explore novel environments, encounter novel odorants, or come across conspecifics (Uchida and Mainen, 2003; Wesson, 2013). We used intranasal thermistor probes that track the warming and cooling of exhaled and inhaled air to characterize respiratory activity during fear expression. Note that junction potentials and differential positioning of thermocouples between animals makes it difficult to interpret the absolute voltage signal during respiration. However, the temporal patterning of inhalations and exhalations can be readily determined on a cycle-by-cycle basis (Angyan and Szirmai, 1967; McAfee et al., 2016). After thermistor implantation we used a simple Pavlovian fear-conditioning paradigm to generate learned fear responses (Rodrigues et al., 2004). Briefly, we paired a ten second pure tone (5 kHz) with a mild foot shock that occurred at the offset of the auditory $CS^+$. Twenty-four hours after fear conditioning mice underwent fear retrieval in a novel environment. After a baseline period of free-exploration, the $CS^+$ was presented four times within twelve minutes. Inter-tone intervals ranged between 120-180 seconds. We observed robust freezing behavior (**Figure 3.1**) following tone presentations (quantified as a percentage of 60 seconds spent freezing following tone onset) as well as during inter-tone intervals. Later presentations of the $CS^+$ evoked less freezing and the percent freezing time following the first tone was significantly higher

than the percent freezing after the last tone (Tukey's multiple comparisons, post hoc Tone 2 vs Tone 4, $p = 0.49$). The total time that mice spent freezing once the tones were presented was 179.75 ±16.23 seconds (mean ± SEM).

We focused on respiratory activity during freezing periods and compared it to respiration during baseline (pre-tone) exploratory periods. During free-exploration, the respiration frequency was rapid and variable as is typical of freely behaving rodents (Kepecs et al., 2007; Rojas-Libano et al., 2014). To characterize the frequency content of breathing signals we estimated the spectral density of simultaneously recorded thermocouple signals and OB LFPs (**Figure 3.2**). The power spectra of signals from baseline periods were characterized by peaks at low frequencies (< 5 Hz) and at 8-10 Hz. Since rodents unlike humans are obligate nose breathers, these frequencies represent basal breathing and sniffing bouts (Negus, 1927). In contrast, during freezing periods, respiration rates became very steady and centered at about 4 Hz. Note that thermocouple signals and OB LFPs are highly correlated and that the breathing rate can be measured directly from thermocouple signals or approximated from low-pass filtered OB LFPs (Rojas-Libano et al., 2014). To determine the respiratory frequency across freezing periods and across mice we estimated the dominant frequency from signals recorded during long, stable freezing epochs (greater than 5 seconds, **Figure 3.3**). While each mouse had its own distinct breathing frequency during these long freezing periods (that varied between mice from 1-2 Hz), the full range of breathing frequencies was between 2-6 Hz with a population average of 4.01 ± 0.13 Hz. These results indicate that fear-related behavioral states (e.g. freezing) are characterized by distinct respiratory patterns in mice. This is consistent with a characterization of the physiological consequences of

$CS^+$ presentations showing that rats have elevated respiration and heart rates during $CS^+$ presentations followed by decreased respiration rates during the freezing periods following $CS^+$ onsets (Frysztak and Neafsey, 1991).

### Correlation between OB and plPFC activity during freezing

Studies reveal a freezing-related 4 Hz oscillation in the plPFC, a structure essential for the expression of freezing behavior (Karalis et al., 2016). Since this frequency overlaps with the breathing rate observed during freezing, we tested whether these two rhythms are correlated. We repeated the auditory-cued fear conditioning experiments in freely behaving animals that were implanted with tungsten electrodes in the OB and plPFC. LPFs recorded in awake-behaving animals that are referenced against a distant point on the skull can be contaminated by non-local and non-neural sources arising from the reference electrode and movement-related noise (Fein et al., 1988; Whitmore and Lin, 2016). We were especially concerned with volume conduction effects which make determining the locality of LFPs difficult. For example, whisker movement-related LFP signals are able to spread to the OB, a few millimeters away (Parabucki and Lampl, 2017). Volume conduction effects can be substantial in monopolar recording arrangements that have a single electrode in a brain region of interest and a reference in a supposedly neutral site. This method detects activity from cortical regions between the recording and reference electrode and integrates the electrical signal with weight inversely proportional to the distance from the electrode. Thus, throughout our experiments we used a bipolar recording configuration to magnify local events (Shirhatti & Ray, Neural computation 2016). Furthermore, in the absence of current-source density

(CSD) analysis we used additional strategies to demonstrate that the plPFC signals were not volume conducted from the OB. For example, we often find that the phase of the 4 Hz signal acquired from bipolar leads in the plPFC is inverted (i.e. there is a nonzero phase difference, **Figure 3.4**). A volume-conducted signal in the plPFC would likely cause a 0° (perfectly in phase) or 180° (antiphase) phase difference between the two electrode leads.

In the OB, LFP recordings were made with tungsten electrodes that penetrated perpendicular to the dorsal surface of the tissue. Thus, electrode tips could end up either dorsal or ventral to the mitral cell layer. Recordings from dorsal vs ventral positioned electrodes have identical shape but inverted polarity because the architecture of the OB forms an electric dipole with zero isopotential difference near the mitral cell layer (Freeman, 1972). For all analyses OB LFPs were transformed offline to have the same polarity.

During freezing, oscillations in the simultaneously recorded LFPs were dominated by a low frequency component at ~4 Hz and were strongly coupled as illustrated by time-frequency coherogram plots and population averaged coherence spectrums (**Figure 3.5, 3.6**). Since each mouse had a slightly different breathing frequency (centered around 4 Hz) we also quantified the peak value of OB-plPFC coherence spectrums from freezing periods and non-freezing time periods taken from the free-exploration baseline before the onset of $CS^+$ tones. The peak coherence significantly increased from non-freezing to freezing periods. Similarly, the cross correlation between the OB and plPFC significantly increased during freezing (**Figure 3.6**). We also extracted the instantaneous phase from the 2-6 Hz filtered signals and quantified the phase-locking value (PLV) in the manner of

Lachaux et al., 1999. PLV measures the variability of the phase difference; if the phase difference is consistent the PLV is close to 1 and is close to zero otherwise (Lachaux et al., 1999). PLVs were significantly greater during freezing. Furthermore, circular distribution analysis of the OB and plPFC phase differences during freezing revealed a 13.5° phase difference (or time lag of about 10 ms) suggesting that the plPFC oscillations were not a result of volume conduction from the OB.

In rodents, freezing is considered a state of attentive immobility that helps the animal avoid detection by predators and may serve to enhance perception (Lojowska et al., 2015). It occurs in response to both conditioned (learned) or unconditioned stimuli. We were interested in freezing that was caused by innately fearful odor stimuli and used the synthetic analog of fox predator odor (2MT, 1:1000 in mineral oil) to evoke robust innate freezing responses. We monitored respiratory activity and OB and plPFC LFPs before and after the addition of 2MT (**Figure 3.7**). Following exposure, we found that respiratory patterns were different and characterized by lower frequencies during extended freezing periods. Surprisingly, low frequency respiratory-related oscillations in the OB and plPFC persisted during freezing periods even though the plPFC is considered dispensable for this kind of innate behavior (Chan et al., 2011).

Overall, these results reveal that the rhythmic activity in the plPFC is coupled to respiration-related OB oscillations during conditioned and innate freezing behavior. Presumably, respiration-related OB activity during freezing is correlated with activity in brain regions that express respiratory rhythms under normal conditions (e.g. the barrel cortex and dentate gyrus). We focused extensively on the plPFC but in a few cases also recorded LFP signals from other brain regions to determine if the 4 Hz signal during

freezing is entirely global (i.e. expressed in every brain regions). Recordings from the medial septum which plays a critical role in regulating the theta rhythmicity of the hippocampus (Stumpf et al., 1962) do not show 4 Hz activity during freezing (**Figure 3.8**). Likewise, electrodes in the CA1 region of the hippocampus show some activity in the 2-6 Hz frequency range but other rhythms are present and seem to dominate (Seidenbecher et al., 2003).

### The contribution of olfactory inputs to rhythmic activity in the plPFC

Respiration-correlated oscillatory activity in the plPFC might be *1*) intrinsically generated by the network, *2*) influenced by brainstem centers, and *3*) modulated by respiration-entrained olfactory inputs. These possibilities are not mutually exclusive and in fact they could all contribute to rhythmic activity in the plPFC. To test the second possibility, we observed conditioned freezing responses in low oxygen conditions (10% $O_2$) under which breathing rates are increased (Bleymehl et al., 2016). Given the increased physiological respiratory drive we wondered if the respiration-related activity in the plPFC during freezing would likewise increase in frequency. This would support the hypothesis that brainstem respiratory centers can entrain the 4 Hz freezing-related rhythm. However, the plPFC rhythm during freezing was still ~4 Hz under low $O_2$ conditions in three animals suggesting that the plPFC rhythm overwrites the physiological drive for faster breathing (**Figure 3.9**). Thus, we focused on the third scenario: that nasal airflow and/or signals from the peripheral olfactory system contribute to the plPFC rhythm during freezing.

We used a within-subject, unilateral naris occlusion approach to block nasal airflow on one side of the animal since the ascending olfactory pathway is primarily ipsilateral (Shipley and Adamek, 1984; King and Hall, 1990) and subsequent tracing experiments suggested connectivity between olfactory prelimbic regions is ipsilateral. Mice were implanted bilaterally with electrodes on both sides of the OB and plPFC. Then, animals underwent unilateral naris occlusion before subsequent fear conditioning. Naris occlusion blocks airflow as well as odorant-evoked signals; if sensory drive from the olfactory nerve is interrupted by tracheotomy, naris closure, or nerve transection the high-amplitude oscillations related to breathing are essentially abolished (Gray and Skinner, 1988; Courtiol et al., 2011). The loss of nasal airflow is especially evident in decreased respiration-related oscillations in OB LFPs on the occluded side in the anesthetized state (**Figure 3.10**). Under anesthesia, top-down cortico-bulbar feedback projections from olfactory cortex and neuromodulator centers are offline (Kiselycznyk et al., 2006; Matsutani and Yamamoto, 2008). Thus, in this state activity in the OB is bottom up and driven almost entirely by respiratory signals.

Under awake-behaving conditions unilateral naris occlusion did not influence freezing behavior which may be due to intact olfactory inputs on the open side. However, during freezing periods we observed a significant reduction in the peak coherence and cross correlation between OB and plPFC signals during freezing on the closed side compared to the open side (**Figure 3.11**). These results support a role for nasal airflow in modulating the plPFC rhythm in conditioned fear behavior. In fact, this approach may underestimate the contribution of olfactory inputs due to potentially incomplete naris closure, residual respiration-related inputs to the OB in the occluded side via contralateral

AON connections, and reciprocal connectivity between the open and occluded-side plPFC(Illig and Eudy, 2009; DeNardo et al., 2015).

### Connectivity between the olfactory pathway and plPFC

The plPFC integrates information from diverse brain regions involved in a variety of cognitive functions and behaviors beyond fear processing (Ongur and Price, 2000; Miller and Cohen, 2001). As a high level structure it receives long range inputs to layer V including dorsal sensory thalamic inputs, anterior cingulate regions, and motor cortex. We explored the anatomical pathway by which respiration-related olfactory inputs could reach the plPFC using anterograde and retrograde tracing approaches. First, we used the retrograde transducing Canine Adenovirus Type 2 expressing *Cre* (CAV2-Cre) (Gore et al., 2013). CAV2 is a good strategy for retrograde Cre delivery as CAV viral vectors are largely restricted to transduction of neurons, are stably expressed, and not neurotoxic (Kremer et al., 2000). We focally injected the CAV2-Cre virus into one side of the plPFC in Rosa26-floxed-tdTomato reporter mice (n = 3) and examined patterns of tdTomato expression four weeks later. Among the OB and olfactory cortices which receive direct olfactory inputs from the OB we observed tdTomato$^{+}$ cell bodies in the ipsilateral AON and taenia tecta (**Figure 3.12**). Previous tracing experiments also reported a proportion of inputs to the medial prefrontal cortex arising from these olfactory regions (Hoover and Vertes, 2007; DeNardo et al., 2015).

In a complimentary experiment, we injected Cre-dependent channelrhodopsin (ChR2)-EYFP virus into the AON of Vglut1-Cre mice (n = 3) to label glutamatergic pyramidal neurons in the AON. Four weeks later, labeled axonal fibers were found in

both the prelimbic (PL) and infralimbic (IL) prefrontal cortex ipsilateral to the injection. The preferential targeting of excitatory AON/TT projections is interesting because the AON/TT is the target of OB tufted cells which are increasingly thought to represent a distinct functional pathway from mitral cells.

Mitral and tufted bulbar outputs can be anatomically and functionally segregated into two classes. Mitral cells project to anterior and posterior olfactory cortical areas while tufted cells send axons only to anterior areas of olfactory cortex (e.g. AON) (Haberly and Price, 1977; Scott, 1981; Igarashi et al., 2012). This segregation extends to the physiological properties and odorant responses of the two types of OB cells. Tufted cells respond to odorants with a shorter temporal latency. They are also more broadly tuned (Nagayama et al., 2004). OSN axon terminals synapse directly onto a TC subtype (external tufted cells) and provide strong, short-latency excitation (De Saint Jan et al., 2009). Furthermore, MCs and TCs lock to distinct phases of the sniff cycle and can be used to help identify the cell classes when other means of distinguishing the two are unavailable (Fukunaga et al., 2012).

One implication of these functional differences (especially the temporal differences) is that TC work in a regime where time is crucial while MC may be involved in cases where information is integrated and complimentary cognitive processing takes place. Along similar lines, we propose that since TCs receive strong breathing-related inputs from OSNs they may specifically provide airflow information to anterior olfactory cortical areas that can target the prefrontal cortex. This pathway specific hypothesis, although not tested here, could be further explored by specifically by blocking these AON outputs to plPFC.

To confirm that AON projections make synaptic contacts with excitatory cells in the prefrontal cortex we injected Cre-dependent channelrhodopsin (ChR2)-EYFP virus into the AON of Vglut1-Cre mice. Since these animals were also Vglut1-tdTomato$^+$ we used coronal brain slices that included the prelimbic and infralimbic prefrontal cortex where excitatory cells could be visualized. These presumably pyramidal cells in all layers of the prefrontal cortex were targeted for patch clamp recordings while the terminals of AON projections were photostimulated. Light-evoked excitatory currents (that could be blocked by the AMPA channel antagonist CNQX) were observed in a majority of cells (**Figure 3.13**). The short and stable latencies between photostimulation and recorded currents suggest a monosynaptic connection between AON projections and a subset of Vglut$^+$ cells in the prefrontal cortex. These results suggest that there is a functional connection between the AON and pyramidal cells in the PL and IL prefrontal cortex.

### OSN Stimulation entrains plPFC rhythms

Given the described functional connectivity between the olfactory system and the plPFC we used an optogenetic strategy to activate OSNs in the nasal epithelium while recording LFPs from the plPFC in freely-moving mice. We stimulated OSNs at 13 Hz which is a frequency at the upper limit of endogenous sniffing rhythms – sniff bouts are not sustained at higher frequencies for very long (Wesson et al., 2008). Activation of OSNs entrained LFP activity in both the OB and plPFC (**Figure 3.14**) in mice expressing ChR2 in OSNs but not in control animals (littermates not expressing ChR2). These data support a previously underappreciated neural connection that links the olfactory system

with the prefrontal cortex that could support the frequency-specific coupling observed during freezing.

### Loss of olfactory inputs leads to prolonged freezing

To investigate the functional consequences of disrupting olfactory inputs on fear circuitry and behavior we acutely lesioned the nasal epithelium. The antithyroid drug methimazole causes tissue-specific toxicity in olfactory mucosa presumably due to extensive damage of supporting architecture such as Bowman's glands and sustentacular cells (Brittebo, 1995; Bergstrom et al., 2003; Xie et al., 2011). In mice given a single intraperitoneal injection of methimazole there is detachment of the olfactory epithelium from the basal cell layer 24 hours after administration. We used a single dose (75 mg/kg) to induce destruction of the epithelium and four days later stained tissue sections using antibodies against OMP to label mature olfactory sensory neurons and SUS-4 to label supporting cells. OSNs are essentially absent from the OE and at this time point regrowth of sensory inputs is minimal (Suzukawa et al., 2011). Similar to naris occlusion, removal of OSN inputs via methimzole treatment reduced the coupling between OB LFPs and respiration (**Figure 3.15**). The reduction in coupling strength (quantified by the peak coherence between the signals) was significantly reduced in both the awake and anesthetized states. However, we noted that in unanesthetized mice there remains some residual coupling that is presumably mediated by top-down inputs that are offline under anesthesia (control awake n = 7, methimazole treated awake n = 5, control anesthetized n = 5, and methimazole anesthetized n = 5). We used the coherence between shuffled OB and respiratory signals to determine a lower bound on expected coherence levels.

Methimazole treatment did not change baseline breathing rates during normal home-cage behavior when we recorded respiration rates over long periods of time (n = 4). Furthermore, methimazole treated mice do not have different breathing patterns during fear conditioned freezing behavior (i.e. they still breathe at ~4 Hz during freezing n = 2).

A group of methimazole treated mice (n = 9) underwent the auditory fear conditioning and fear retrieval paradigm four days after drug injection (**Figure 3.16**). Removing olfactory inputs reduced 4 Hz activity in the plPFC during freezing behavior although it was not eliminated. The coherence between LFPs recorded from OB and plPFC was low and did not significantly increase during freezing periods even though a peak at the respiration rate (~4 Hz) was still evident. Peak coherence during freezing did not reach the same levels as in control mice (methimazole treated $0.59 \pm 0.04$ n = 9, compared to control $0.88 \pm 0.03$ n = 8, U = 1.5 p = 0.0002 in two tailed Mann-Whitney test). Consistently, the cross correlation between the OB and plPFC did not increase in methimazole treated animals during freezing periods. Circular distribution analysis failed to reveal the consistent phase difference between OB and plPFC signals during freezing as observed in control animals. Furthermore, the phase locking value was not increased during freezing periods.

The onset of conditioned freezing corresponds with the emergence of 4 Hz oscillations in the plPFC and BLA. Grainger Causality analysis of these highly correlated LFP signals suggested that the plPFC leads the BLA supporting the idea that the plPFC entrains activity in the BLA (Karalis et al., 2016). To demonstrate a causal role of oscillatory activity in fear behavior investigators activated ChR2-expressing parvalbumin$^{+}$ interneurons in the prefrontal cortex to generate 4-Hz oscillations and

induced fear behavior. The results suggest that 4 Hz activity is positivity correlated with freezing. We reasoned that influencing rhythmic activity in the plPFC by disrupting olfactory inputs would in turn disrupt freezing behavior. However, methimazole treated mice still showed freezing behavior during the retrieval session indicating that olfactory inputs are indispensable in the acquisition and expression of auditory-cued fear behavior.

In fact, when we quantified freezing times, methimazole treated animals had significantly longer freezing periods compared to control and unilaterally naris occluded mice (**Figure 3.17**). This was not due to non-specific decreases in locomotion after methimazole treatment since pre-tone baseline freezing time was not significantly different among the three groups. These results suggest that without olfactory inputs freezing time during fear retrieval is increased even though 4 Hz oscillations in the plPFC are significantly decreased (although not entirely removed).

Since methimazole treatment may have other non-olfactory and off target effects like hepatotoxicity (Woeber, 2002), we used an alternative strategy to confirm that disruption of olfactory inputs could prolong freezing periods. We bilaterally inactivated the OBs of cannulated mice with tetrodotoxin (TTX, 0.5 µl, 60 µM) before the fear retrieval test. LFP recordings taken from TTX inactivated OBs showed a dramatic loss of oscillatory activity (which requires coordinated temporal firing of excitatory and inhibitory cell populations in the bulb, **Figure 3.18**). During the fear retrieval session TTX treated mice had longer freezing periods as compared to saline infused control mice, similar to results found using methimazole. However, in contrast to ablation of sensory neurons, acute inactivation of OB networks also increased baseline (pre-tone) freezing times. This suggests that disruption of the OB and ablation of the OE have somewhat

differential effects on conditioned fear behavior. The latter treatment spares intrinsic and centrifugal inputs which leaves residual respiration-entrained activity in the OB. Despite spending more time freezing, TTX treated mice did not show a change in total distance traveled pre-tone compared to control mice. This is consistent with reports that bulbectomized rodents have differences in baseline exploratory behavior including hyperactivity in the open field (Song and Leonard, 2005; Zueger et al., 2005; Hendriksen et al., 2015). Note that we chose acute ablation of the OE instead of a genetic manipulation to disrupt OSNs in large part due to the profound effects on emotion and behavior caused by bulbectormy and/or chronic removal of olfactory sensory inputs (as discussed in the Introduction). Genetically modified mouse lines with disrupted sensory input have an anxiety-like phenotype (Glinka et al., 2012; Chen et al., 2014). In addition, inducible knockout of key olfactory signaling molecules in OSNs is likely compromised by the continuous neurogenesis of OSNs in the epithelium (Costanzo, 2005).

**Figure 3.1. During retrieval session mice show robust conditioned freezing behavior**. **A.** Example freezing behavior of a single mouse over the course of the retrieval session. Freezing (indicated in blue) is observed following tone presentations but also during inter-tone intervals. **B.** Quantification of freezing behavior for 8 mice expressed as a percentage of time spent freezing in the 60 s period after each tone presentation. The pre-tone freezing is measured in the 60 s period before the first tone is presented. Percent time spent freezing is significantly different between the first tone and the last tone (55 ± 6.35 % vs 32.71 ± 4.76 %, One-way ANOVA, $F(4,7) = 3.91$. Tukey post hoc, Tone 1 vs Tone 4, $p = 0.01$). **C**. Total freezing time in seconds before (pre-tone, 12.88 ± 3.40 s) and after (post-tone, 179.75 ± 16.23s) tone presentations.

**Figure 3.1.**

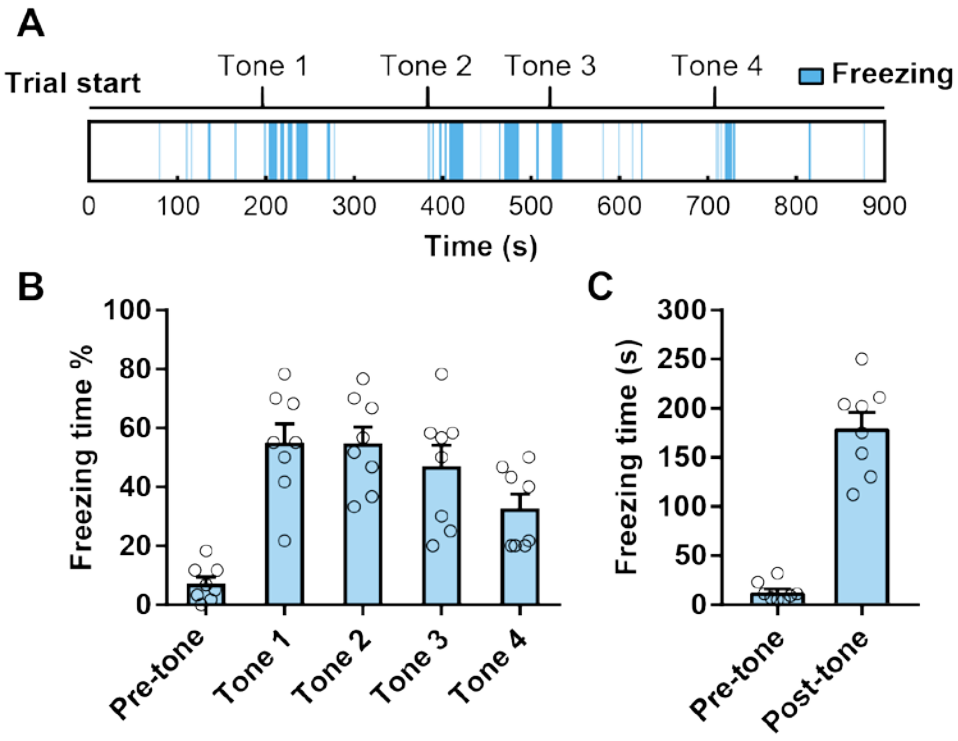
A
Trial start
Tone 1
Tone 2
Tone 3
Tone 4
Freezing
0
100
200
300
400
500
600
700
800
900
Time (s)
B
Freezing time %
100
80
60
40
20
0
Pre-tone
Tone 1
Tone 2
Tone 3
Tone 4
C
Freezing time (s)
300
250
200
150
100
50
0
Pre-tone
Post-tone

**Figure 3.2. Freezing and nonfreezing periods are characterized by differences in respiratory frequency. A**. Power spectrum of thermocouple and local field potential signals and OB LFP recordings from a single mouse during a non-freezing (pre-tone baseline) period. The unfiltered traces used to calculate the power spectrum are shown to the right, with downward deflections in the thermocouple signal indicating inhalations. **B**. Power spectrum and raw traces from the same mouse during freezing. Note the increased power at approximately 4 Hz. In both cases (non-freezing and freezing) note the similarity of the thermocouple and OB LFP signals indicating that the low frequency component of the OB LFP represents nasal airflow.

**Figure 3.2.**

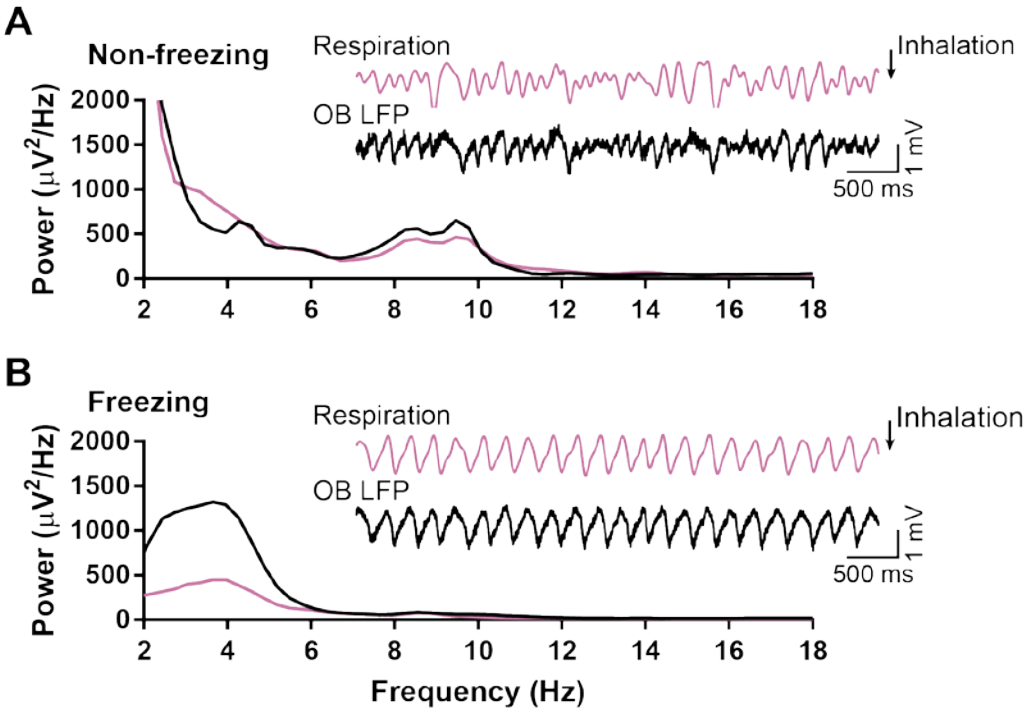
A
Non-freezing
Respiration
Inhalation
OB LFP
1 mV
500 ms
Power (μV²/Hz)
2000
1500
1000
500
0
2
4
6
8
10
12
14
16
18
B
Freezing
Respiration
Inhalation
OB LFP
1 mV
500 ms
Power (μV²/Hz)
Frequency (Hz)

**Figure 3.3. Summary of respiratory activity during conditioned fear behavior. A.** The instantaneous (cycle-to-cycle) respiratory frequency aligned to a freezing period from individual mice (n = 8). Top: a raw thermocouple trace from an example animal (mouse 8). Bottom: the instantaneous frequency of either thermocouple (Mice 1-4) or low-pass filtered OB LFPs (Mice 5-8) aligned to the onset of a freezing period (freezing onset at 5 s). **B.** The respiratory frequency of each mouse during long, continuous freezing episodes longer than 5 s is estimated by peaks in the power spectrum of either thermocouple or low-pass filtered OB LFPs. The overall average for all mice is 4.05 ± 0.13 Hz (indicated by the dashed-line). **C.** The percent power in the 2-6 Hz frequency band is increased during freezing as compared to non-freezing baseline periods (51.20 ± 3.22 to 73.23 ± 2.13, n = 8 paired two-tailed Student's t test $t(7) = 9.67$, $p < 0.001$).

**Figure 3.3.**

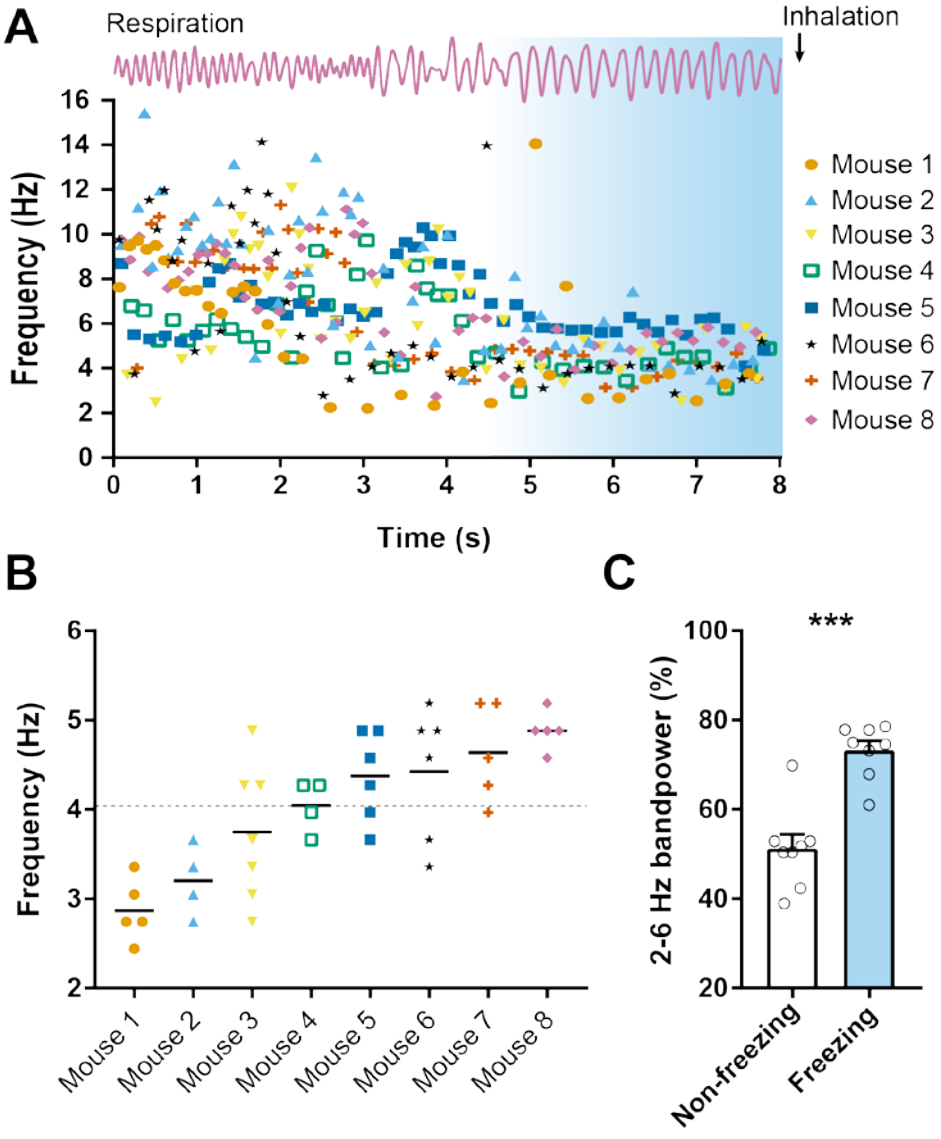
A
Respiration
Inhalation
Frequency (Hz)
Time (s)
Mouse 1
Mouse 2
Mouse 3
Mouse 4
Mouse 5
Mouse 6
Mouse 7
Mouse 8
B
Frequency (Hz)
Mouse 1
Mouse 2
Mouse 3
Mouse 4
Mouse 5
Mouse 6
Mouse 7
Mouse 8
C
***
2-6 Hz bandpower (%)
Non-freezing
Freezing

**Figure 3.4. Partial reversal of the LFP signal across the two electrode contacts within the plPFC suggests the 4 Hz signal is not the result of volume conduction.** Example recordings of respiration and plPFC LFPs during a freezing period. Signals from both electrodes leads (lead 1 and lead 2) are shown. Filtered (2-6 Hz) LFPs are shown overlaid on raw traces (in gray). Beneath the LFPs are the phase-representations of the filtered signals obtained via the Hilbert Transform. The phase offset between the two 4 Hz signals suggests that the 4 Hz signal is not the result of volume conduction.

**Figure 3.4.**

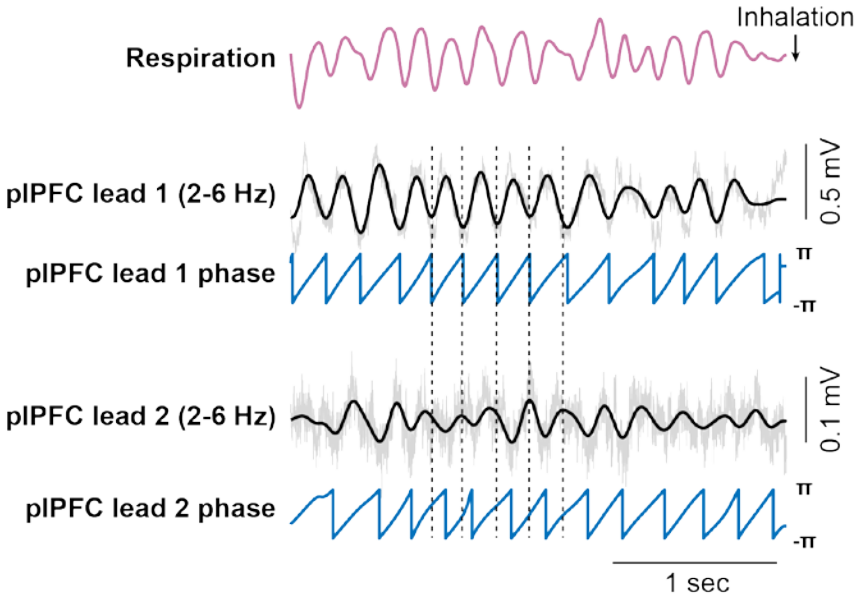
Respiration
Inhalation
plPFC lead 1 (2-6 Hz)
0.5 mV
plPFC lead 1 phase
π
-π
plPFC lead 2 (2-6 Hz)
0.1 mV
plPFC lead 2 phase
π
-π
1 sec

**Figure 3.5. During conditioned freezing neural activity in the OB and plPFC is dominated by highly correlated 4 Hz oscillations. A.** An example of OB and plPFC LFPs recorded during a freezing epoch. Filtered signals (2-6 Hz) are overlaid on raw traces (in gray). Nissl-stained coronal brain sections show the location of LFP electrodes in the OB and plPFC. Scale bars, 0.5 mm top and 1.0 mm bottom. **B.** Time-frequency cohereogram of OB and plPFC LFPs recorded from another mouse during a portion of the fear retrieval session. Observed freezing periods are marked above in blue. High phase coherence between the two signals emerges during periods of freezing.

**Figure 3.5.**

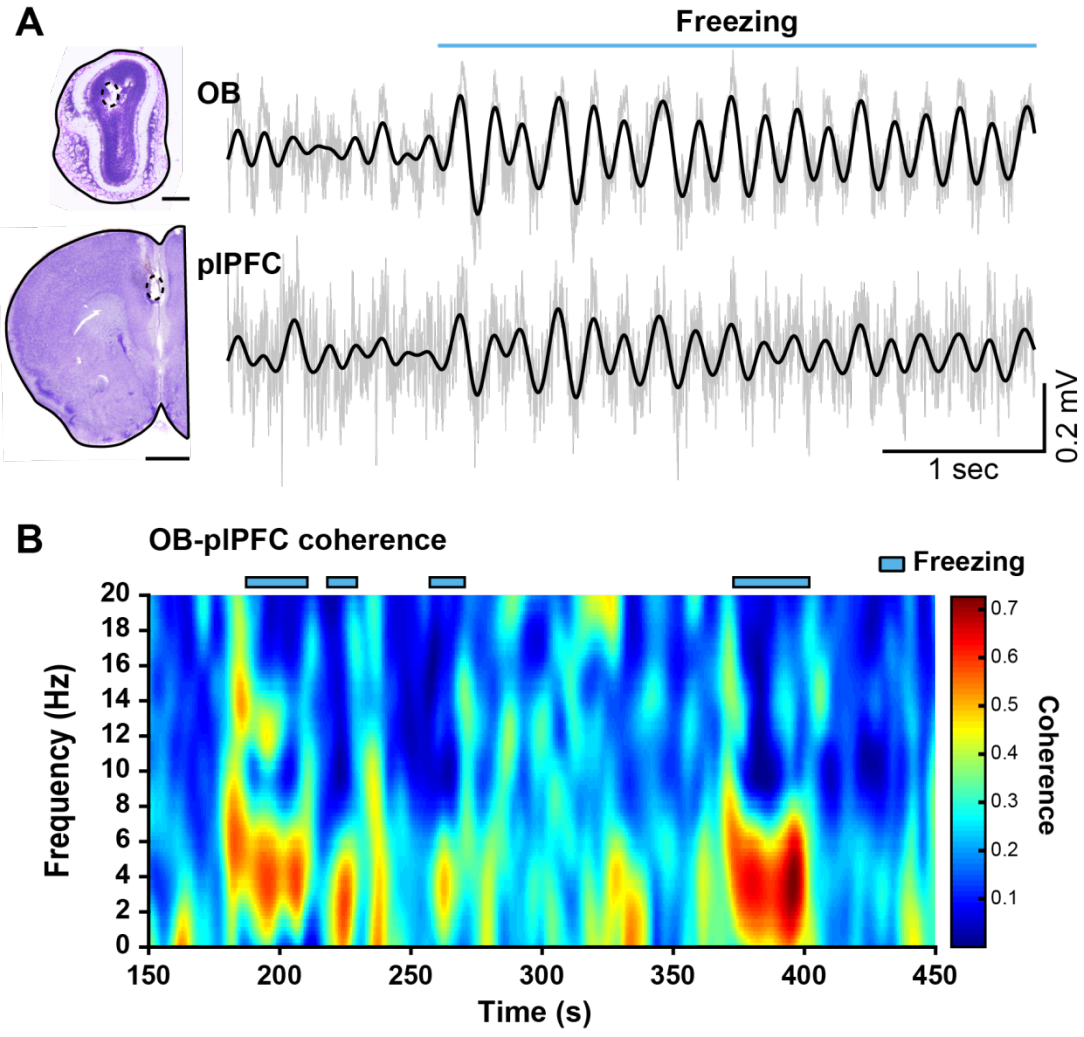
A
Freezing
OB
plPFC
0.2 mV
1 sec
B
OB-plPFC coherence
Freezing
Frequency (Hz)
Time (s)
Coherence

**Figure 3.6. Summary of the relationship between OB and plPFC signals during freezing. A.** Spectral coherence between simultaneously recorded OB and plPFC LFPs during non-freezing (from pre-tone baseline periods, in black) and freezing (blue) periods (displayed as mean ± SEM, n = 8 mice). Note the large peak at ~4 Hz. Inset, averaged peak coherence value for non-freezing and freezing episodes (0.69 ± 0.06 to 0.88 ± 0.03, n = 8, Wilcoxon matched-pairs signed rank test, $p = 0.016$). **B.** Example cross and auto correlations between filtered (2-6 Hz) OB and plPFC signals recorded during freezing. In this example the peak cross correlation is 0.92 with a lag of about 5 ms. **C.** All animals tested showed an increase in the peak OB-plPFC cross-correlation value from non-freezing to freezing periods (0.34 ± 0.04 to 0.75 ± 0.07, n = 8, paired two-tailed Student's *t* test $t(7) = 5.75$, $p < 0.001$. **D.** The phase locking value (between the OB and plPFC) for each mouse increased from freezing to non-freezing periods (0.39 ± 0.06 to 0.72 ± 0.07, n = 8, paired two-tailed Student's *t* test $t(7) = 5.18$, $p = 0.001$). **E.** Circular distribution of phase differences between OB and plPFC 2-6 Hz signals during freezing in 8 mice. The mean direction of the distribution is 13.5° (red line, with lower 95% confidence limit = 13.0 and upper 95% confidence limit = 14.0, $p < 0.001$ in one-sample test for mean angle equal to 0°). The phase distribution is also visualized as a radial histogram (30 bins) surrounding the polar plot.

**Figure 3.6.**

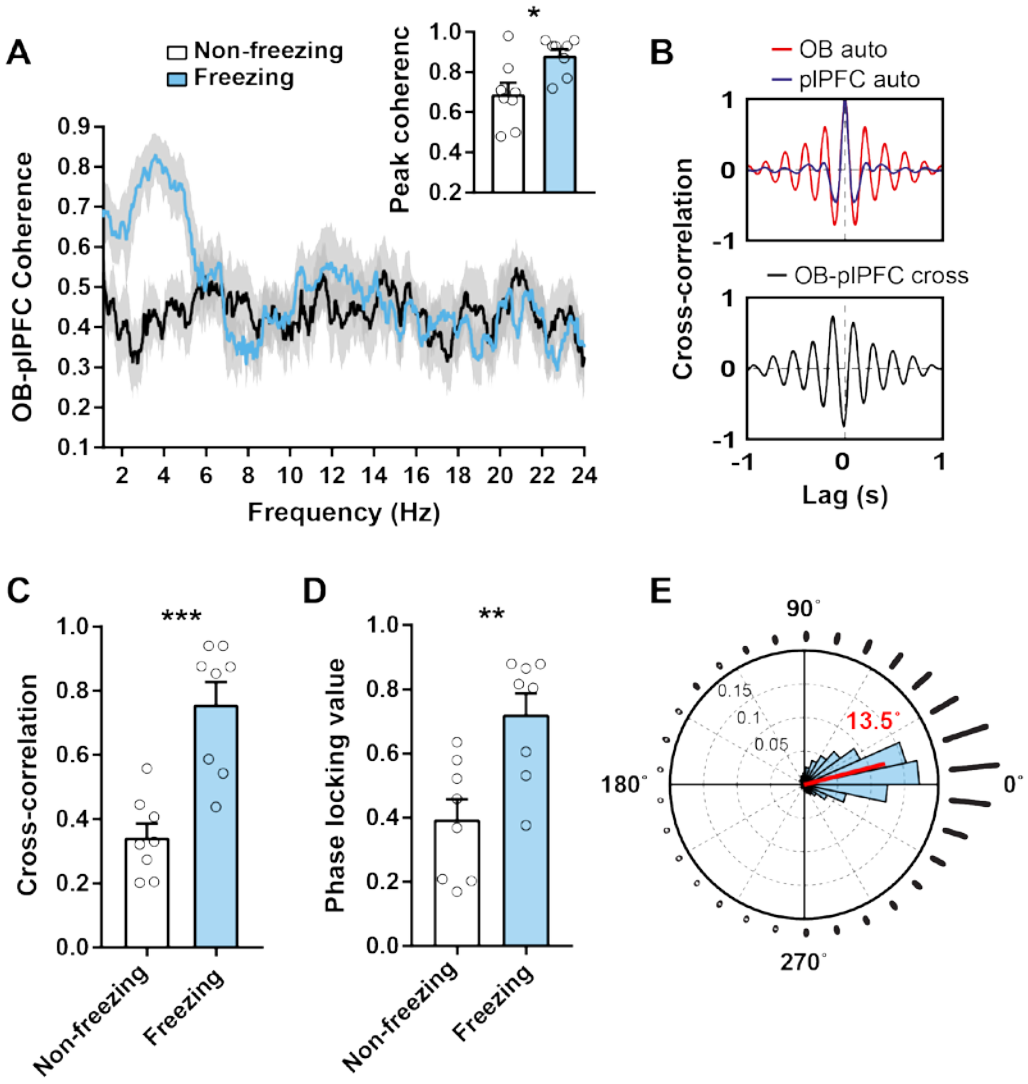
A
Non-freezing
Freezing
OB-pIPFC Coherence
Frequency (Hz)
Peak coherenc
*
B
OB auto
pIPFC auto
OB-pIPFC cross
Cross-correlation
Lag (s)
C
***
Cross-correlation
Non-freezing
Freezing
D
**
Phase locking value
Non-freezing
Freezing
E
90°
180°
0°
270°
13.5°

**Figure 3.7. During innate freezing respiration is slow and neural activity in the OB and plPFC is correlated at the breathing frequency. A.** 5 min exposure to 2-Methyl-thiazoline (2MT) a synthetic analog of the fox odor TMT causes avoidance and periods of behavioral freezing. **B**. Thermocouple recording from the 2MT exposure with periods of observed freezing indicated in blue. Insets show segments of thermocouple signal in an expanded time base. **C.** Nissl-stained coronal section showing the location of LFP electrode in the plPFC. Scale bar, 1 mm. **D.** An example of OB and plPFC LFPs recorded during a freezing epoch. Filtered signals (2-6 Hz) are overlaid on raw traces (in gray).

**Figure 3.7.**

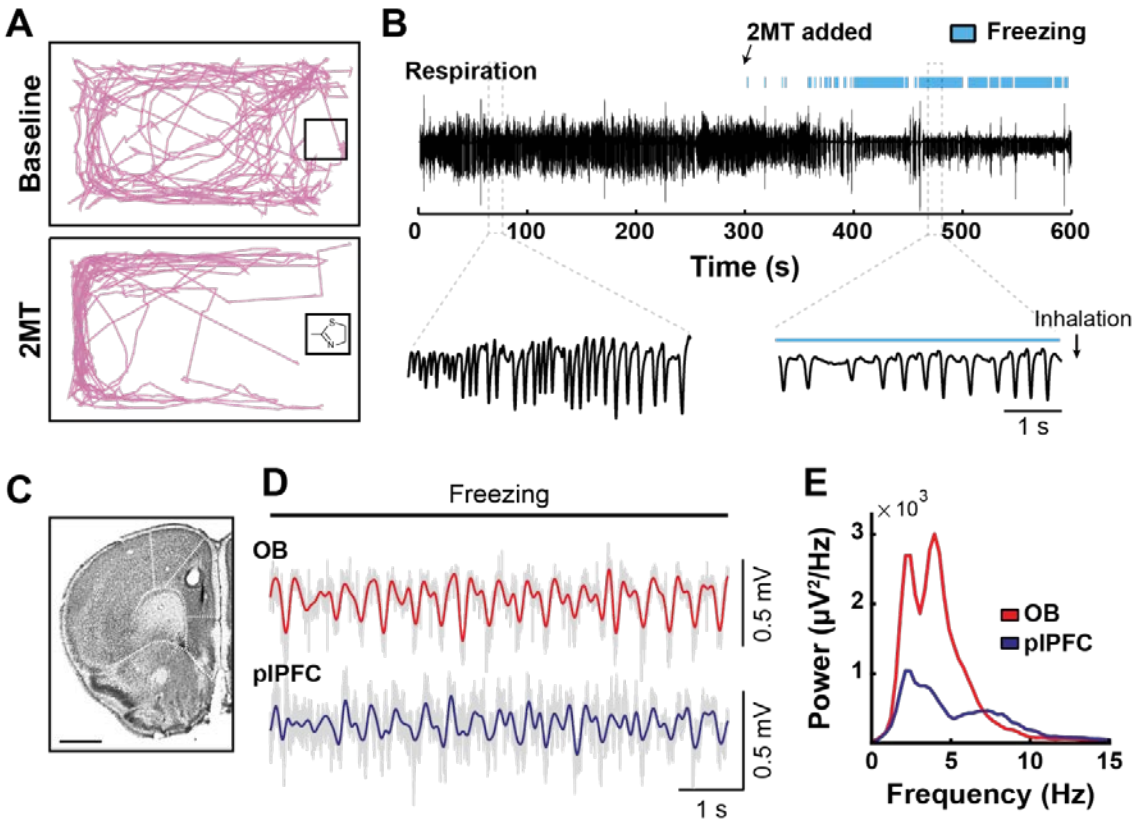
A
Baseline
2MT
B
2MT added
Freezing
Respiration
0
100
200
300
400
500
600
Time (s)
Inhalation
1 s
C
D
Freezing
OB
0.5 mV
plPFC
0.5 mV
1 s
E
× 10^3
3
2
1
Power (μV²/Hz)
OB
plPFC
0
5
10
15
Frequency (Hz)

**Figure 3.8. 4 Hz LFP oscillations during freezing are not globally expressed in every brain region. A.** Nissl-stained coronal brain sections show the location of an LFP electrode in the medial septum (dashed circle). Scale bar, 1.0 mm. CTX cortex, CPu caudoputamen, PIR piriform cortex, aca anterior commissure, OT olfactory tubercle. **B.** Unfiltered LFP recordings from the OB and the medial septum during freezing behavior (indicated in blue). There are strong ~4 Hz oscillations in the OB signal that are not observed in the medial septum trace. **C.** Nissl-stained coronal brain sections show the location of an LFP electrode in the hippocampus (CA1 region). Scale bar, 1.0 mm. **D.** Unfiltered thermocouple and LFP recordings from the OB and CA1 during freezing behavior.

**Figure 3.8.**

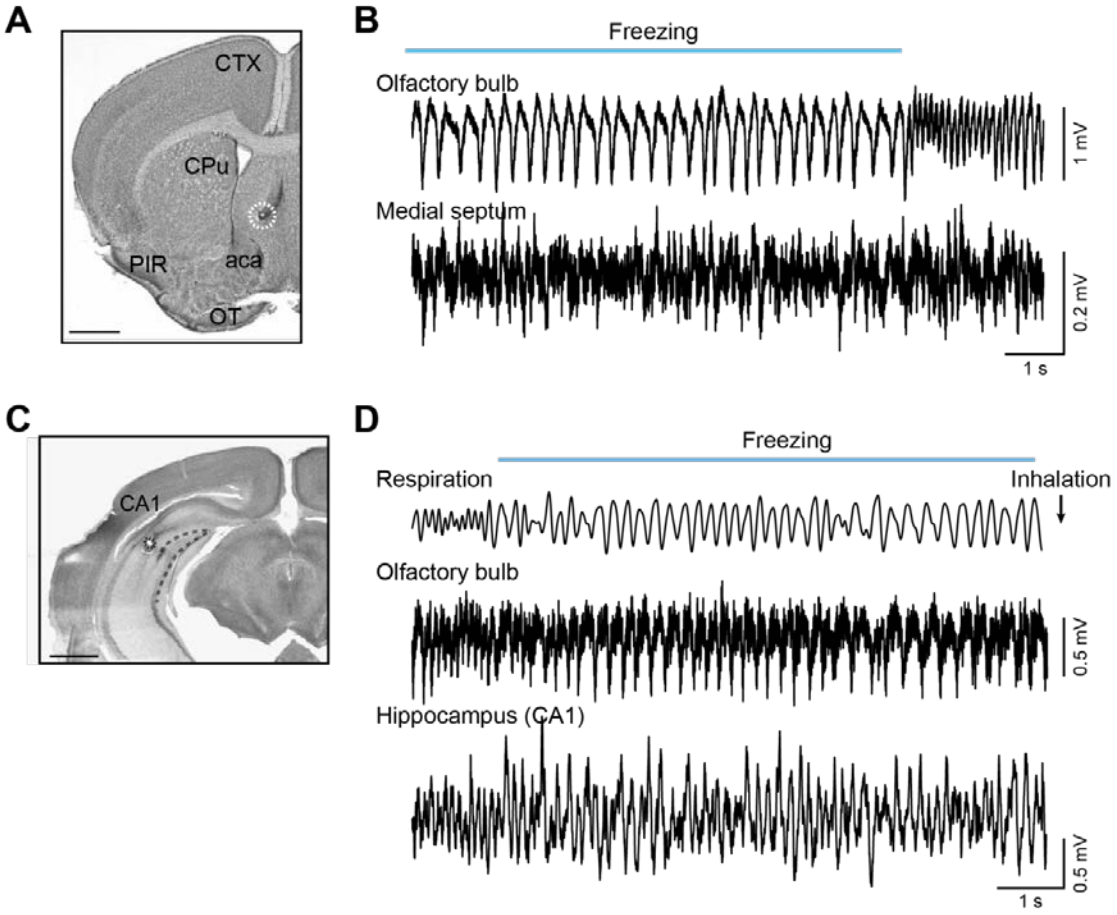
A
CTX
CPu
PIR
aca
OT
B
Freezing
Olfactory bulb
1 mV
Medial septum
0.2 mV
1 s
C
CA1
D
Freezing
Respiration
Inhalation
Olfactory bulb
0.5 mV
Hippocampus (CA1)
0.5 mV
1 s

**Figure 3.9. Respiration and plPFC oscillations during freezing in low oxygen conditions remain at 4 Hz. A.** Nitrogen is added to the chamber to gradually reduce the percentage of oxygen. A stable concentration of 10% is reached at about 150 seconds. The fear retrieval session begins at 175 seconds and continues for 900 seconds. **B.** The instantaneous (cycle-to-cycle) respiratory frequency aligned to a freezing period from an individual mouse. **C.** Left, power spectra computed from segments of unfiltered plPFC LFP recordings (n = 3 mice) during conditioned freezing periods in low oxygen conditions. All three animals tested show large peaks at ~4 Hz. Right, representative LFP (2-6 Hz filtered shown overlaid on raw traces) from the plPFC during a freezing period in one mouse.

**Figure 3.9.**

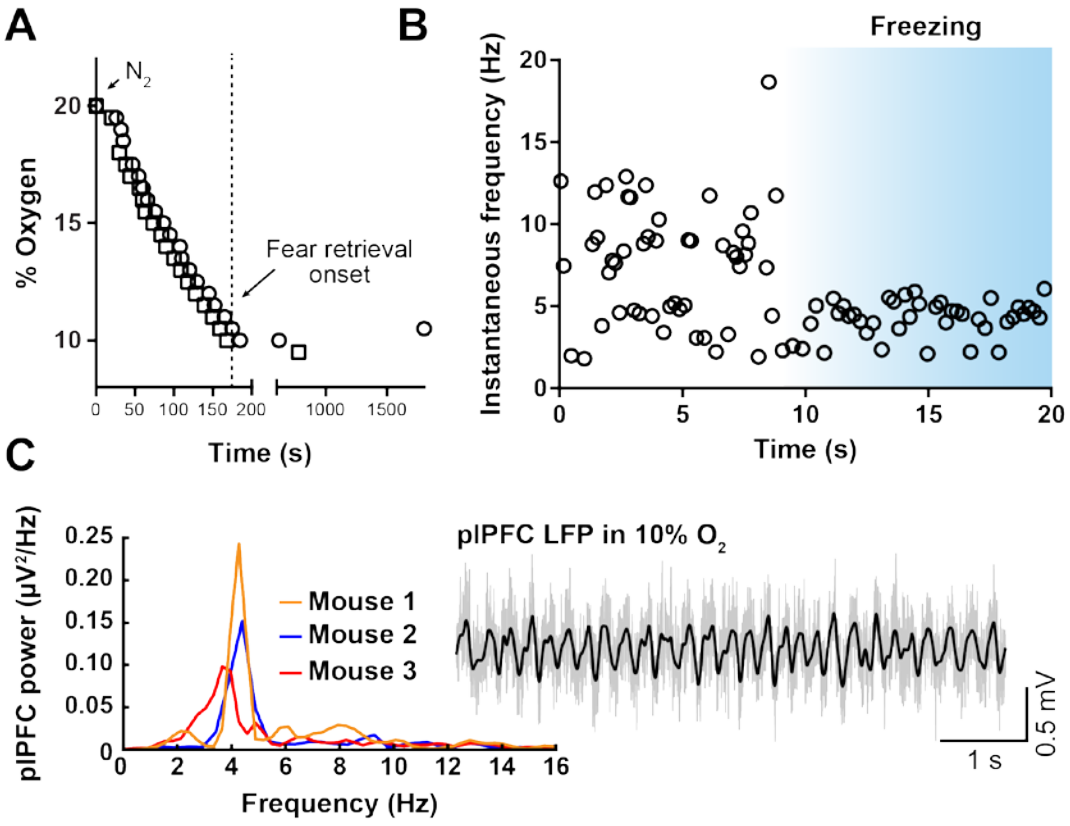
A
N2
% Oxygen
20
15
10
0
50
100
150
200
1000
1500
Fear retrieval onset
Time (s)
B
Freezing
Instantaneous frequency (Hz)
20
15
10
5
0
0
5
10
15
20
Time (s)
C
pIPFC power (μV²/Hz)
0.25
0.20
0.15
0.10
0.05
0
0
2
4
6
8
10
12
14
16
Frequency (Hz)
Mouse 1
Mouse 2
Mouse 3
pIPFC LFP in 10% O2
1 s
0.5 mV

**Figure 3.10. Unilateral Naris occlusion decouples OB LFPs from respiration. A.** Naris occlusion impairs ascending signals from the olfactory system. Successful naris occlusion could be confirmed by the reduction of respiration-entrained oscillations in the OB, especially in the anesthetized state. Filtered signals (2-6 Hz) are overlaid on raw traces (gray). **B.** Power spectral density of OB LFPs from open and occluded sides under anesthesia. Inset, averaged peak power of the OBs from open vs occluded sides (21987 ± 4716 vs 4993 ± 1452, n = 7 mice, paired two-tailed Student's t test $t(6) = 3.662$, $p = 0.011$). Breathing rates are about 2 Hz under anesthesia.

**Figure 3.10.**

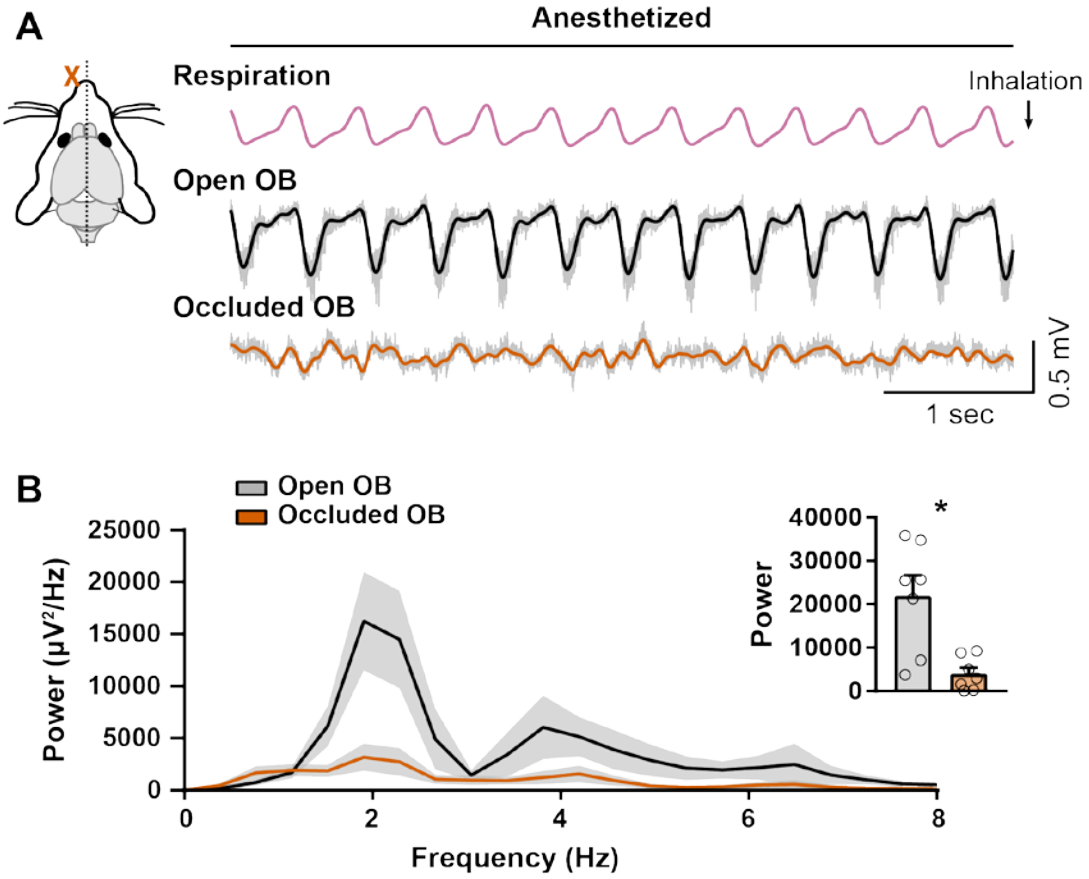
A
Anesthetized
X
Respiration
Inhalation
Open OB
Occluded OB
0.5 mV
1 sec
B
Open OB
Occluded OB
Power (μV²/Hz)
25000
20000
15000
10000
5000
0
0
2
4
6
8
Frequency (Hz)
Power
40000
30000
20000
10000
0
*

**Figure 3.11. Respiration-entrained olfactory signals contribute to the 4 Hz rhythm in the plPFC. A.** Bilateral OB and plPFC recordings from a naris occluded mouse during freezing in a fear retrieval session. **B.** Spectral coherence between simultaneously recorded OB and plPFC LFP signals during freezing periods on the open vs occluded sides (displayed as mean ± SEM, n = 7 mice). Inset, averaged peak coherence between OB and plPFC LFPs for open and closed sides (0.80 ± 0.06 to 0.58 ± 0.07, n = 7, paired two-tailed Student's *t* test $t(6) = 3.211$, $p = 0.018$. The average peak coherence between plPFC and shuffled OB signals from the occluded side is 0.42 indicated by the thick dashed line. Thin dashed lines represent the standard error. **C.** The occluded side shows a decrease in the OB-plPFC cross-correlation compared to the open side during freezing (0.69 ± 0.08 open vs 0.40 ± 0.08 occluded, n = 7, paired two-tailed Student's *t* test $t(6) = 3.35$, $p = 0.015$).

**Figure 3.11.**

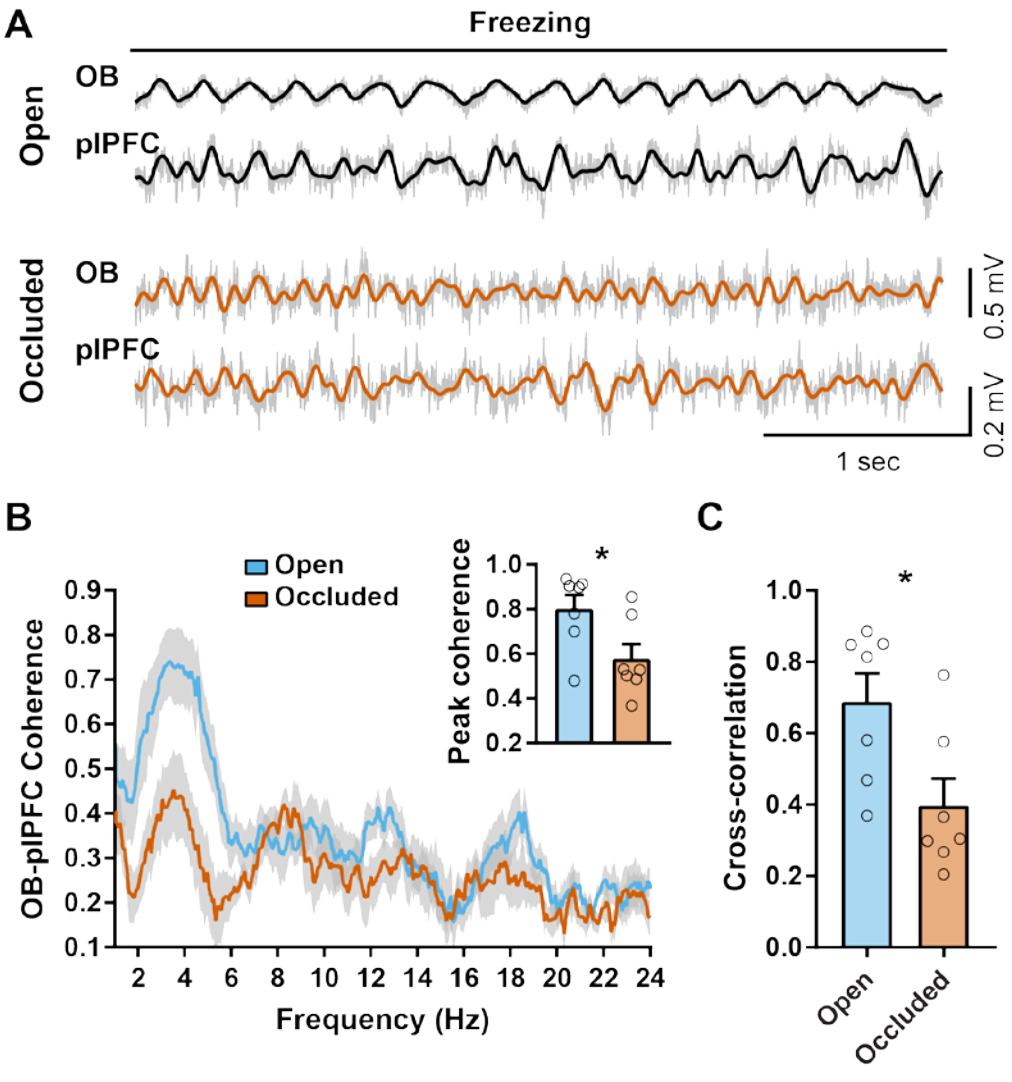
A
Freezing
Open
OB
plPFC
Occluded
OB
plPFC
0.5 mV
0.2 mV
1 sec
B
Open
Occluded
OB-plPFC Coherence
Frequency (Hz)
Peak coherence
*
C
Cross-correlation
*
Open
Occluded

**Figure 3.12. Tracing olfactory input to the plPFC. A.** The prelimbic PFC (PL) receives direct inputs from the ipsilateral anterior olfactory nucleus (AON) and ventral tania tecta (vTT). Focal injection of 0.5 µl CAV2-cre (13 x $10^{12}$ gc/ml) into the PL in $Rosa^{tdTomatof/f}$ reporter mice leads to labeled cell bodies in the AON and vTT, two regions that receive direct input from the OB. IL infralimbic cortex, CTX cortex, PIR piriform cortex, LOT lateral olfactory tract, dTT dorsal taenia tecta, vTT ventral taenia tecta. Scale bar: 750 µm, left and 250 µm, right panel and bottom right panel. **Ai** show an expanded view of the region outlined in A and **Aii** shows the same region from a more section anterior to the section shown in Ai. **B**. Focal injection of Cre-dependent ChR2-EYFP virus directed to the AON in Vglut-1-Cre mice results in labeled fibers in the prelimbic (PL, **Bi)** and infralimbic (IL, **Bii**) PFC. Note that there is essentially no viral infection in the main olfactory bulb (MOB) and projections from the AON to the PFC are found only on the ipsilateral side. Scale bar: 200 µm, center panel and 30 µm, right panels.

**Figure 3.12.**

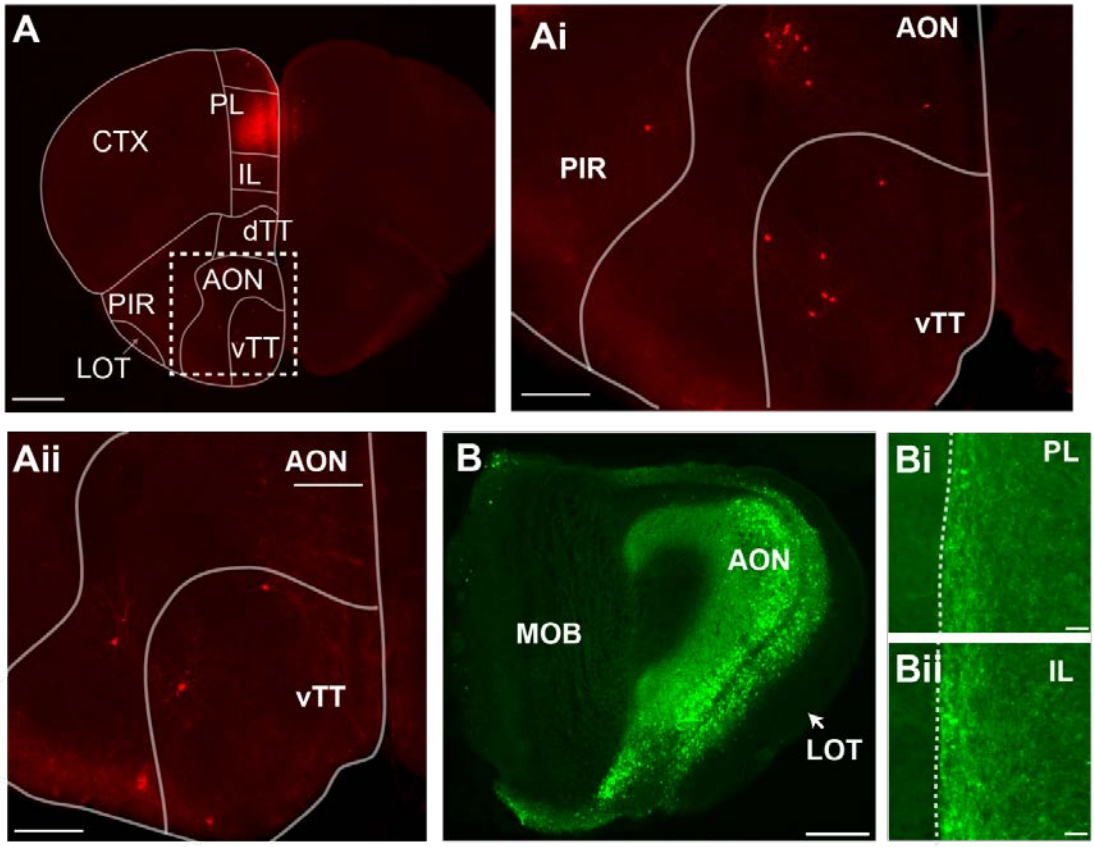
A
CTX
PL
IL
dTT
AON
PIR
vTT
LOT
Ai
AON
PIR
vTT
Aii
AON
vTT
B
AON
MOB
LOT
Bi
PL
Bii
IL

**Figure 3.13. Functional connectivity between AON projections and the plPFC. A.** A schematic of the recording strategy. Top, focal injections of ChR2-EYFP are delivered to the anterior olfactory nucleus of VGluT1-Cre mice to label AON-plPFC excitatory projections (as in Figure 3.8, these projections target the superficial layers of the ipsilateral PL and IL prefrontal cortex). Since these mice express tdTomato under control of the VGluT1 promotor, pyramidal cells can be targeted for *in vitro* patch-clamp recordings in coronal brain slices that contain the PL and IL prefrontal cortex (bottom). **B.** Light evoked excitatory currents in VGlutT1$^{+}$ cells in the prelimbic cortex. In the presence of CNQX these excitatory currents are abolished.

**Figure 3.13.**

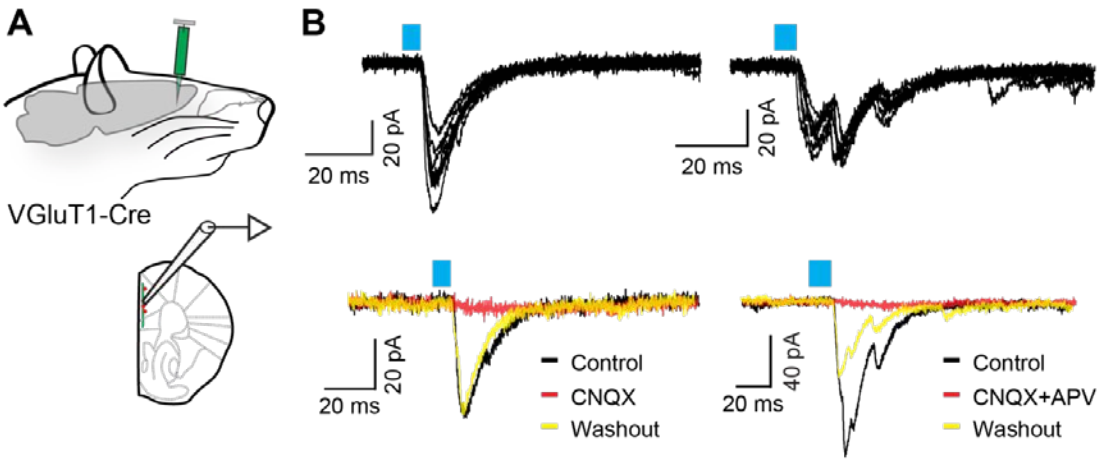
A
VGluT1-Cre
B
20 pA
20 ms
20 pA
20 ms
20 pA
20 ms
Control
CNQX
Washout
40 pA
20 ms
Control
CNQX+APV
Washout

**Figure 3.14. Optogenetic stimulation of olfactory sensory neurons entrains rhythmic activity in the OB and plPFC. A.** An optic fiber was implanted in the nose of OMP-ChR2 mice to stimulate OSNs. The example shows stimulation at 13 Hz (15 mW, 20 ms), which is distinct from endogenous respiration rhythms. Simultaneous LFP recordings from the OB and the plPFC show optical stimuatlion-entrained neural activity. Filtered signals (2-20 Hz) are overlaid on raw traces (gray). Blue bars mark laser (473 nm) pulses delivered to the nasal epithelium. **B.** The power spectral density (mean ± SEM, n = 3 mice) of plPFC LFPs shows increased power at 13 Hz, the optogenetic stimulation frequency (blue). The black line shows data from control mice (n = 3, $OMP^{cre/WT}$ mice without ChR2) that underwent the same procedure as OMP-ChR2 mice.

**Figure 3.14.**

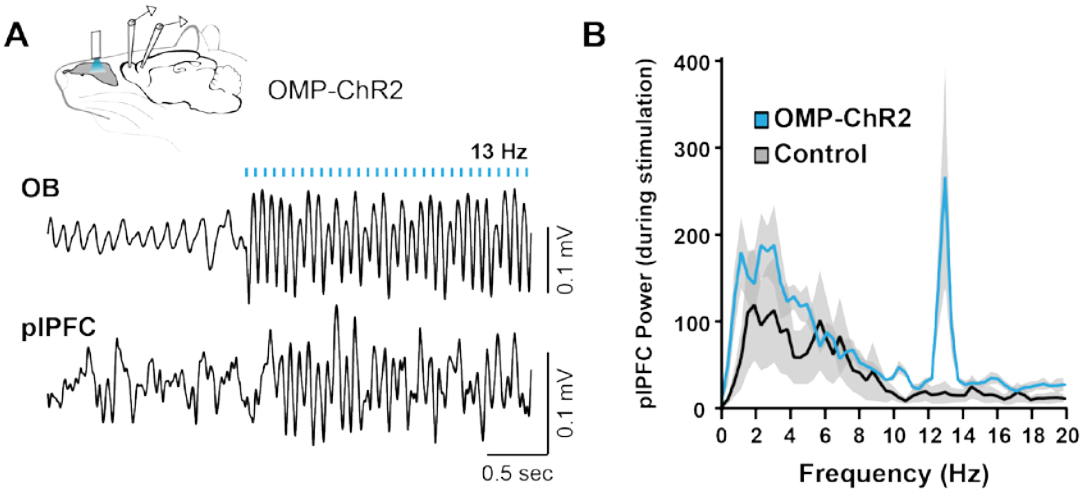
A
OMP-ChR2
13 Hz
OB
0.1 mV
pIPFC
0.1 mV
0.5 sec
B
OMP-ChR2
Control
pIPFC Power (during stimulation)
400
300
200
100
0
0 2 4 6 8 10 12 14 16 18 20
Frequency (Hz)

**Figure 3.15. Disruption of olfactory inputs via methimazole decouples olfactory bulb LPFs from respiration in awake and anesthetized states but does not alter baseline breathing activity. A.** Sections of olfactory epithelia from six-week old mice. Arrow lines denote the thickness of the olfactory epithelium. Dashed lines mark the basement membrane that separates the olfactory epithelium from the lamina propria. Asterisks mark $OMP^+$ axonal bundles that remain following the ablation of the OSN cell bodies. Scale bar, 50 μm. **B.** Thermocouple and OB LFP recordings from a single mouse 5 days following methimazole injection. The OB oscillations no longer faithfully follow respiration, in contrast to control conditions (c.f. Figure 3.2). **C.** Average peak coherence between respiratory signals and OB LFPs (one-way ANOVA $F(3,17) = 35.1$, Tukey post hoc, awake control vs methimazole, $p < 0.001$; anesthetized control vs methimazole, $p < 0.001$). The average peak coherence between respiration and shuffled OB signals is 0.55 indicated by the thick dashed line (the thin dashed lines indicate the standard error). **D.** The percent of power in 5 frequency bands of respiratory signals recorded from freely moving mice (n = 4) is unchanged following methimazole treatment, two-way ANOVA with repeated measures $F(1,3) = 0.6$, $p = 0.495$ for pre vs post methimazole condition. Respiration was monitored for 2 hours in home cages before and after methimazole injection. Signals were analyzed in 10 sec epochs. **E.** Left, Representative thermocoulple signal from a methimazole treated mouse during conditioned freezing behavior. Breathing is at ~4 Hz. Right, breathing frequency during freezing in methimazole treated mice (n = 3 mice, 9 freezing periods). Average respiration rate is 0.34 ± 0.27 which is not different from 4 (One sample *t* test $t(8) = 2.10$, $p = 0.07$).

**Figure 3.15.**

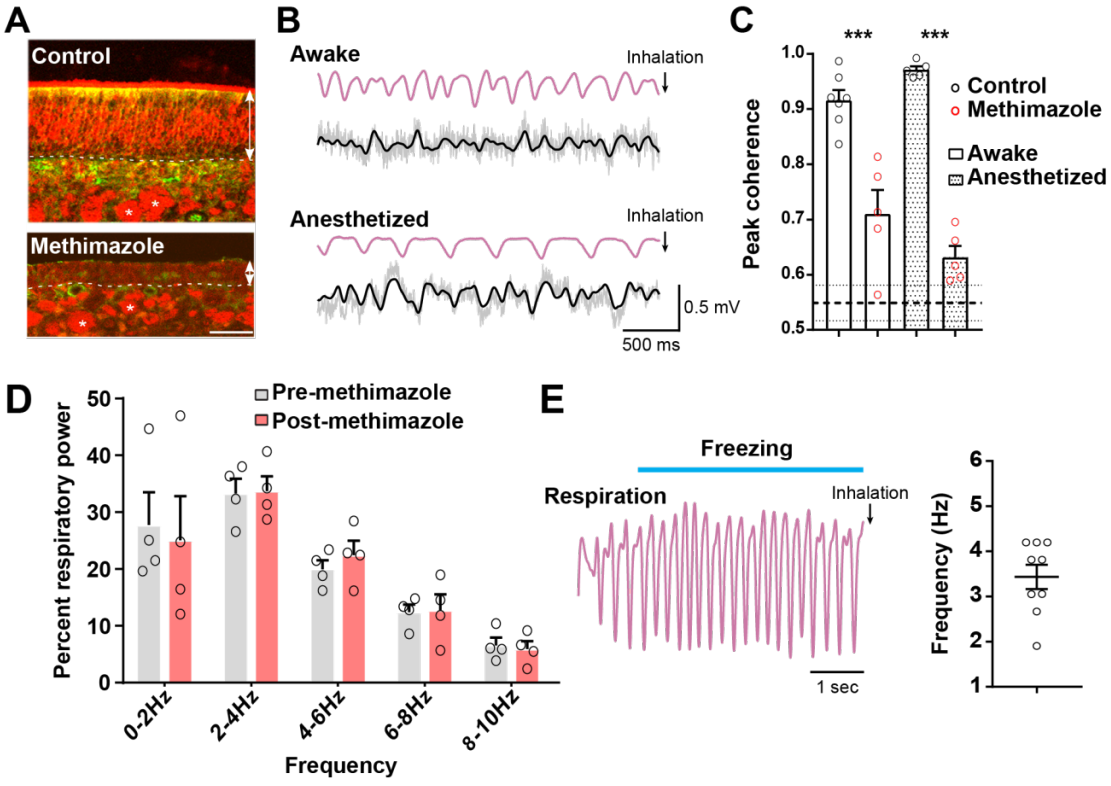
A
Control
Methimazole
B
Awake
Inhalation
Anesthetized
Inhalation
0.5 mV
500 ms
C
***
***
Peak coherence
1.0
0.9
0.8
0.7
0.6
0.5
Control
Methimazole
Awake
Anesthetized
D
Pre-methimazole
Post-methimazole
Percent respiratory power
50
40
30
20
10
0
0-2Hz
2-4Hz
4-6Hz
6-8Hz
8-10Hz
Frequency
E
Freezing
Respiration
Inhalation
1 sec
Frequency (Hz)
6
5
4
3
2
1

**Figure 3.16. Disruption of olfactory inputs via methimazole decouples olfactory bulb LPFs from respiration during conditioned freezing. A.** Example OB and plPFC LFPs during a freezing epoch in a methimazole-treated mouse. Filtered signals (2-6 Hz) are overlaid on raw traces (gray). **B.** Spectral coherence between simultaneously recorded OB and plPFC LFPs during non-freezing (black) and freezing (blue) periods (mean ± SEM, n = 9 mice). Inset, averaged peak coherence for non-freezing and freezing periods (0.54 ± 0.06 to 0.58 ± 0.04, n = 9, paired two-tailed Student's *t* test $t(8) = 0.552$, $p = 0.60$). **C.** Example cross and auto correlations between filtered (2-6 Hz) OB and plPFC signals recorded during freezing in a methimazole treated mouse. The OB-plPFC cross correlation from Figure 3.6 (control) is shown in gray for comparison **D.** Maximum OB-plPFC cross-correlation values during non-freezing and freezing periods (0.33 ± 0.05 to 0.40 ± 0.03, n = 9, paired two-tailed Student's *t* test $t(8) = 1.08$, $p = 0.31$. **E.** The phase locking value (between the OB and plPFC) for each was not different from freezing to non-freezing periods (0.33 ± 0.04 to 0.37 ± 0.02, n = 9, paired two-tailed Student's *t* test $t(8) = 0.35$, $p = 0.47$). **F.** Circular distribution of phase differences between OB and plPFC 2-6 Hz signals during freezing (Rayleigh test for circular non uniformity z = 2.08, p = 0.125). Data from methimazole treated animals are overlaid on the distribution from control animals (in gray, as in **Figure 3.6**).

**Figure 3.16.**

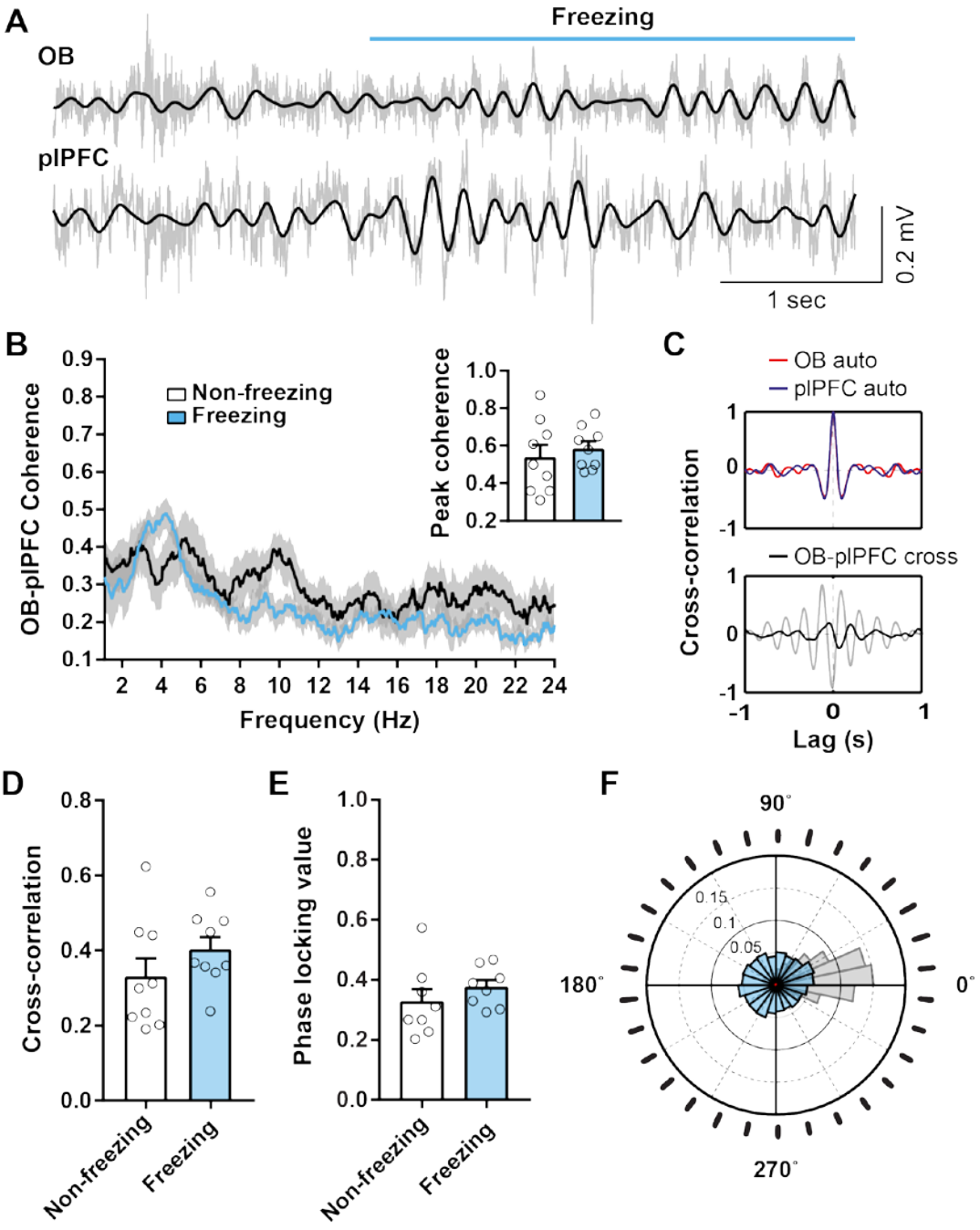
A
Freezing
OB
pIPFC
0.2 mV
1 sec
B
Non-freezing
Freezing
OB-pIPFC Coherence
Frequency (Hz)
Peak coherence
C
OB auto
pIPFC auto
OB-pIPFC cross
Cross-correlation
Lag (s)
D
Cross-correlation
Non-freezing
Freezing
E
Phase locking value
Non-freezing
Freezing
F
90°
180°
0°
270°
0.15
0.1
0.05

**Figure 3.17. Disruption of olfactory inputs via methimazole treatment prolongs freezing periods. A.** Baseline (pre-tone onset) freezing time is not significantly different among control (n = 8), unilaterally naris occluded (n = 7), and methimazole treated (n = 9) groups (one-way ANOVA $F(2,21) = 1.28$, $p = 0.30$). **B.** Freezing time during the retrieval session (post-tone) is significantly longer in methimazole treated mice compared to control and naris-occluded animals (one-way ANOVA $F(2,21) = 15.61$, Tukey post hoc, control vs methimazole $p < 0.001$, naris occluded vs methimazole $p < 0.001$). **C.** Cumulative frequency distributions show methimazole treated animals have increased frequency of longer freezing periods compared to control or naris-occluded mice ($p < 0.001$, two-sample Kolmogorov-Smirnov test).

**Figure 3.17.**

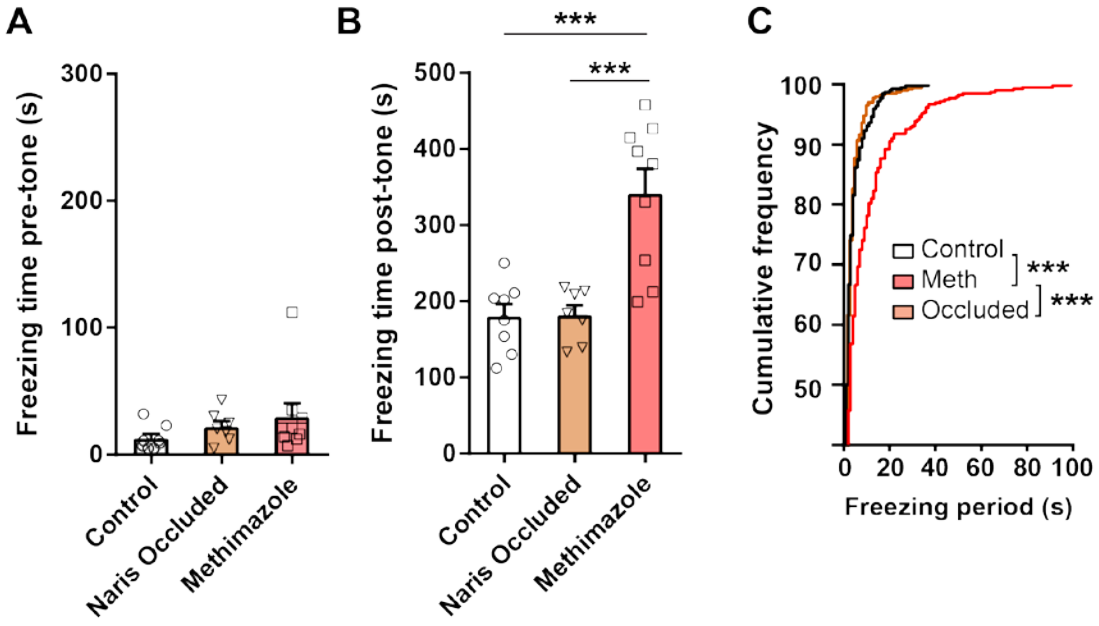
A
Freezing time pre-tone (s)
300
200
100
0
Control
Naris Occluded
Methimazole
B
***
***
Freezing time post-tone (s)
500
400
300
200
100
0
Control
Naris Occluded
Methimazole
C
Cumulative frequency
100
90
80
70
60
50
Control
Meth
Occluded
***
***
0
20
40
60
80
100
Freezing period (s)

**Figure 3.18. Disruption of olfactory inputs via inactivation of OB circuits prolongs freezing periods. A.** Example traces of OB LFPs, 2-6 Hz filtered traces are overlaid on raw traces (gray) before (pre-TTX) and 30 min after intrabulbar injection of TTX (post-TTX). The amplitude of low-frequency, respiration-related oscillatory activity is decreased. **B.** Baseline (pre-tone onset) freezing time is significantly longer in TTX infused mice (53.71 ± 13.13 s, n = 7) compared to saline treated control mice (12.43 ± 2.27 s, n = 7; unpaired two tailed Student's *t* test $t(12) = 3.10$, $p = 0.009$). **Ci.** Freezing time is significantly longer in TTX infused mice (410.60 ± 71.39 s) compared to saline treated mice (186.60 ± 45.59 s, n = 7; unpaired two tailed Student's *t* test $t(12) = 2.65$, $p = 0.021$. **Cii.** Results were similar if automated software (AnyMaze) was used to quantify post-tone freezing time (479.8 ± 43.56 s vs 257.5 s, unpaired two tailed Student's *t* test $t(12) = 2.80$, $p = 0.016$). **D.** Cumulative frequency distributions show TTX infused animals have an increased frequency of longer freezing periods compared to saline infused mice ($p = 0.01$ in two-sample Kolmogorov-Smirnov test). E. Total distance traveled prior to tone onset is not different in saline (6.40 ± 1.18 m) and TTX infused mice (6.16 ± 1.51 m; unpaired Student's *t* test $t(12) = 0.127$, $p = 0.90$).

**Figure 3.18.**

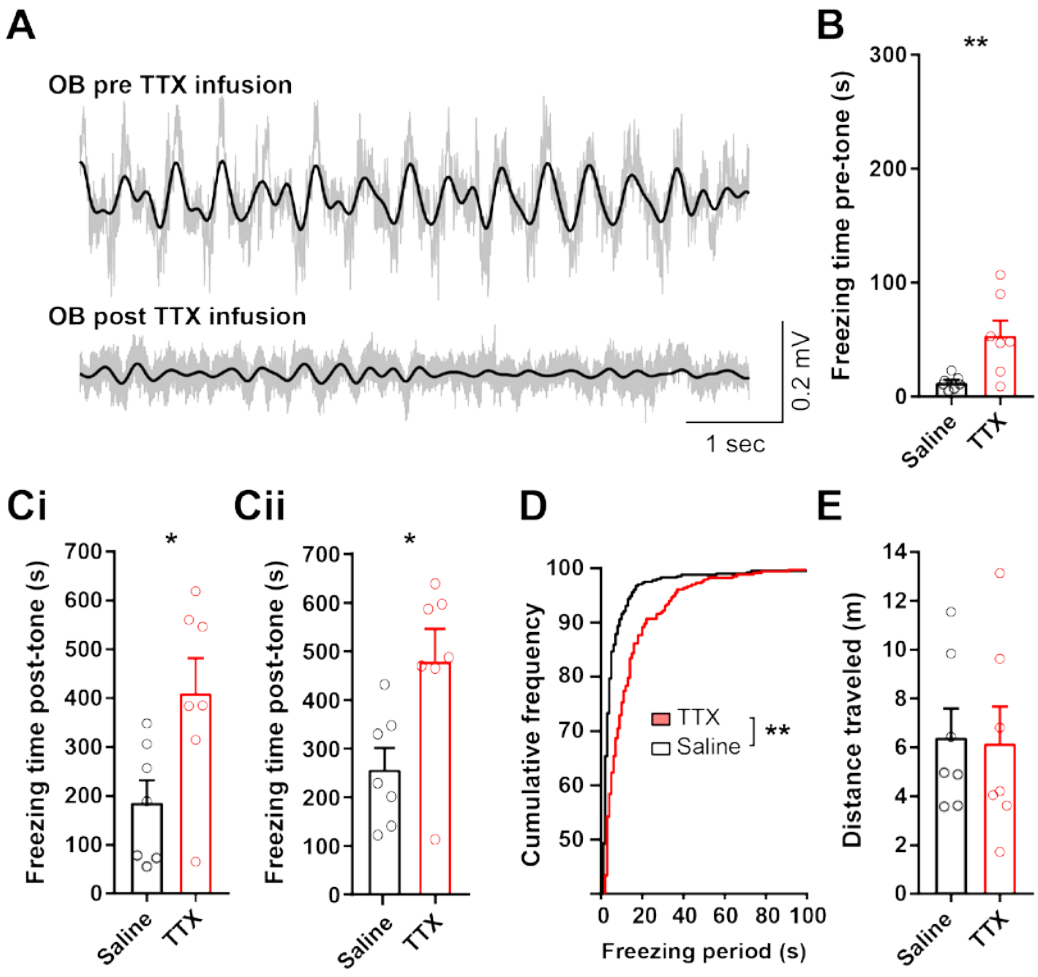
A
OB pre TTX infusion
OB post TTX infusion
0.2 mV
1 sec
B
**
Freezing time pre-tone (s)
300
200
100
0
Saline
TTX
Ci
*
Freezing time post-tone (s)
700
600
500
400
300
200
100
0
Saline
TTX
Cii
*
Freezing time post-tone (s)
700
600
500
400
300
200
100
0
Saline
TTX
D
Cumulative frequency
100
90
80
70
60
50
TTX
Saline
**
0
20
40
60
80
100
Freezing period (s)
E
Distance traveled (m)
14
12
10
8
6
4
2
0
Saline
TTX

## References


Angyan L, Szirmai I (1967) Recording of respiration with thermocouple in freely moving cats. Acta Physiol Acad Sci Hung 31:73-76.

Bergstrom U, Giovanetti A, Piras E, Brittebo EB (2003) Methimazole-induced damage in the olfactory mucosa: effects on ultrastructure and glutathione levels. Toxicol Pathol 31:379-387.

Bleymehl K, Perez-Gomez A, Omura M, Moreno-Perez A, Macias D, Bai Z, Johnson RS, Leinders-Zufall T, Zufall F, Mombaerts P (2016) A Sensor for Low Environmental Oxygen in the Mouse Main Olfactory Epithelium. Neuron 92:1196-1203.

Brittebo EB (1995) Metabolism-dependent toxicity of methimazole in the olfactory nasal mucosa. Pharmacol Toxicol 76:76-79.

Chan T, Kyere K, Davis BR, Shemyakin A, Kabitzke PA, Shair HN, Barr GA, Wiedenmayer CP (2011) The role of the medial prefrontal cortex in innate fear regulation in infants, juveniles, and adolescents. The Journal of neuroscience : the official journal of the Society for Neuroscience 31:4991-4999.

Chen YM, Liu XF, Jia XL, Zong W, Ma YY, Xu FQ, Wang JH (2014) Anxiety- and depressive-like behaviors in olfactory deficient Cnga2 knockout mice. Behav Brain Res 275:219-224.

Costanzo RM (2005) Regeneration and rewiring the olfactory bulb. Chem Senses 30 Suppl 1:i133-134.

Courtiol E, Amat C, Thevenet M, Messaoudi B, Garcia S, Buonviso N (2011) Reshaping of bulbar odor response by nasal flow rate in the rat. PLoS One 6:e16445.

De Saint Jan D, Hirnet D, Westbrook GL, Charpak S (2009) External tufted cells drive the output of olfactory bulb glomeruli. The Journal of neuroscience : the official journal of the Society for Neuroscience 29:2043-2052.

DeNardo LA, Berns DS, DeLoach K, Luo L (2015) Connectivity of mouse somatosensory and prefrontal cortex examined with trans-synaptic tracing. Nat Neurosci 18:1687-1697.

Fein G, Raz J, Brown FF, Merrin EL (1988) Common reference coherence data are confounded by power and phase effects. Electroencephalogr Clin Neurophysiol 69:581-584.

Freeman WJ (1972) Depth recording of averaged evoked potential of olfactory bulb. J Neurophysiol 35:780-796.

Frysztak RJ, Neafsey EJ (1991) The effect of medial frontal cortex lesions on respiration, "freezing," and ultrasonic vocalizations during conditioned emotional responses in rats. Cereb Cortex 1:418-425.

Fukunaga I, Berning M, Kollo M, Schmaltz A, Schaefer AT (2012) Two distinct channels of olfactory bulb output. Neuron 75:320-329.

Glinka ME, Samuels BA, Diodato A, Teillon J, Mei DF, Shykind BM, Hen R, Fleischmann A (2012) Olfactory Deficits Cause Anxiety-Like Behaviors in Mice. J Neurosci 32:6718-6725.

Gore BB, Soden ME, Zweifel LS (2013) Manipulating gene expression in projection-specific neuronal populations using combinatorial viral approaches. Curr Protoc Neurosci 65:4 35 31-20.

Gray CM, Skinner JE (1988) Centrifugal regulation of neuronal activity in the olfactory bulb of the waking rabbit as revealed by reversible cryogenic blockade. Exp Brain Res 69:378-386.

Haberly LB, Price JL (1977) The axonal projection patterns of the mitral and tufted cells of the olfactory bulb in the rat. Brain Res 129:152-157.

Hendriksen H, Korte SM, Olivier B, Oosting RS (2015) The olfactory bulbectomy model in mice and rat: one story or two tails? Eur J Pharmacol 753:105-113.

Hoover WB, Vertes RP (2007) Anatomical analysis of afferent projections to the medial prefrontal cortex in the rat. Brain Struct Funct 212:149-179.

Igarashi KM, Ieki N, An M, Yamaguchi Y, Nagayama S, Kobayakawa K, Kobayakawa R, Tanifuji M, Sakano H, Chen WR, Mori K (2012) Parallel mitral and tufted cell pathways route distinct odor information to different targets in the olfactory cortex. The Journal of neuroscience : the official journal of the Society for Neuroscience 32:7970-7985.

Illig KR, Eudy JD (2009) Contralateral projections of the rat anterior olfactory nucleus. J Comp Neurol 512:115-123.

Ito J, Roy S, Liu Y, Cao Y, Fletcher M, Lu L, Boughter JD, Grun S, Heck DH (2014) Whisker barrel cortex delta oscillations and gamma power in the awake mouse are linked to respiration. Nat Commun 5.

Karalis N, Sirota A (2018) Breathing coordinates limbic network dynamics underlying memory consolidation. bioRxiv (Preprint).

Karalis N, Dejean C, Chaudun F, Khoder S, Rozeske RR, Wurtz H, Bagur S, Benchenane K, Sirota A, Courtin J, Herry C (2016) 4-Hz oscillations synchronize prefrontal-amygdala circuits during fear behavior. Nat Neurosci 19:605-612.

Kepecs A, Uchida N, Mainen ZF (2007) Rapid and precise control of sniffing during olfactory discrimination in rats. J Neurophysiol 98:205-213.

King C, Hall WG (1990) Developmental-Change in Unilateral Olfactory Habituation Is Mediated by Anterior Commissure Maturation. Behav Neurosci 104:796-807.

Kiselycznyk CL, Zhang S, Linster C (2006) Role of centrifugal projections to the olfactory bulb in olfactory processing. Learn Mem 13:575-579.

Kremer EJ, Boutin S, Chillon M, Danos O (2000) Canine adenovirus vectors: an alternative for adenovirus-mediated gene transfer. J Virol 74:505-512.

Lachaux JP, Rodriguez E, Martinerie J, Varela FJ (1999) Measuring phase synchrony in brain signals. Hum Brain Mapp 8:194-208.

Lojowska M, Gladwin TE, Hermans EJ, Roelofs K (2015) Freezing Promotes Perception of Coarse Visual Features. J Exp Psychol Gen 144:1080-1088.

Matsutani S, Yamamoto N (2008) Centrifugal innervation of the mammalian olfactory bulb. Anat Sci Int 83:218-227.

McAfee SS, Ogg MC, Ross JM, Liu Y, Fletcher ML, Heck DH (2016) Minimally invasive highly precise monitoring of respiratory rhythm in the mouse using an epithelial temperature probe. J Neurosci Meth 263:89-94.

Miller EK, Cohen JD (2001) An integrative theory of prefrontal cortex function. Annu Rev Neurosci 24:167-202.

Nagayama S, Takahashi YK, Yoshihara Y, Mori K (2004) Mitral and tufted cells differ in the decoding manner of odor maps in the rat olfactory bulb. J Neurophysiol 91:2532-2540.

Negus VE (1927) The Function of the Epiglottis. J Anat 62:1-8.

Ongur D, Price JL (2000) The organization of networks within the orbital and medial prefrontal cortex of rats, monkeys and humans. Cereb Cortex 10:206-219.

Parabucki A, Lampl I (2017) Volume Conduction Coupling of Whisker-Evoked Cortical LFP in the Mouse Olfactory Bulb. Cell Rep 21:919-925.

Rodrigues SM, Schafe GE, LeDoux JE (2004) Molecular mechanisms underlying emotional learning and memory in the lateral amygdala. Neuron 44:75-91.

Rojas-Libano D, Frederick DE, Egana JI, Kay LM (2014) The olfactory bulb theta rhythm follows all frequencies of diaphragmatic respiration in the freely behaving rat. Front Behav Neurosci 8:214.

Scott JW (1981) Electrophysiological identification of mitral and tufted cells and distributions of their axons in olfactory system of the rat. J Neurophysiol 46:918-931.

Seidenbecher T, Laxmi TR, Stork O, Pape HC (2003) Amygdalar and hippocampal theta rhythm synchronization during fear memory retrieval. Science 301:846-850.

Shipley MT, Adamek GD (1984) The connections of the mouse olfactory bulb: a study using orthograde and retrograde transport of wheat germ agglutinin conjugated to horseradish peroxidase. Brain Res Bull 12:669-688.

Song C, Leonard BE (2005) The olfactory bulbectomised rat as a model of depression. Neurosci Biobehav Rev 29:627-647.

Stumpf C, Petsche H, Gogolak G (1962) The significance of the rabbit's septum as a relay station between the midbrain and the hippocampus. II. The differential influence of drugs upon both the septal cell firing pattern and the hippocampus theta activity. Electroencephalogr Clin Neurophysiol 14:212-219.

Suzukawa K, Kondo K, Kanaya K, Sakamoto T, Watanabe K, Ushio M, Kaga K, Yamasoba T (2011) Age-related changes of the regeneration mode in the mouse peripheral olfactory system following olfactotoxic drug methimazole-induced damage. J Comp Neurol 519:2154-2174.

Uchida N, Mainen ZF (2003) Speed and accuracy of olfactory discrimination in the rat. Nat Neurosci 6:1224-1229.

Wesson DW (2013) Sniffing behavior communicates social hierarchy. Curr Biol 23:575-580.

Wesson DW, Donahou TN, Johnson MO, Wachowiak M (2008) Sniffing behavior of mice during performance in odor-guided tasks. Chem Senses 33:581-596.

Whitmore NW, Lin SC (2016) Unmasking local activity within local field potentials (LFPs) by removing distal electrical signals using independent component analysis. Neuroimage 132:79-92.

Woeber KA (2002) Methimazole-induced hepatotoxicity. Endocr Pract 8:222-224.

Xie F, Zhou X, Genter MB, Behr M, Gu J, Ding X (2011) The tissue-specific toxicity of methimazole in the mouse olfactory mucosa is partly mediated through target-tissue metabolic activation by CYP2A5. Drug Metab Dispos 39:947-951.

Yanovsky Y, Ciatipis M, Draguhn A, Tort AB, Brankack J (2014) Slow oscillations in the mouse hippocampus entrained by nasal respiration. The Journal of neuroscience : the official journal of the Society for Neuroscience 34:5949-5964.

Zueger M, Urani A, Chourbaji S, Zacher C, Roche M, Harkin A, Gass P (2005) Olfactory bulbectomy in mice induces alterations in exploratory behavior. Neurosci Lett 374:142-146.

# CHAPTER 4: DISCUSSION

## Nasal breathing, brain rhythms, and fear behavior

Most cognitive processes have been linked to at least one traditionally described oscillatory regime. But despite about 90 years of research on brain rhythms beginning with Hans Berger's discovery of the human EEG there remain differing opinions regarding their functional role. On one hand, some argue that despite the widespread presence of neural rhythms, oscillatory activity is epiphenomenal. On the other hand, many believe oscillatory activity to be fundamental to the brain: no oscillations, no function. Analogously the individual members of an orchestra can play all the right notes, but the conductor of the orchestra (rhythm) is necessary to make a piece of music sound beautiful. A major difficulty in testing the function of oscillations is that these rhythms are an emergent property of reciprocally connected excitatory and inhibitory circuits. Thus, it is difficult to interfere cleanly with oscillations *per se* without disrupting the underlying processes at the same time. The appropriate experiments would involve specifically and non-invasively abolishing endogenous electric field activity in awake-behaving animals which is currently technically challenging.

However, it is clear that ongoing neuronal activity is defined by the combination of anatomical interconnectivity, synaptic activity, and spatial-temporal electric fields. That is to say, electric fields directly affect the neurons in the networks that give rise to them even though the fields themselves may not be strong enough to trigger or suppress action potentials themselves (Francis et al., 2003; Radman et al., 2007; Frohlich and McCormick, 2010).

One approach to causally link brain rhythms and neural computations is to induce exogenous oscillations in a system. For example, in humans, transcranial magnetic stimulation (TMS) or transcranially applied currents can entrain rhythmic brain oscillation patterns at the input frequency (Ozen et al., 2010; Thut et al., 2011). Patterns of stimulation at 30 Hz over the frontal eye field caused human subjects to better detect near-threshold stimuli (i.e. improved their perceptual sensitivity) suggesting that visual processing is enhanced by an extrinsic source of neural synchronization at a specific frequency (Chanes et al., 2013). Likewise, slow (less than 1 Hz) transracially applied currents that mimic slow oscillations in frontal cortex during non-REM sleep enhance the retention (or slows decay of memory) of items in a declarative memory task (Marshall et al., 2006).

In rodent models, optogenetic control over specific neuronal populations can induce field oscillations (an approach we took in **Chapter 2** using synchronous OSN activation). For example, in the neocortex, synchronous optogenetic activation of fast-spiking, parvalbumin-expressing interneurons generates local gamma oscillations (Cardin et al., 2009). The timing of sensory input (whisker deflections) relative to the artificially induced gamma phase determined how many pyramidal neuron spikes were evoked by the stimuli. So, sensory input that arrives at a specific phase of the ongoing gamma frequency field activity is more likely to activate barrel cortex neurons and their downstream targets. Furthermore, using this strategy to induce gamma oscillations causes less salient sensory stimuli to be better detected while simultaneously impairing the detection of more salient ones (Siegle et al., 2014). Although these are not natural

oscillations that arise due to network properties, these results suggest that rhythms can influence neuronal gain and sensory processing.

In our experiments we investigated the 4-Hz oscillation in the prefrontal cortex expressed during freezing in order to explore the role of breathing-related signals in emotional processing (**Chapter 3**). Recent studies suggest respiration-related signals in the brain are widespread and that there are at least two distinct patterns of cortical activity related to respiration: *1*) Low frequency oscillations that explicitly follow the breathing rhythm and *2*) modulation of locally generated gamma activity locked to breathing. Thus, one hypothesis is that respiration-entrained oscillations aid long-range communication between functional networks in the brain and temporally organize local activity via their influence on gamma activity. We focused on low frequency activity correlated with breathing and did not explicitly test if gamma in the plPFC is modulated by the 4 Hz respiration-related rhythm. However, we know that in other contexts gamma (75 Hz) amplitude in the barrel cortex is modulated by the phase of low-frequency breathing oscillations (Ito et al., 2014). Likewise, in the prefrontal cortex, the breathing rhythm phase modulates gamma at 80-100 Hz (Biskamp et al., 2017). In both cortices gamma amplitude is highest at the peak of the lower frequency cycle. Similar theta-gamma interactions emerge during working memory tasks but since respiration was not measured it is unclear if the 'theta' signal modulating gamma was respiration-related (Li et al., 2012b).

Thus, like other characterized rhythms that provide temporal windows of reduced and enhanced excitability, breathing-related oscillations could group or 'chunk' neural activity into discrete cell assemblies or sequences of assemblies (Masquelier et al., 2009;

Buzsaki, 2010). Downstream integrators will 'see' neural events only if spikes occur within the appropriate time-integrating window as defined by the low frequency oscillation. Thus, one potential working model is one in which respiration-related olfactory inputs help to entrain a low-frequency rhythm that may work in this manner to bind neural activity in key portions of the fear circuit including the basolateral amygdala, prefrontal cortex, and hippocampus. The ultimate activation of the appropriate cell assemblies that produce fear behavior likely involves the periaqueductal grey (PAG). The PAG is a midbrain structure implicated in defensive behaviors such as fight and flight responses, freezing, and physiological metrics such as blood pressure, heart rate, and vocal activity. Broadly speaking, the PAG is anatomically divided into dorsolateral (dlPAG), dorsalmedial (dmPAG), and ventralateral (vlPAG) subregions. Functionally, the dlPAG is involved in innate defensive responses to predators, the dmPAG is involved in defensive responses to conspecifics, and the vlPAG is critical for conditioned freezing responses to painful stimuli (Gross and Canteras, 2012). Accordingly, subregions of the PAG may differentially regulate breathing. In fact, electrical stimulation of the dorsal subregion induces anticipatory fight or flight responses that prepare the animal for high-intensity exercise, including decreased inspiratory and expiratory duration (Huang et al., 2000; Hayward et al., 2003; Hayward et al., 2004). In cats, stimulation of the ventrolateral PAG induces a temporary increase in respiratory frequency followed by respiratory depression (Subramanian et al., 2008).

Excitatory projections from the vlPAG gray target premotor cells in the magnocellular nucleus of the medulla that promote freezing. These vlPAG projections are typically under the control of local inhibitory microcircuits. GABAergic projections from

the central nucleus of the amygdala (CEA) target these inhibitory interneurons to disinhibit vlPAG outputs (Tovote et al., 2016). It may be the case that the PAG controls motor output and respiratory behavior and can ultimately cause breathing at 4 Hz. This rhythmic breathing signal is detected by mechanosensitive OSNs in the nasal epithelium and propagated to the olfactory bulb. Bulbar outputs could be sent to downstream areas that express respiratory rhythms including the prefrontal cortex (possibly via a tufted cell → AON/TT → PFC pathway) which synchronizes activity in the BLA during freezing behavior (Karalis et al., 2016; Karalis and Sirota, 2018). Fear-related information processed in the basolateral amygdala is relayed to the CEA which then regulates multiple fear responses mediated by the downstream PAG circuits including changes in respiration as described above (LeDoux, 2000; Isosaka et al., 2015).

This model (schematized in **Figure 1.1**) presumes the 4 Hz signal is part of a positive feedback loop that can help to sustain periods of behavioral freezing once they are initiated. One common idea is that freezing serves to put an organism into a state optimized for sensory processing (Blanchard et al., 2011; Lojowska et al., 2015). The hypothesis that remains to be tested is if the coordination of multiple brain regions via low frequency oscillations improves how sensory signals (especially those originating from the threat-detecting olfactory system) influence key brain regions. This may constitute a mechanism for improving stimuli detection and identification.

There are a few points that call this interpretation into question. For one, in this framework it remains to be determined how freezing periods are terminated once they are initiated. It is worth noting that AON outputs also target the superficial layers of ilPFC (**Figure 3.12**) a subregion of the medial PFC that functionally opposes the plPFC.

Without the ilPFC conditioned freezing behavior is aberrantly increased even with repeated fear extinction training. This is believed to be due to IL projections to the BLA that target inhibitory intercalated neurons in the amygdala that suppress amygdala output (Likhtik et al., 2008; Cho et al., 2013; Strobel et al., 2015). Nasal breathing related oscillations that reach the PL vs the IL may have different effects on initiating and terminating freezing, although this remains to be experimentally confirmed.

Second, we point out that removing sensory input significantly reduces, but does not eliminate, oscillatory activity in the 2-6 Hz range during freezing. Similarly, there is often residual coupling between breathing and respiration related neural activity following bulbectomy or tracheotomy. Do redundant mechanisms support respiration-locked oscillations? Other sensory inputs including interoceptive signals from the lungs, diaphragm, or abdominal muscles involved in respiratory movement are represented in the anterior insular cortex which integrates and represents cardiorespiratory signals (Craig, 2009; Hassanpour et al., 2018). These sensory inputs reaching either somatosensory cortex or insular cortex could entrain neural activity although their contribution to respiration-related LFPs remains to be explicitly investigated.

Likewise, we cannot rule out the possibility that brainstem rhythm generators also contribute to widespread neural entrainment with breathing. The efferent projections of the pre-Bötzinger complex reach the PAG, hypothalamus, and thalamus (Yang and Feldman, 2018). There are breathing-modulated neurons in the thalamus and thus and breathing signals could reach the cortex via thalamo-cortical pathways (Chen et al., 1992). In many systems, efference motor signals are sent to sensory regions to resolve ambiguities about how motor behavior influences sensory input (Crapse and Sommer,

2008). Similarly, it may be useful for the brain to have both a motor copy and sensory copy of breathing to compare and determine if the expected action matches the actual external action. This hypothesis remains to be tested.

It is also worth considering the possibility that the 4 Hz signal observed in the prefrontal cortex is a read-out of breathing and not functionally necessary for freezing behavior. In our experiments disrupting the 4 Hz signal in the prefrontal cortex by ablating OSNs or inactivating the OB does not result in less freezing as would be predicted if the 4 Hz signal in the plPFC was positively correlated with freezing behavior. Experiments performed in parallel by Karalis and Sirota found intact (but not increased) fear memory and expression following OSN ablation using the same methimazole treatment. One reason increased freezing was not observed (as reported here) is likely that their experimental subjects underwent two fear retrieval sessions, one before and one following olfactory de-afferentation (Karalis and Sirota, 2018).

We also observe low-frequency breathing-related oscillations during freezing evoked by innately fearful stimuli, specifically 2MT presentations (**Figure 3.7**). But freezing responses to innately fearful stimuli may not involve the same prefrontal and basolateral amygdala circuits necessary for conditioned freezing. For example, the fox odor 2,4,5-trimethyl thiazoline (TMT) activates glomeruli that project to distributed regions of the cortical amygdala. If these specific amygdala projections are tagged with ChR2 and later reactivated, experimenters observe behavioral responses similar to those evoked by naturally fearful stimuli (Root et al., 2014). In fact, photoactivation of just one out of a subset of glomeruli normally activated by TMT is sufficient to induce freezing (Saito et al., 2017). These results suggest that at least some innately fearful compounds

use a labeled-line like strategy which involves direct OB outputs to the central amygdala and downstream PAG circuitry. In our experiments, we find that during PFC-independent freezing behavior there is an oscillatory phenomenon similar to that observed in plPFC during conditioned freezing behavior. This seems inconsistent with the hypothesis that the 4 Hz oscillations are causally involved in generating conditioned freezing behavior.

However, olfactory inputs, either via mechanosensitive breathing-related signals or odor-related signals, can influence fear behavior. In our methimazole experiments olfactory sensory input was impaired during the conditioning trials as well as the retrieval sessions. Comparatively, in our OB inactivation experiments the animals were normal during conditioning but were impaired during fear retrieval. Both manipulations resulted in increased levels of freezing but with different baseline levels of fear. It is unclear if these differences in baseline levels of freezing are due to differences in how intact OB circuity is or due to having normal olfactory input during conditioning and not having input during the testing. One possible interpretation is that increased freezing results from a loss of odor cues that normally guide behavior. Analogously, disrupting other sensory modalities could have a similar effect on conditioned fear behavior. Mice, in which the olfactory sense dominates, may be particularly sensitive to a general disturbance of olfactory input since hyper activation of MOE also causes a behavioral phenotype like de-activation of OSNs. Future experiments are necessary to dissociate the effects of removing odor vs breathing signals.

## Searching for inspiration

A universal feature of brains is rhythmic activity. In fact, the first neural circuits may have been those responsible for generating simple rhythmic movements (Marder and Calabrese, 1996). With increasing complexity, circuits evolved that incorporated sensors to facilitate finding food, avoiding harmful stimuli, and reproduction. These circuits also contained neural oscillators and were built on top of existing ones resulting in parallel layers of loops that influence each other at different frequencies with evolutionarily more recent layers 'on top' (Buzsaki and Freeman, 2015). These oscillators are not only involved in motor pattern generation but also cognitive processing (since they are highly correlated with sensory processing, memory, attention, decision making). Note also that the brains of early mammals where highly olfactory and dominated by olfactory structures in which respiration is inexorably linked. One evolutionary perspective is that the neocortex may have evolved under the influence of olfaction and the other neocortical sensory areas may have used olfactory areas as a blueprint and are thus similarly sensitive to oscillations in the frequency range of breathing (Fontanini and Bower, 2006).

Here, we conceptualize the breathing rhythm as a phylogenetically older oscillator that can coordinate other rhythms and that is in turn influenced oscillators. This hypothesis is borne out in the sensorimotor domain; breathing is highly correlated with other rhythmic motor features like eye movements and body turning. Studies in humans show that respiration is entrained by motor subsystems (Ebert et al., 2000) and to some extent respiration can influence voluntary movements (Rassler and Raabe, 2003). On the sensory side, the threshold for sensory signal detection in the auditory and visual modalities is lower during expiration vs inspiration (Demaree et al., 1974; Gallego et al.,

1991; Li et al., 2012a). Also, pain is perceived as less severe if experienced during expiration compared to inspiration (Iwabe et al., 2014) and pain perception can be lessened by slow, deep breathing (Miller and Perry, 1990). Might these features be the product of nested oscillators that can interact with one another? And if so, how much is due to overlap in brainstem rhythm generators vs olfactory sensory input?

Nasal breathing signals can influence field activity in human brains as well as rodents despite major differences in both olfactory anatomy and breathing patterning. This introduces an interesting perspective on meditation research and pathophysiology related to the loss of olfactory input. Nasal breathing techniques are important in meditation and eastern practice and play a role in achieving altered states of consciousness. In western culture, voluntarily paced breathing is often used without a mindfulness component to encourage relaxation and calming mental states. Many studies focus on the clinical outcomes of chronic and acute pathologies and therefore combine breathing techniques, postures, and meditation making it difficult to disentangling the effects of breathing patterns independent of other cognitive components like focused attention and mental imagery. Regardless, in studies of the neurophysiological correlates of meditation one common motif is a high degree of EEG synchronization that is fundamentally different waking EEG. This is observed in the gamma band (Lutz et al., 2004) and led to speculation that perhaps slow breathing can to some extent influence brain-wide synchronization.

In humans the loss of breathing related signals can result in cognitive deficits. There is an interesting reciprocal relationship between olfactory function and depression: patients with depression have reduced olfactory function and patients with olfactory

dysfunction have symptoms of depression that positively correlate with the severity of olfactory impairment. We do not know to what extent the loss of rhythmic breathing signals from the olfactory system contributes (as compared to olfactory related signals which can cause loss of taste, etc). But there are correlations between neuropsychiatric diseases (including schizophrenia and depression) and measurable alterations in specific oscillatory bands. It will be necessary to further dissect out the neural mechanisms that underlie the mental and behavioral benefits of nasal breathing and determine the role of neural entrainment to the respiratory rhythm.

## Methods

### *Animals*

Wild-type mice C57BL6/J were purchased from the Jackson Laboratory (stock No: 000664). OMP-ChR2 ($OMP^{cre/WT}$-$Rosa^{ChR2f/f}$) mice were obtained by crossing OMP-cre mice (the coding region and part of the 3' upstream translating region replaced by that of Cre; Jackson stock No: 006668) with Rosa26-CAG-LSL-ChR2(H134R)-EYFP-WPRE mice (or Ai32 line, Jackson stock No. 024109). From this cross we used OMP-cre heterozygous mice since $OMP^{cre/cre}$ knockout animals have OSNs with slowed odorant response kinetics (Lee et al., 2011). $OMP^{WT/WT}$ littermates were used as controls in optogenetic stimulation experiments. $Rosa^{tdTomatof/f}$ mice (Rosa26-CAG-LSL-tdTomato-WPRE or Ai9 line, Jackson stock No: 007905) were used as a reporter line in retrograde tracing experiments. *Vglut1-Cre* mice (Vglut1-IRES2-Cre-D; Jackson stock No: 023527)

were used in anterograde tracing experiments along with ROSA26-AP (R26iAP, Jackson stock No: 009253) in alkaline phosphatase staining experiments.

All mice were kept on a 12 hour light/12 hour dark cycle and provided with food *ad libitum*. Mice were house individually following surgical implantation or viral infection. Behavioral and recoding procedures were carried out during the light phase of the cycle. Experiments included male and female mice between 2-6 months of age. Data were combined since no sex differences were evident. Mice were randomly allocated into control or experimental groups. All procedures were approved by the University of Pennsylvania Institutional Care and Use Committee.

***Surgery***

Surgical procedures included chronic implants of LFP electrodes and optic fibers, viral injections, and anesthetized extracellular recordings. For these procedures mice were exposed to isoflurane at 3% (vol/vol) in oxygen for anesthetic induction (flow rate 1 L/min). They were then secured in a stereotaxic system (Model 940, Kopf Instruments) and isoflurane levels were reduced to 1-2% for the remainder of the surgery. Body temperature was maintained at 37° C with a temperature control system (TC-1000, CWE). Respiratory rate and effort was monitored at regular intervals and anesthetic depth was regularly confirmed by pedal reflex (toe pinch). Eye moisture was maintained by applying sterile eye ointment (Artificial Tears, Henry Schein). Areas for electrode implantation were measured from bregma using a stereotaxic arm and standard coordinates (Paxinos and Franklin, 2004). We primarily made craniotomies over the OB (+4.3 mm AP, +1.0 mm ML, 1.5 mm DV) and plPFC (+1.8 mm AP, +0.3 mm ML, 1.0-1.4 mm DV). In some experiments we also targeted the HP (-2.0 mm AP, +1.5 mm ML,

1.5-2.0 mm DV) and BC (-1.0 mm AP, +3.5 mm ML, 1.0 mm DV). Once the skull was exposed small craniotomies were made (0.75-1.0 mm in diameter) by drilling in the appropriate location. To monitor respiration some animals also had a hole drilled in the anterior nasal bone for thermistor implantation (36 ga, PFA insulated, Omega Engineering, part No: 5TC-TT-K-36-36). Thermocouples were implanted in the nasal cavity contralateral to electrode implants when possible in order to minimize artifacts in the recordings that could be caused by the introduction of the probes. In optogenetic experiments a fiber optic cannula (400 µm core, 1 mm fiber length 0.39 NA, Thor Labs) was implanted in the hole in the nasal cavity. LFP electrodes consisted of pairs of PFA-coated tungsten wires (50.8 µm bare diameter, AM-systems part No: 795500) separated by 0.5-1.0 mm in the dorsal-ventral plane. Electrode impedance was measured using an IMP-2AMC (BAK Electronics) and ranged from 50-180 KΩ. Tungsten wires were attached to an 18-pin electrode interface board (EIB-16, Neuralynx). In this configuration each electrode lead was referenced to a low-impedance stainless steel wire implanted in the cerebellum (contralateral to LFP electrode implants). Local re-referencing took place offline following LFP recordings. A ground wire was wrapped around a skull screw implanted in the cerebellum and the implant was secured with low toxicity silicone elastomer (Kwik-Sil, WPI) and dental cement. In naris occlusion experiments LFP electrodes were implanted bilaterally and one naris was closed by touching a small vessel cauterizer (Fine Science Tools) to the external naris for > 5 seconds. The occluded side (left vs right) was counterbalanced across animals. Naris occlusion was confirmed by visual inspection and by loss of nasal-airflow entrained OB LFPs under anesthesia. Following surgical implantation mice were allowed to recover for 7 days before

recordings were made. A subset of animals received a single intraperitoneal injection of methimazole (Sigma-Aldrich, 75 mg/kg in sterile saline) four days prior to fear conditioning and/or recording sessions.

***Electrophysiological Recordings***

LFP recordings were made by connecting the EIB interface boards to an Intan RHD2000 amplifier board (Intan Technologies). Signals from each electrode were amplified and acquired between 0.1 Hz to 9 kHz, digitized at 25 kHz and stored on a PC for offline analysis. At the end of the experiments, animals were deeply anesthetized with ketamine/xylaxine (200/20 mg/kg body weight). In some cases, LFP recordings were taken from anesthetized animals. In these cases, direct measurements of chest expansion using a piezoelectric belt (Kent Scientific) wrapped around the mouse's body were taken to record respiration rate. In some mice electrolytic lesions were made in the brain by passing a small current (~1 mA for 30 seconds) between electrodes leads in order to mark recording sites. Then mice were transcardially perfused with phosphate buffered saline (PBS) and 4% paraformaldehyde and brains were dissected out. After overnight fixation, 75 um coronal sections were cut, mounted, and stained with cresyl violet to confirm recording sites. Specimens were compared with matching coronal sections from the Allen Mouse Brain Reference Atlas (Lein et al., 2007).

We also made blind extracellular recordings from the OB of OMP-ChR2 mice while stimulating OSNs in the nose. Briefly, in isoflurane anesthetized mice optic fibers were implanted in the nasal cavity as described above. A craniotomy was made in the skull over the olfactory bulb and glass micropipettes (20-50 MΩ, filled with 0.5 M sodium acetate) were slowly lowered until the tip reached the ventral mitral cell layer.

Here, large amplitude spiking events were often observed locked to the respiratory rhythm. Signals were amplified via a differential amplifier with an active headstage (DP-300, Warner Instruments) and referenced to a low resistance silver/silver chloride pellet electrode implanted in the neck muscle. Amplifier signals digitized at 25 kHz using a Digidata 1322 (Axon Instruments) and split into two channels, one bandpass filtered between 0.1-100 Hz and another filtered between 300-3000 Hz.

Light stimulation was delivered to OSNs via a 473 nm laser (SLOC Lasers, BL473T8-150FC) coupled to a patch cable. Laser intensity was adjusted to achieve an output of 15 mW at the fiber tip (continuous output, measured via PM100D, Thor Labs). Laser output was controlled via deliver of 0-5 V TTL pulses generated by an arbitrary waveform generator (Agilent 33201A).

***Behavioral experiments***

Fear conditioning was performed in a Med Associates modular test chamber. Briefly, a 5 kHz pure tone ($CS^+$, 10 s) was paired with a 1 second footshock (US, 0.5 mA) with the onset of the US coinciding with the offset of the $CS^+$. During the conditioning session mice received 4 $CS^+$-US pairings with intertrial intervals that ranged randomly between 120-180 s. After 24 h, mice were submitted to a 15 min testing session (fear retrieval) in a novel room and experimental chamber (an empty mouse cage, 7½" x 11½" x 5". Mice were connected to the recording apparatus and left in their home cage for 1 h prior to being moved to the novel context and the initiation of recordings and $CS^+$ presentations. Freezing behavior was scored manually by visual inspection of recorded webcam videos. Animals were considered to be freezing if no movement was detected for more than 1 s by an experimenter blind to condition.

In pharmacology experiments, wild type mice (male and female) had 26-gauge guide cannulas (WPI) bilaterally implanted into their OBs (the tip of the cannula lowered 1.5 mm ventral to the bulbar surface). After a recovery period of 1 week, these mice were fear conditioned and tested the following day. TTX (60 µM, Abcam) or sterile saline was injected via a 5 µL Hamilton syringe at a rate of 0.1 µL/min using an automated pump (Micro-4, WPI). Following injections of 0.5 µL TTX or 0.5 µL saline per bulb, mice were left in their home cage for 45 min before being transferred to a novel environment for the fear retrieval test. Additional mice (not included in the behavioral cohort) were implanted with bipolar electrodes that extended ~1 mm past the end of the guide cannula in order to acquire LFP signals before and after TTX infusion and confirm the disruption of low frequency, respiration-related signals. In these pharmacology experiments where animals were not tethered with via recording wires we could use automated behavioral software (ANY-maze tracking) was used to measure freezing. This was used to confirm our visually guided results as well as quantify the distance traveled during the free exploration portion of the fear retrieval test before the onset of the first tone.

To test freezing responses in low oxygen we used a special chamber that we slowly filled with nitrogen to displace ambient $O_2$. In some experiments naive mice were exposed to 2-Methyl-2-thiazoline (2MT, Sigma-Aldrich) diluted in mineral oil (1:1000).

***Neurotracing***

For retrograde tracing experiments $Rosa^{tdTomatof/f}$ mice were injected with CAV2-Cre virus at a concentration of $13x10^{12}$ GC/ml (Gore et al., 2013). Unilateral viral injections were made with a 33-gauge needle (Hamilton Company) and an Ultra Micro Pump (WPI) mounted to a stereotaxic arm. The needle was lowered through a craniotomy

in the skull into the plPFC (+1.8-2.0 mm AP, +0.3 mm ML, 1.4 mm ventral to the cortical sur5 face). For anterograde tracing experiments Vglut1-Cre mice were unilaterally injected with 0.5-0.8 ul Cre-dependent ChR2-EYFP (AAV1.EF1a.DIO-.hChR2(H134R)-eYFP.WPRE.hGH from the Penn Vector Core). The microinjection needle was angled to reach the AON by bypassing the OB and reaching the coordinates +3.0 mm AP, +0.9 mm ML, 3.5 mm DV. The virus was infused at a rate of 50 nl/min. Following infusion, the needle was allowed to settle for 15 min to allow viral diffusion before needle retraction. Four weeks following viral injection mice were transcardially perfused with PBS and 4% paraformaldehyde (PFA) and brains were dissected. After 4 h fixation at 4° C, 75 µm coronal sections were cut on a vibratome then mounted and visualized under a fluorescent microscope (Leica DM5000B). Outlines of brain regions were added based on matching coronal sections from the Allen Mouse Brain Reference Atlas.

***Immunohistochemistry***

In epithelial immunostaining experiments mice were deeply anesthetized with ketamine/xylazine (200 mg/kg body weight) before decapitation. The heads were fixed in 4% PFA overnight at 4° C. The tissue was decalcified in 0.5 M EDTA (pH 8.0, ethylenediaminetetraacetic acid) for 4 days and infiltrated in a series of sucrose solutions before being embedded in OCT. The frozen sections were cut into 20 µm coronal sections on a cryostat. After antigen retrieval in a 95° water bath for 10 min, the tissue sections were blocked for 60 min in 0.3% Triton X-100 in PBS with 3% bovine serum albumin, and then incubated at 4° C with primary antibodies in the same solution overnight. Primary antibodies included chicken anti-OMP59 (1:500) and mouse

monoclonal SUS-460 (1:100). Immunofluorescence was achieved by reaction with appropriate secondary antibodies (Molecular Probes, Invitrogen) including goat anti-chicken-568 (A11041) and donkey anti-mouse-488 (A21202) at 1:200 for 1 h. Tissues were washed in 0.3% Triton X-100 in PBS and mounted in Vectashield (Vector Laboratories). Fluorescent images were taken under a SP5/Leica confocal microscope with LAS AF software.

***Patch Clamp***

Adult mice (8-12 weeks old, either gender) were deeply anesthetized with ketamine/xylazine and decapitated. The brain was dissected out and immediately placed in ice-cold Ringer's solution containing (in mM) 124 NaCl, 3 KCl, 1.3 $MgSO_4$, 2 $CaCl_2$, 26 $NaHCO_3$, 1.25 $NaH_2PO_4$, 5.5 glucose and 4.47 sucrose; osmolality ~305 mOsm and pH 7.4 bubbled continuously with 95% $O_2$ balance $CO_2$. Coronal slices (300 µm) were cut using a Leica VT 1200S vibratome. Slices were incubated in oxygenated Ringer's solution for 1 h at room temperature before use. For recordings, slices were transferred to a recording chamber and continuously perfused with oxygenated Ringers. $Td^+$ cells were visualized using an Olympus 40X water-immersion objective on a BX51WI upright microscope equipped with epifluorescence. Recording pipettes were made from borosilicate glass with a Flaming-Brown puller (Sutter Instruments). The tip resistance was 5-10 MΩ and the pipette solution contained (in mM) 120 K-gluconate, 10 KCl, 2 MgATP, 0.5 NaGTP, 20 HEPES, 0.5 EGTA, and 10 phosphocreatine di(tris) salt at a pH of 7.4 and osmolality of 300 mOsm. ChR2 was activated using whole field light stimulation via a 473 nm blue laser (FTEC2473V65-YF0, Blue Sky Research).

Recordings were controlled by an EPC-9 amplifier combined with Pulse Software (HEKA Electronics). Signals were filtered at 2.9 kHz and acquired at 10 kHz.

***Data Analysis***

Acquired electrophysiological data were processed offline using custom Matlab (Mathworks) scripts and Chronux, an open-source software package for analyzing neural data (Bokil et al., 2010). Raw voltage signals from neighboring bipolar electrodes were down-sampled to 2500 samples/sec then compared to achieve local measurements of brain activity and reduce the influence of far-field contamination (see **Results** section for justification of our recording strategy and discussion of volume conduction). The analysis were done on long, continuous freezing periods and compared with equivalent length non-freezing periods taken during the free exploration period before the presentation of the first tone. In cases where signals were bandpass filtered to analyze low frequency activity (2-12 Hz) we used the zero-phase digital filter (Matlab's *filtfilt* forward-reverse filter).

*Power spectral analysis*: We used Welch's method to estimate the power of LFP signals at different frequencies using periodogram spectra estimates to reduce noise (Matlab's built-in *pwelch* function). To calculate the power spectrum hamming windows of 5000 samples (2 s) were used with an overlap of 1250 samples (0.5 s). During periods of freezing the power spectra were characterized by a clear peak at low frequencies. Often we defined the respiration rate during freezing as the exact frequency where these peaks were found.

*Instantaneous respiratory frequency*: Instantaneous frequency was measured by calculating the time between consecutive peaks (exhalations) in the respiratory signal (determined using the built-in *findpeaks* Matlab function).

*Bandpower*: To determine the percentage of the total power in a specified frequency interval we used the built in Matlab function *bandpower* to calculate the power from 2 Hz to 6 Hz then compared that to the power in a wider band (1 Hz to 100 Hz).

*Cohereogram*: Time-frequency coherence was estimated using the function *tfcohf* (Mehrkanoon et al., 2013) which estimates the complex coherence coefficients using the Fourier decomposition of two input signals. Data were decomposed using a 1 s window and smoothed over a time-frequency area of 10 Hz by 13 s.

*Cross-correlation*: We used the built in Matlab function *xcorr* with the 'coeff' option to calculate the cross-correlation between low-pass filtered LFP signals. The maximum correlation between the signals was used to define the cross-correlation.

*Coherence*: Coherence spectra were calculated using the Chronux function *coherencyc* which uses a multi-taper approach to estimate the phase coherence between two signals. The multi-taper method reduces estimation error by taking multiple independent estimates from the same sample. Increasing the number of tapers used reduces the variance of the spectrum (Melman and Victor, 2016).

*Phase analysis*: To compute phase differences raw LFP signals were bandpass filtered. Next, we estimated the instantaneous phase of the signals at each time point *t* during freezing using the Hilbert transform (the built in Matlab function *hilbert*) then defined the phase difference as $\varphi_1(t) - \varphi_2(t)$. Using these phase differences we analyzed the phase difference distributions using Matlab's circular statistics toolbox. We also used

the phase differences to compute the average phase locking value (PLV) over time (the total length of freezing). The PLV measures the variability of the phase difference over time.

*Data shuffling*: We determined chance levels of signal coherence between OB LFPs and respiration by shuffling data (i.e. computed the coherence between temporally mismatched segments of data). Specifically, we rearranged 250 ms bins of raw OB signals and recomputed the coherence between these shuffled OB traces and respiration traces.

All statistical analysis was performed in GraphPad Prizm 7 (San Diego, CA). Parametric tests were used if the data were considered normally distributed (Shapiro-Wilk normality test) with equal variance between groups. If data were not normally distributed the non-parametric Wilcoxon matched-pairs signed rank test or Mann-Whitney U test were used. Data from all completed experiments are included. The experimental sample sizes were powered at 0.9 to observe the effects at the significance level of 0.05 following the 'Guidelines for the Care and Use of Mammals in Neuroscience and Behavioral Research' (http://www.ncbi.nlm.nih.gov/books/NBK43321).

## References


Biskamp J, Bartos M, Sauer JF (2017) Organization of prefrontal network activity by respiration-related oscillations. Sci Rep 7:45508.

Blanchard DC, Griebel G, Pobbe R, Blanchard RJ (2011) Risk assessment as an evolved threat detection and analysis process. Neurosci Biobehav Rev 35:991-998.

Bokil H, Andrews P, Kulkarni JE, Mehta S, Mitra PP (2010) Chronux: a platform for analyzing neural signals. J Neurosci Meth 192:146-151.

Buzsaki G (2010) Neural syntax: cell assemblies, synapsembles, and readers. Neuron 68:362-385.

Buzsaki G, Freeman W (2015) Editorial overview: brain rhythms and dynamic coordination. Curr Opin Neurobiol 31:v-ix.

Cardin JA, Carlen M, Meletis K, Knoblich U, Zhang F, Deisseroth K, Tsai LH, Moore CI (2009) Driving fast-spiking cells induces gamma rhythm and controls sensory responses. Nature 459:663-667.

Chanes L, Quentin R, Tallon-Baudry C, Valero-Cabre A (2013) Causal frequency-specific contributions of frontal spatiotemporal patterns induced by non-invasive neurostimulation to human visual performance. The Journal of neuroscience : the official journal of the Society for Neuroscience 33:5000-5005.

Chen ZB, Eldridge FL, Wagner PG (1992) Respiratory-Associated Thalamic Activity Is Related to Level of Respiratory Drive. Respir Physiol 90:99-113.

Cho JH, Deisseroth K, Bolshakov VY (2013) Synaptic encoding of fear extinction in mPFC-amygdala circuits. Neuron 80:1491-1507.

Craig AD (2009) How do you feel - now? The anterior insula and human awareness. Nature Reviews Neuroscience 10:59-70.

Crapse TB, Sommer MA (2008) Corollary discharge across the animal kingdom. Nat Rev Neurosci 9:587-600.

Demaree RG, Demaree RG, Simpson DD (1974) Respiratory Phase and Visual Signal-Detection. Percept Psychophys 16:337-339.

Ebert D, Rassler B, Hefter H (2000) Coordination between breathing and forearm movements during sinusoidal tracking. Eur J Appl Physiol 81:288-296.

Fontanini A, Bower JM (2006) Slow-waves in the olfactory system: an olfactory perspective on cortical rhythms. Trends Neurosci 29:429-437.

Francis JT, Gluckman BJ, Schiff SJ (2003) Sensitivity of neurons to weak electric fields. The Journal of neuroscience : the official journal of the Society for Neuroscience 23:7255-7261.

Frohlich F, McCormick DA (2010) Endogenous electric fields may guide neocortical network activity. Neuron 67:129-143.

Gallego J, Perruchet P, Camus JF (1991) Assessing attentional control of breathing by reaction time. Psychophysiology 28:217-224.

Gore BB, Soden ME, Zweifel LS (2013) Manipulating gene expression in projection-specific neuronal populations using combinatorial viral approaches. Curr Protoc Neurosci 65:4 35 31-20.

Gross CT, Canteras NS (2012) The many paths to fear. Nat Rev Neurosci 13:651-658.

Hassanpour MS, Simmons WK, Feinstein JS, Luo Q, Lapidus RC, Bodurka J, Paulus MP, Khalsa SS (2018) The Insular Cortex Dynamically Maps Changes in Cardiorespiratory Interoception. Neuropsychopharmacology 43:426-434.

Hayward LF, Swartz CL, Davenport PW (2003) Respiratory response to activation or disinhibition of the dorsal periaqueductal gray in rats. J Appl Physiol 94:913-922.

Hayward LF, Castellanos M, Davenport PW (2004) Parabrachial neurons mediate dorsal periaqueductal gray evoked respiratory responses in the rat. J Appl Physiol 96:1146-1154.

Huang ZG, Subramanian SH, Balnave RJ, Turman AB, Moi Chow C (2000) Roles of periaqueductal gray and nucleus tractus solitarius in cardiorespiratory function in the rat brainstem. Respir Physiol 120:185-195.

Isosaka T, Matsuo T, Yamaguchi T, Funabiki K, Nakanishi S, Kobayakawa R, Kobayakawa K (2015) Htr2a-Expressing Cells in the Central Amygdala Control the Hierarchy between Innate and Learned Fear. Cell 163:1153-1164.

Ito J, Roy S, Liu Y, Cao Y, Fletcher M, Lu L, Boughter JD, Grun S, Heck DH (2014) Whisker barrel cortex delta oscillations and gamma power in the awake mouse are linked to respiration. Nat Commun 5.

Iwabe T, Ozaki I, Hashizume A (2014) The respiratory cycle modulates brain potentials, sympathetic activity, and subjective pain sensation induced by noxious stimulation. Neurosci Res 84:47-59.

Karalis N, Sirota A (2018) Breathing coordinates limbic network dynamics underlying memory consolidation. bioRxiv (Preprint).

Karalis N, Dejean C, Chaudun F, Khoder S, Rozeske RR, Wurtz H, Bagur S, Benchenane K, Sirota A, Courtin J, Herry C (2016) 4-Hz oscillations synchronize prefrontal-amygdala circuits during fear behavior. Nat Neurosci 19:605-612.

LeDoux JE (2000) Emotion circuits in the brain. Annu Rev Neurosci 23:155-184.

Lee AC, He JW, Ma MH (2011) Olfactory Marker Protein Is Critical for Functional Maturation of Olfactory Sensory Neurons and Development of Mother Preference. J Neurosci 31:2974-2982.

Lein ES et al. (2007) Genome-wide atlas of gene expression in the adult mouse brain. Nature 445:168-176.

Li S, Park WH, Borg A (2012a) Phase-dependent respiratory-motor interactions in reaction time tasks during rhythmic voluntary breathing. Motor Control 16:493-505.

Li SY, Bai WW, Liu TT, Yi H, Tian X (2012b) Increases of theta-low gamma coupling in rat medial prefrontal cortex during working memory task. Brain Res Bull 89:115-123.

Likhtik E, Popa D, Apergis-Schoute J, Fidacaro GA, Pare D (2008) Amygdala intercalated neurons are required for expression of fear extinction. Nature 454:642-645.

Lojowska M, Gladwin TE, Hermans EJ, Roelofs K (2015) Freezing Promotes Perception of Coarse Visual Features. J Exp Psychol Gen 144:1080-1088.

Lutz A, Greischar LL, Rawlings NB, Ricard M, Davidson RJ (2004) Long-term meditators self-induce high-amplitude gamma synchrony during mental practice. P Natl Acad Sci USA 101:16369-16373.

Marder E, Calabrese RL (1996) Principles of rhythmic motor pattern generation. Physiol Rev 76:687-717.

Marshall L, Helgadottir H, Molle M, Born J (2006) Boosting slow oscillations during sleep potentiates memory. Nature 444:610-613.

Masquelier T, Hugues E, Deco G, Thorpe SJ (2009) Oscillations, phase-of-firing coding, and spike timing-dependent plasticity: an efficient learning scheme. The Journal of neuroscience : the official journal of the Society for Neuroscience 29:13484-13493.

Mehrkanoon S, Breakspear M, Daffertshofer A, Boonstra TW (2013) Non-identical smoothing operators for estimating time-frequency interdependence in electrophysiological recordings. Eurasip J Adv Sig Pr.

Melman T, Victor JD (2016) Robust power spectral estimation for EEG data. J Neurosci Meth 268:14-22.

Miller KM, Perry PA (1990) Relaxation technique and postoperative pain in patients undergoing cardiac surgery. Heart Lung 19:136-146.

Ozen S, Sirota A, Belluscio MA, Anastassiou CA, Stark E, Koch C, Buzsaki G (2010) Transcranial electric stimulation entrains cortical neuronal populations in rats. The Journal of neuroscience : the official journal of the Society for Neuroscience 30:11476-11485.

Radman T, Su Y, An JH, Parra LC, Bikson M (2007) Spike timing amplifies the effect of electric fields on neurons: implications for endogenous field effects. The Journal of neuroscience : the official journal of the Society for Neuroscience 27:3030-3036.

Rassler B, Raabe J (2003) Co-ordination of breathing with rhythmic head and eye movements and with passive turnings of the body. Eur J Appl Physiol 90:125-130.

Root CM, Denny CA, Hen R, Axel R (2014) The participation of cortical amygdala in innate, odour-driven behaviour. Nature 515:269-273.

Saito H, Nishizumi H, Suzuki S, Matsumoto H, Ieki N, Abe T, Kiyonari H, Morita M, Yokota H, Hirayama N, Yamazaki T, Kikusui T, Mori K, Sakano H (2017) Immobility responses are induced by photoactivation of single glomerular species responsive to fox odour TMT. Nat Commun 8:16011.

Siegle JH, Pritchett DL, Moore CI (2014) Gamma-range synchronization of fast-spiking interneurons can enhance detection of tactile stimuli. Nat Neurosci 17:1371-1379.

Strobel C, Marek R, Gooch HM, Sullivan RK, Sah P (2015) Prefrontal and Auditory Input to Intercalated Neurons of the Amygdala. Cell Rep.

Subramanian HH, Balnave RJ, Holstege G (2008) The midbrain periaqueductal gray control of respiration. The Journal of neuroscience : the official journal of the Society for Neuroscience 28:12274-12283.

Thut G, Veniero D, Romei V, Miniussi C, Schyns P, Gross J (2011) Rhythmic TMS Causes Local Entrainment of Natural Oscillatory Signatures. Current Biology 21:1176-1185.

Tovote P, Esposito MS, Botta P, Chaudun F, Fadok JP, Markovic M, Wolff SB, Ramakrishnan C, Fenno L, Deisseroth K, Herry C, Arber S, Luthi A (2016) Midbrain circuits for defensive behaviour. Nature 534:206-212.

Yang CF, Feldman JL (2018) Efferent projections of excitatory and inhibitory preBotzinger Complex neurons. J Comp Neurol 526:1389-1402.

# APPENDIX: THE STEM CELL MARKER LGR5 DEFINES A SUBSET OF POST-MITOTIC NEURONS IN THE OLFACTORY BULB

## Introduction

The maintenance and repair of adult tissues depends on specialized stem cells. Specific molecular markers have been identified and used to characterize and track these stem cells. Finding reliable stem cell markers allows researchers to investigate how stem cells self-renew and pursue their respective lineage which has important clinical implications. Recently, Lgr5, leucine-rich repeat containing G protein-coupled receptor 5, has been established as an adult stem cell marker in the small intestine and colon, stomach, hair follicles, kidneys, mammary glands, and ovaries (Barker et al., 2007; Jaks et al., 2008; Barker et al., 2010; Tian et al., 2011; Barker et al., 2012; de Visser et al., 2012; Leushacke et al., 2013; Plaks et al., 2013; Ng et al., 2014; Sun et al., 2014). By binding to R-spondin ligands (secreted Wnt signaling agonists) Lgr5 mediates the Wnt pathway and plays a critical role in embryonic development and cell genesis in adult tissues (Carmon et al., 2011; de Lau et al., 2011; Glinka et al., 2011; de Lau et al., 2014; Moberly et al., 2018). Lgr5 also labels stem cells in sensory organs such as the eye, ear, tongue, and nose (Shi et al., 2012; Hirata-Tominaga et al., 2013; Shi et al., 2013; Yee et al., 2013; Bramhall et al., 2014; Chen et al., 2014). Lgr5 is also expressed in several neuronal subtypes including mouse retinal amacrine cells and cerebellar granule neurons. This suggests a potential role of Lgr5 in cells other than epithelial stem cells (Miller et al., 2014; Sukhdeo et al., 2014).

Interestingly, Lgr5 is highly expressed in the olfactory bulb (OB) the first relay station in the brain for processing odor information and one of the few neural structures that undergoes adult neurogenesis (Ming and Song, 2011; Lepousez et al., 2015). Olfactory sensory neurons (OSNs) in the nose project to the OB and form synapses in specialized structures called glomeruli. The OB projection neurons (the mitral/tufted cells) subsequently carry information to the olfactory cortices. The OB can be divided into different anatomically defined layers from the surface to the center: the glomerular layer (GL), the external plexiform layer (EPL), the mitral cell layer (MCL), the internal plexiform layer (IPL), the granule cell layer (GCL), and the core region which is continuous with the rostral migratory stream (RMS). The RMS originates from the subventricular zone (Lledo et al., 2008; Whitman and Greer, 2009). Each layer contains heterogeneous cell populations that can be characterized by distinct morphologies, molecular markers, and electrophysiological properties (McQuiston and Katz, 2001; Parrish-Aungst et al., 2007; Batista-Brito et al., 2008; Kiyokage et al., 2010; Kosaka and Kosaka, 2011). For example, in the glomerular layer, juxtaglomerular cells surrounding individual glomeruli are divided into three main subtypes: the external tufted cells (ET), periglomerular cells (PG), and short axon cells (SA). However, despite the high expression of *Lgr5* in the OB, the identity and properties of $Lgr5^{+}$ cells here remain uncharacterized. However, our data indicate that Lgr5-$EGFP^{+}$ cells in the OB represent a non-stem cell lineage, implying that LGR5 has distinct roles in post-mitotic neurons.

### Lgr5 does not label stem cells in the OB

Adult neurogenesis only occurs in a few brain structures including the OB (Ming and Song, 2011). Since Lgr5 labels stem cells in many organs, we asked whether Lgr5 is expressed in the brain. In adult Lgr5-EGFP mice, the OB is the only brain structure that shows high levels of Lgr5 expression. The Lgr5-EGFP expression pattern is consistent with a previous report and with *Lgr5* mRNA expression from the Allen Mouse Brain Atlas (Miller et al., 2014). Within the OB, Lgr5-EGFP+ cells are found primarily in the glomerular layer, mitral cell layer, and granule cell layer (**Figure A.1**).

Next, we stained OB sections from adult Lgr5-EGFP mice with Sox2 and Nestin, two stem cell markers in the nervous system (**Figure A.2**). We found that Lgr5+ cells do not coexpress either marker. Furthermore, Lgr5-EGFP$^+$ cells are not proliferating cells as they do not coexpress Ki67 or incorporate BrdU. Similar results were also observed in embryonic and neonatal mice. Thus, Lgr5 does not mark stem cells in the OB from early development to adulthood.

To further confirm that Lgr5-EGFP$^+$ cells in the OB do not function as stem cells, we performed genetic linage tracing experiments by crossing Lgr5-EGFP-cre/ERT2 mice with Rosa26-floxed STOP-tdTomato mice. Upon tamoxifen induction, Lgr5-EGFP$^+$ cells would be marked by expression of both EGFP and tdTomato. If some LGR5-EGFP$^+$ cells are stem cells they will give rise to progeny which are likely to downregulate the expression of Lgr5 and will thus be tdTomato$^+$ only. Up to 90 days post tamoxifen injection, we found that all tdTomato$^+$ cells also express EGFP (**Figure A.3**), suggesting that tdTomato$^+$ cells are not the progenies of Lgr5-EGFP$^+$ cells but are instead Lgr5-EGFP$^+$ cells themselves.

### Lgr5-EGFP$^+$ cells are terminally differentiated neurons in the OB

To reveal the identities of Lgr5-EGFP$^+$ cells in the OB, we stained OB sections from adult Lgr5-EGFP mice with a variety of cell markers. Nearly all Lgr5-EGFP$^+$ cells in different layers of the OB were positively stained with NeuroTrace Nissl, suggesting that Lgr5-EGFP$^+$ cells are neurons (**Figure A.4**). Consistently, Lgr5-EGFP$^+$ cells do not express GFAP (an astrocyte marker), and a subset are stained by NeuN, a nuclear marker for a subset of mature neurons in the OB. Within the glomerular layer, nearly half of Lgr5-EGFP$^+$ cells express tyrosine hydroxylase (TH) the rate limiting enzyme in the biosynthesis of dopamine. These TH$^+$ cells are also GABAergic because virtually all TH$^+$ cells also express GAD67 and subset expresses GAD65 (Parrish-Aungst et al., 2007; Kiyokage et al., 2010). Therefore, we quantified Lgr5-EGFP$^+$ cells based on their TH and GAD65 expression: Lgr5$^+$TH+GAD65$^+$ (26%), Lgr5$^+$TH$^+$GAD65- (24%), Lgr5$^+$TH$^-$ GAD65$^+$ (13%), and Lgr5$^+$TH$^-$GAD65$^-$ (37%).

These results indicated that these molecules define distinct but overlapping subpopulations of neurons. Similar lineage tracing experiments confirmed that some TH$^+$ and GAD65$^+$ cells are Lgr5$^+$, but they are unlikely to by the progeny of Lgr5-EGFP$^+$ cells since all tdTomato+ cells are also positive for EGFP (**Figure A.5**). In contrast, Lgr5-EGFP$^+$ cells do not express the calcium binding protein calbindin (CB) or calretinin (CR) which together account for nearly 38% of the neurons in the glomerular layer (Parrish-Aungst et al., 2007). Consistently, none of the CB$^+$ or CR$^+$ cells are the progeny of Lgr5-EGFP$^+$ cells. In the mitral cell layer, more than 40% of Lgr5-EGFP$^+$ cells also express the leucine-rich repeat membrane protein, 5T4 oncofetal trophoblast glycoprotein, which labels a subset of superficial GABAergic granule cells that are in or very near to the

mitral cell layer (Imamura et al., 2006; Yoshihara et al., 2012). We observe a small population of Lgr5-EGFP$^+$/5T4$^+$ cells in the glomerular layer as well. Additionally, double *in situ* hybridization experiments reveal that some *lgr5*$^+$ cells in the MCL and the GL/EPL boundary express *vglut1*, supporting that these cells are glutamatergic mitral and tufted cells, respectively. These data show that Lgr5 is expressed in multiple neuronal subtypes within different layers of the mouse OB.

### Lgr5 is expressed in neurons at different maturation stages

Because interneurons in the OB are continuously replenished from neuroblast cells that migrate via the RMS from the SVZ, we asked whether Lgr5-EGFP$^+$ cells are at different maturation stages (Lledo et al., 2008; Cave and Baker, 2009; Whitman and Greer, 2009). We noted that there is no Lgr5-EGFP expression in the OB core region, RMS, or SVG. It is most likely that Lgr5 expression is initiated after the neuroblast successfully migrate to the OB, although we cannot rule out the possibility that some Lgr5-EGFP$^+$ neurons are generated locally in the OB. As neurons mature, they downregulate the expression of DCX (a microtubule-associated protein expressed in neuronal precursor cells and immature neurons) and upregulate the expression of NeuN (Brown et al., 2003). In addition to NeuN$^+$Lgr5-EGFP$^+$ cells, a subset of Lgr5-EGFP+ cells (15% in the GCL and 10% in the MCL) coexpress DCX. Similarly, Lgr5-EGFP$^+$TH$^+$ cells also both contain DCX$^+$ (21%) and NeuN$^+$ (30%) populations (**Figure A.6**). These data suggest that Lgr5 is expressed in OB neurons that are at different developmental stages.

### Unlike TH and 5T4, Lgr5 expression is not activity-dependent

Because both TH and 5T4 show activity dependent-expression in the OB and overlap with Lgr5 expression we asked whether Lgr5 expression is likewise activity-dependent (Baker et al., 1993; Yoshihara et al., 2012). Unilateral naris occlusion was performed on neonatal mice and Lgr5-EGFP expression was compared between open and closed sides 30 days later. No significant difference was observed in the number of Lgr5-EGFP$^+$ cells within different layers of the OB (**Figure A.7**). In contrast, in the glomerular layer, the percentage of TH$^+$ cells among Lgr5-EGFP$^+$cells decreased by 36% in the closed side (due to reduced TH expression). Similarly, in the mitral cell layer, the percentage of 5T4$^+$ cells among Lgr5-EGFP$^+$ cells decreased by 42% in the closed side. We next examined whether sensory deprivation affects maturation of Lgr5-EGFP$^+$ cells. The percentage of DCX$^+$ cells among Lgr5-EGFP$^+$ cells in the GL was increased by 48% in the closed side and increased by 126% in the GCL. This indicates that sensory deprivation leads to accumulation of immature Lgr5-EGFP$^+$ neurons. Thus, Lgr5 does not show activity-dependent expression in the OB, even though olfactory sensory input plays a role in the maturation of these cells.

### Lgr5-EGFP+ cells have heterogeneous electrophysiological properties

We further investigated the functional properties of Lgr5-EGFP$^+$ neurons in the OB by performing patch-clamp recordings in the glomerular cell layer where we observe the strongest Lgr5-EGFP expression (**Figure A.8**). Under current-clamp mode, depolarizing current injections caused action potentials in all Lgr5-EGFP$^+$ cells. The firing patterns of both Lgr5-EGFP$^+$ and neighboring Lgr5-EGFP- cells in the glomerular

layer could be characterized as tonic firing, delayed firing, bursting, or single spike, similar to blind recordings from glomerular neuronal populations (McQuiston and Katz, 2001).

Juxtaglomerular neurons participate in inter- and intra-glomerular circuits, making synaptic contacts with incoming sensory neuron axon terminals, mitral and tufted cell dendrites, and other local and distant juxtaglomerular cells. Spontaneous excitatory postsynaptic currents (sEPSCs) in Lgr5-EGFP$^{+}$ cells demonstrate that these cells are integrated into OB circuits and receive synaptic input. Curiously, spontaneous EPSCs recorded in Lgr5-EGFP$^{+}$ cells exhibitied similar event frequencies but significantly larger amplitudes compared to Lgr5-EGFP$^{-}$ cells.

### An Lgr5 ligand (R-spondin 3) is expressed in the olfactory bulb

In other cell types and tissues, Lgr5 has been shown to bind R-spondins and regulate the Wnt signaling pathway (Carmon et al., 2011; de Lau et al., 2011; Glinka et al., 2011). The R-spondin family consists of four secreted proteins (R-spondin 1-4), all of which are potential ligands for Lgr5. We searched the *in situ* hybridization data from the Allen Mouse Brain Atlas and the Allen Developing Mouse Brain Atlas and found that only R-spondin 3 is expressed in the adult OB, which we further confirmed by double *in situ* hybridization of *Lgr5* and *R-spondin 3* (**Figure A.9**). This suggests that Lgr5 is activated by an endogenous ligand in the OB.

Given that Lgr5-EGFP$^{+}$ cells showed larger sEPSCs compared to Lgr5-EGFP$^{-}$ cells, we wondered if the binding of R-spondin 3 to Lgr5 could have either an acute effect on synaptic function of chronic effects on synaptic formation or maintenance via

Wnt signaling. We directly assessed the first possibility by examining the effect of R-spondin 3 perfusion on the electrophysiological properties of Lgr5-EGFP+ cells using whole-cell patch clamp and perforated patch clamp. The latter recording configuration maintains the integrity of second messenger signaling cascades while gaining electrical access to the cell via the formation of antibiotic pores. Perfusing R-spondin 3 (at 100 ng/ml, or 3.5 nM) for 10 min did not cause significant changes in resting membrane potentials or sEPSCs (**Figure A.9**). This concentration of R-spondin 3 is presumably a saturating dose since the median effective dose is < 1 ng/ml according to the manufacturer's datasheet and the half-maximum effective concentration is 0.01 nM in cultured cells (Carmon et al., 2011). These results suggest that Lgr5 and its ligand may not have acute effects but instead exert their function in the OB in a chronic manner (discussed below).

## Discussion

Here, we investigated the identity and properties of Lgr5-EGFP$^+$ cells in the OB using an Lgr5 reporter mouse line and genetic lineage tracing. Immunostaining with molecular markers showed that Lgr5-EGFP$^+$ cells are not stem cells but are fully differentiated neurons of various subtypes and maturation stages. Patch clamp recordings revel that these neurons fire action potentials and display spontaneous postsynaptic events. Genetic lineage tracing demonstrates that Lgr5-EGFP$^+$ cells do not give rise to other cells and instead represent a non-stem cell lineage, implying a novel role for Lgr5 in post-mitotic neural cells.

Lgr5 has been established as a marker for epithelial stem cells in many body organs including sensory organs. The OB is a sensory region that undergoes adult neurogenesis and expresses Lgr5 at high levels. But, Lgr5-EGFP$^{+}$ cells are not progenitor/stem cells in the OB and are instead post-mitotic neuronal cells in different OB layers and at different maturation stages. In the glomerular layer, juxtaglomerular cells are subdivided into three main types. Lgr5 is expression is greater in certain subtypes. Specifically, nearly 50% of Lgr5-EGFP$^{+}$ cells are TH$^{+}$ dopaminergic cells, which account for about 10% of the total number of juxtaglomerular cells (Parrish-Aungst et al., 2007). The Th$^{+}$ cells can be further divided into two main populations including GAD65$^{+}$ uniglomerular (innervating a single glomerulus) and GAD67$^{+}$ multi-glomerular short axon cells which can innervate tens of glomeruli (Kiyokage et al., 2010). Among Lgr5-EGFP$^{+}$ cells, 26% of them express both TH and GAD65 and thus most are likely uniglomerular PG cells. Another 24% express TH but not GAD65 and most likely belong to short axon cells. These cells modulate information transmission in the OB via interglomerular interactions (Kiyokage et al., 2010; Whitesell et al., 2013; Banerjee et al., 2015; Liu et al., 2016).

In contrast, Lgr5 is not expressed in cells that express calcium binding proteins (CB and CR), which comprise 37% of juxtaglomerular cells and define a population of anaxonic (not having a typical axon) PG cells (Parrish-Aungst et al., 2007; Kosaka et al., 2008; Kosaka and Kosaka, 2011). Overall, Lgr5 expression is not random among GABAergic neurons in the glomerular layer but shows a preference for TH$^{+}$ cells over CB$^{+}$ and CR$^{+}$ cells. Note that the immunohistochemistry data may underestimate the percentage of TH$^{+}$ or GAD$^{+}$ cells among Lgr5$^{+}$ cells due to any inefficiency of the

antibodies. Lgr5 is also expressed in some excitatory, external tufted cells located in the GL/EPL boundary.

Similarly, in the mitral cell layer, Lgr5 is expressed in a heterogeneous population of cells including both excitatory and inhibitory neurons with preference for some cell types. Nearly 40% of Lgr5-EGFP$^+$ cells are 5T4$^+$, which labels a subset of superficial granule cells that play a role in the formation and maintenance of dendritic morphology and synapse connectivity (Imamura et al., 2006; Yoshihara et al., 2012). Considering that 5T4$^+$ cells account for only 14% of NeuN$^+$ cells while nearly all 5T4$^+$ cells are NeuN$^+$, Lgr5 expression shows a strong preference in 5T4$^+$ cells. But, Lgr5 expression is not activity dependent, even though both TH and 5T4 expression is significantly lower after naris occlusion. Following permanent naris occlusion and subsequent sensory deprivation, the percentage of Lgr5-EGFP$^+$TH$^+$ and Lgr5-EGFP$^+$5T4$^+$ cells is significantly reduced.

Lgr5 is not only expressed in heterogeneous cell populations but also at different maturation stages. NeuN, a pan neuronal nuclear marker, is expressed in neurons undergoing withdrawal from the cell cycle and or with the initiation of terminal differentiation. Thus, NeuN is used as a marker for mature neurons, especially those that have down regulated the expression of DCX (a marker of early neuronal development). Only a small portion of cells in the OB are NeuN$^+$ (specifically 25% in the GL and 29% in the MCL). Thus, NeuN staining may underestimate the number of mature neurons in the OB. Nonetheless, among Lgr5$^+$ cells, 28% in the GL and 41% in the MCL/GCL are NeuN$^+$ consistent with% (e.g. 43% in the GL and 41% in the MCL/GCL). DCX$^+$ cells are enriched throughout the RMS and generate different subtypes of local interneurons in the

OB. Since we find no Lgr5-EGFP$^{+}$ cells in the RMS, Lgr5 expression is initiated after the progenitor cells eventually reach the OB. Lgr5-EGFP$^{+}$DCX$^{+}$ cells are found in different layers of the OB and likely mature into specific subtypes of mature Lgr5$^{+}$ neurons in the OB. Unilateral naris occlusion causes an increase in the number of Lgr5$^{+}$/DCX$^{+}$ cells in all OB layers, suggesting that the maturation of Lgr5$^{+}$ neurons depends on some extent to olfactory sensory input.

Patch clamp recordings confirm that Lgr5-EGFP$^{+}$ cells comprise a heterogeneous population of neurons. Interestingly, Lgr5-EGFP$^{+}$ cells have spontaneous ESPCs with significantly larger amplitudes as compared to Lgr5-EGFP- cells. This may be due to biased expression of Lgr5 in certain subtypes of juxtaglomerular neurons (such as TH$^{+}$) if these subtypes have larger spontaneous ESPCs. Alternatively, the larger ESPCs may reflect the potential role of Lgr5 and its ligand R-spondin in regulating synaptic connections in the OB. For example, the Wnt signaling pathway plays roles in synapse formation and maintenance and disruption of this pathway leads to synaptic disassembly in neurodegenerative disease (Dickins and Salinas, 2013). Because new neurons are continuously generated and incorporated into OB circuits and the OB is the only brain structure that expresses Lgr5 at high levels in adulthood we speculate that Lgr5 regulates synaptic formation and maintenance in adults via the Wnt signaling pathway (Ming and Song, 2011; Lepousez et al., 2015). Due to the embryonic lethality of Lgr5 knockout, OB-specific Lgr5 knockout or knockdown models are needed to reveal the distinct roles of Lgr5 in the OB.

**Figure A.1. Lgr5 does not label stem cells in the OB.** Coronal sections from adult Lgr5-EGFP mice were stained with the stem cell marker Sox2 (**A**), Nestin (**B**), cell proliferation marker Ki67 (**C**) or BrdU (**D**). Abbreviations: GL, glomerular layer, MCL, mitral cell layer, GCL, granule cell layer. Many $BrdU^+$ cells are in the core region of the OB, where there is no EGFP signal observed. Scale bars: 100 μm (**A**, **B**, **C**, and **D**) and 20 μm (**A2**, **B2**, **C2**, and **D3**).

**Figure A.1.**

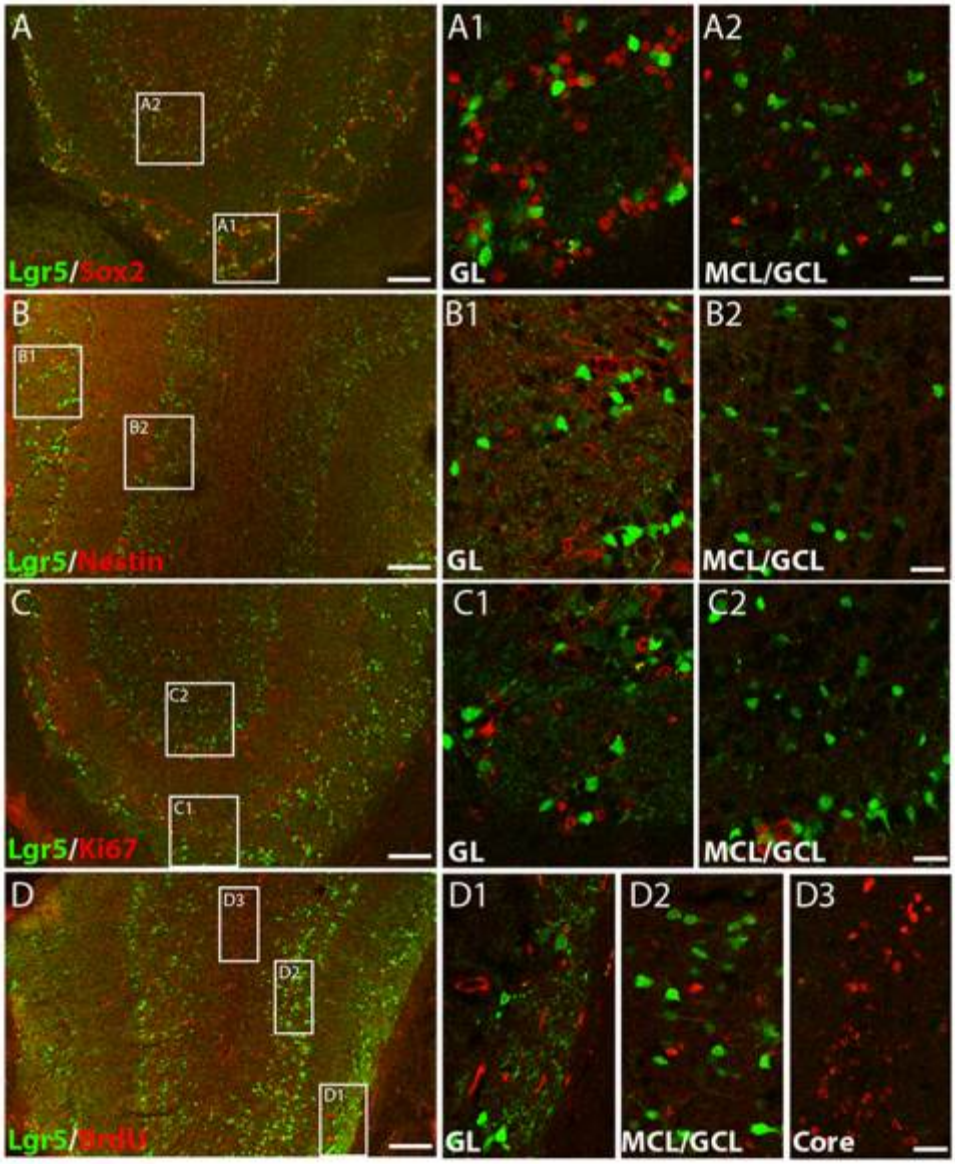
A
A2
A1
Lgr5/Sox2
A1
GL
A2
MCL/GCL
B
B1
B2
Lgr5/Nestin
B1
GL
B2
MCL/GCL
C
C2
C1
Lgr5/Ki67
C1
GL
C2
MCL/GCL
D
D3
D2
D1
Lgr5/BrdU
D1
GL
D2
MCL/GCL
D3
Core

**Figure A.2. Lgr5 does not label stem cells in the OB at prenatal and neonatal stages.** (**A**-**C**) At embryonic day 18 (E18), Lgr5-EGFP$^{+}$ cells do not coexpress Sox2 (**A**, **A1**), Ki67 (**B**, **B1**), or Nestin (**C**, **C1**) in the GL. In the core region where Lgr5-EGFP expression is absent, there are abundant Sox2$^{+}$ cells (**A2**), Ki67+ cells (**B2**), and Nestin$^{+}$ cells (**C2**). (**D**-**F**) At postnatal day 1 (P1), Lgr-EGFP$^{+}$ cells do not express Sox2 (**D**), Ki67 (**E**), or Nestin (**F**) in the GL (**D1**-**F1**) or the MCL/GCL (**D2**-**F2**). Scale bars: 100 μm in **C** and **F** and 20 μm in **C1**, **C3**, **F1**, and **F2**. Each scale bar applies to the entire row.

**Figure A.2.**

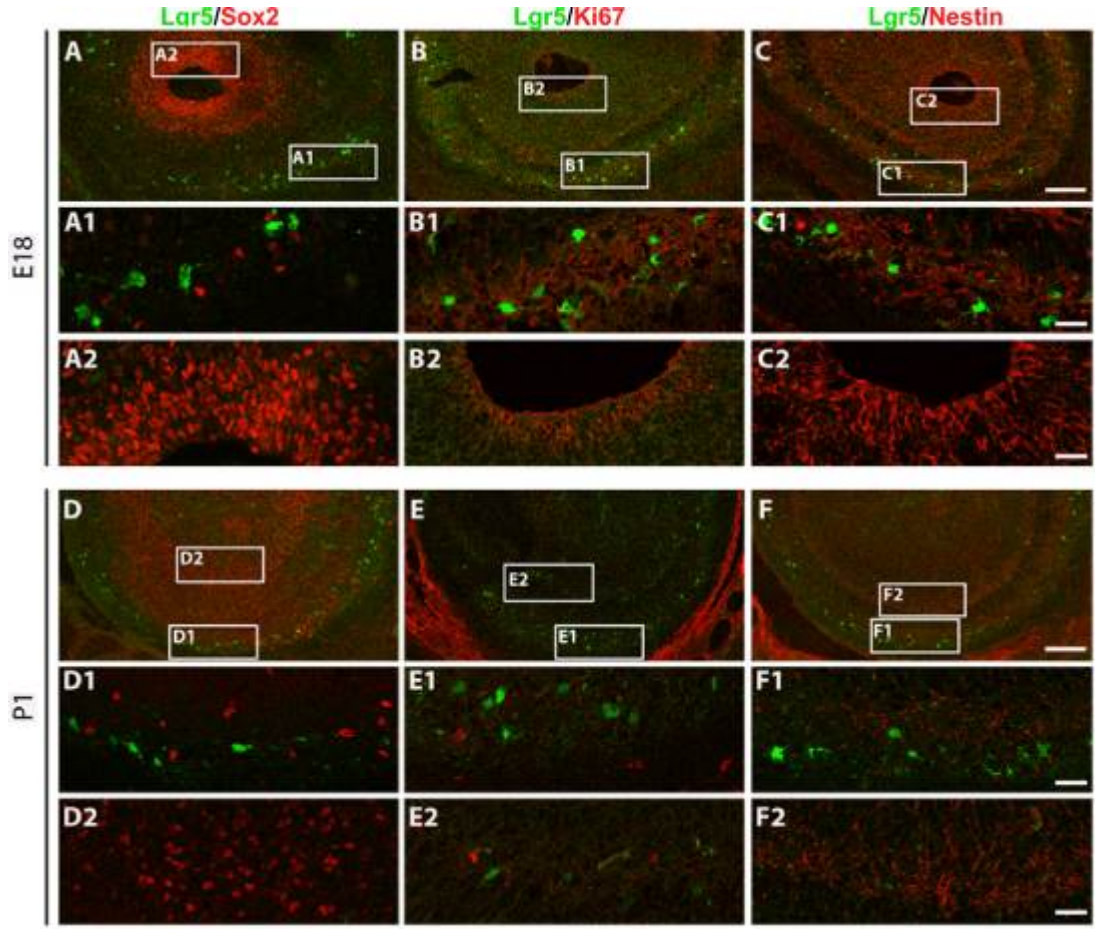
Lgr5/Sox2
Lgr5/Ki67
Lgr5/Nestin
E18
P1
A
A1
A2
B
B1
B2
C
C1
C2
D
D1
D2
E
E1
E2
F
F1
F2

**Figure A.3. Lgr5-EGFP$^+$ cells do not give rise to other cell types in the OB.** Genetic linage tracing was performed in Lgr5-EGFP-cre/ERT2 and Rosa26-floxed STOP-tdTomato mice at 10 days (**A**, **B**) and 90 days (**C**, **D**) after tamoxifen induction. All tdTomato$^+$ cells are also Lgr5-EGFP$^+$ in the GL (arrowheads in **A** and **C**), MCL (arrowheads in **B** and **D**) and GCL (arrowheads in **B** and **D**). Scale bars: 20 μm. Each scale bar applies to the entire row.

**Figure A.3.**

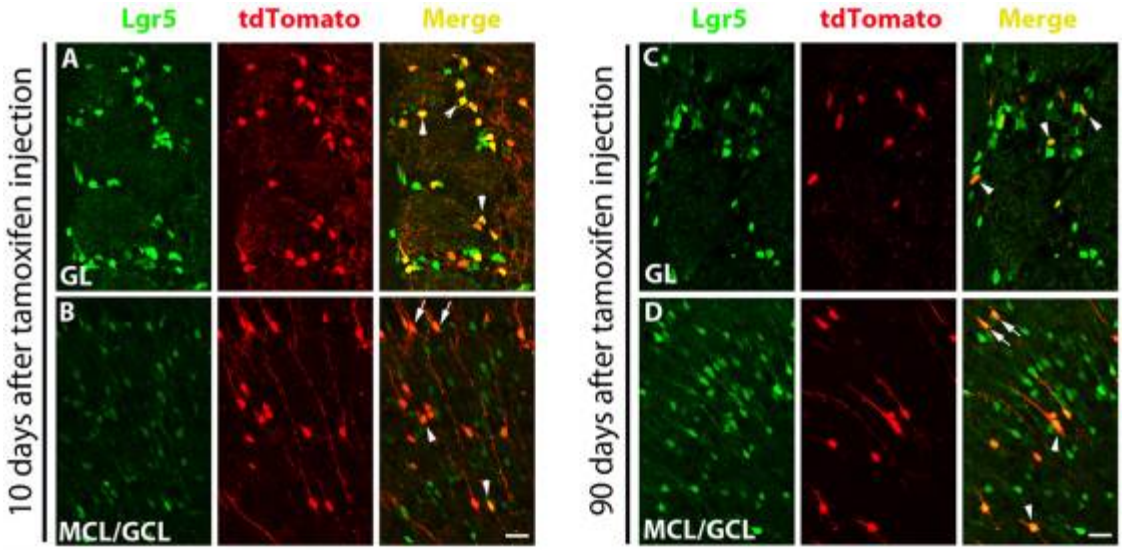
Lgr5
tdTomato
Merge
10 days after tamoxifen injection
A
GL
B
MCL/GCL
Lgr5
tdTomato
Merge
90 days after tamoxifen injection
C
GL
D
MCL/GCL

**Figure A.4. Lgr5 marks several subtypes of neurons in the OB.** (**A**-**D**) Coronal OB sections from adult Lgr5-EGFP mice were stained with Nissl. Nearly all Lgr5-EGFP$^+$ cells are Nissl$^+$ in the GL (**A**, 89%), EPL (**B**, 100%), MCL (**C**, 94%), and GCL (**D**, 84%). (**E**-**H**) Lgr5-EGFP$^+$ cells are not positively stained by astrocyte marker GFAP (**E**), but a subset is positively stained by neuronal cell marker NeuN in the GL (28%) (**F**) and MCL/GCL (41%) (**G**), and by the dopaminergic marker TH (**H**). (**I**-**L**) Lgr5, GAD65, and TH show distinct but overlapping expression in the GL. Examples of cells expression all three molecules (**I**), GAD65 and TH but not Lgr5 (**J**), Lgr5 and TH but not GAD65 (**K**) and a summary of the data from a total of 1804 Lgr5-EGFP$^+$ cells (**L**). (**M**, **N**) Lgr5-EGFP$^+$ cells do not coexpress CB (**M**) or CR (**N**). (**O**) Approximately 41% of Lgr5-EGFP$^+$ cells in the MCL express 5T4. (**P**) A small population of Lgr5$^+$/5T4$^+$ cells are present in the GL. (**Q**-**S**) Double *in situ* hybridization using *lgr5* and *vglut1* riboprobes show coexpression of these two genes in a subset of cells (**Q**) located at the MCL (**R**) and GL/EPL border (**S**). Scale bars: 10 μm in **D**, **H**, and **P**, 100 μm in **Q**, and 20 μm in **S** and **R**.

**Figure A.4.**

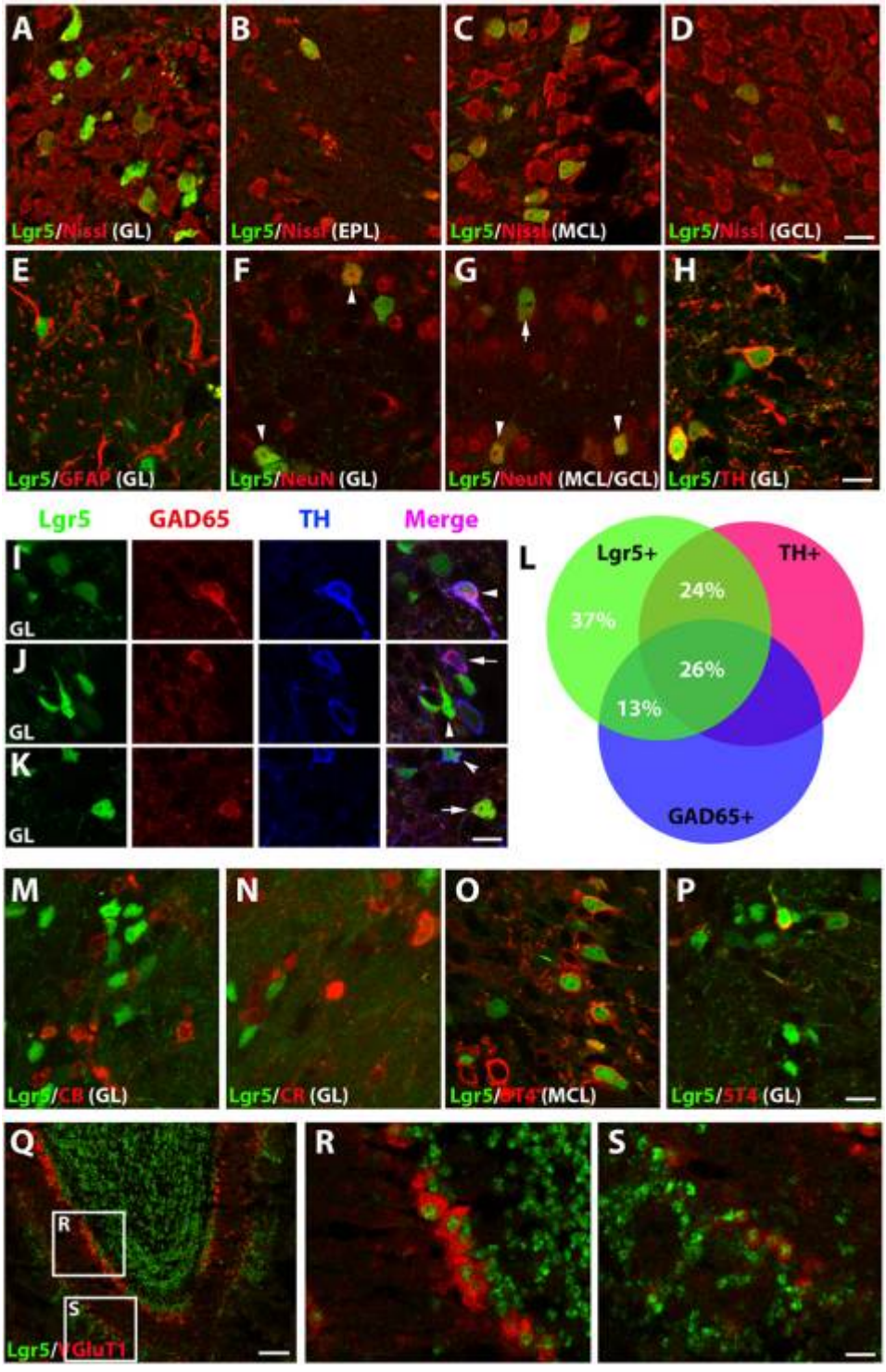
A
Lgr5/Nissl (GL)
B
Lgr5/Nissl (EPL)
C
Lgr5/Nissl (MCL)
D
Lgr5/Nissl (GCL)
E
Lgr5/GFAP (GL)
F
Lgr5/NeuN (GL)
G
Lgr5/NeuN (MCL/GCL)
H
Lgr5/TH (GL)
Lgr5
GAD65
TH
Merge
I
GL
J
GL
K
GL
L
Lgr5+
TH+
GAD65+
24%
37%
26%
13%
M
Lgr5/CB (GL)
N
Lgr5/CR (GL)
O
Lgr5/ST4 (MCL)
P
Lgr5/ST4 (GL)
Q
R
S
Lgr5/VGluT1
R
S

**Figure A.5. Lgr5-EGFP$^+$ cells do not give rise to other neuronal cell types in the OB.** Genetic lineage tracing was performed in Lgr5-EGFP-cre/ERT2 and Rosa26-floxed STOP-tdTomato mice at 21 days (**A**-**D**) and 90 days (**E**-**H**) after tamoxifen induction. All tdTomato$^+$ cells are also EGFP$^+$, suggesting that they are Lgr5-EGFP$^+$ cell rather than the progeny of Lgr5-EGFP$^+$ cells. Some tdTomato$^+$ cells are TH$^+$ (column 1: **A**, **A'**, **E**, **E'**) and GAD65$^+$ (column 2: **B**, **B'**, **F**, **F'**), while no tdTomato$^+$ cells are CB$^+$ (column 3: **C**, **C'**, **G**, **G'**) or CR$^+$ (column 4: **D**, **D'**, **H**, **H'**). Scale bars: 20 μm in **D** and **H**, 10 μm in **D'** and **H'**. Each scale bar applies to the entire row.

**Figure A.5.**

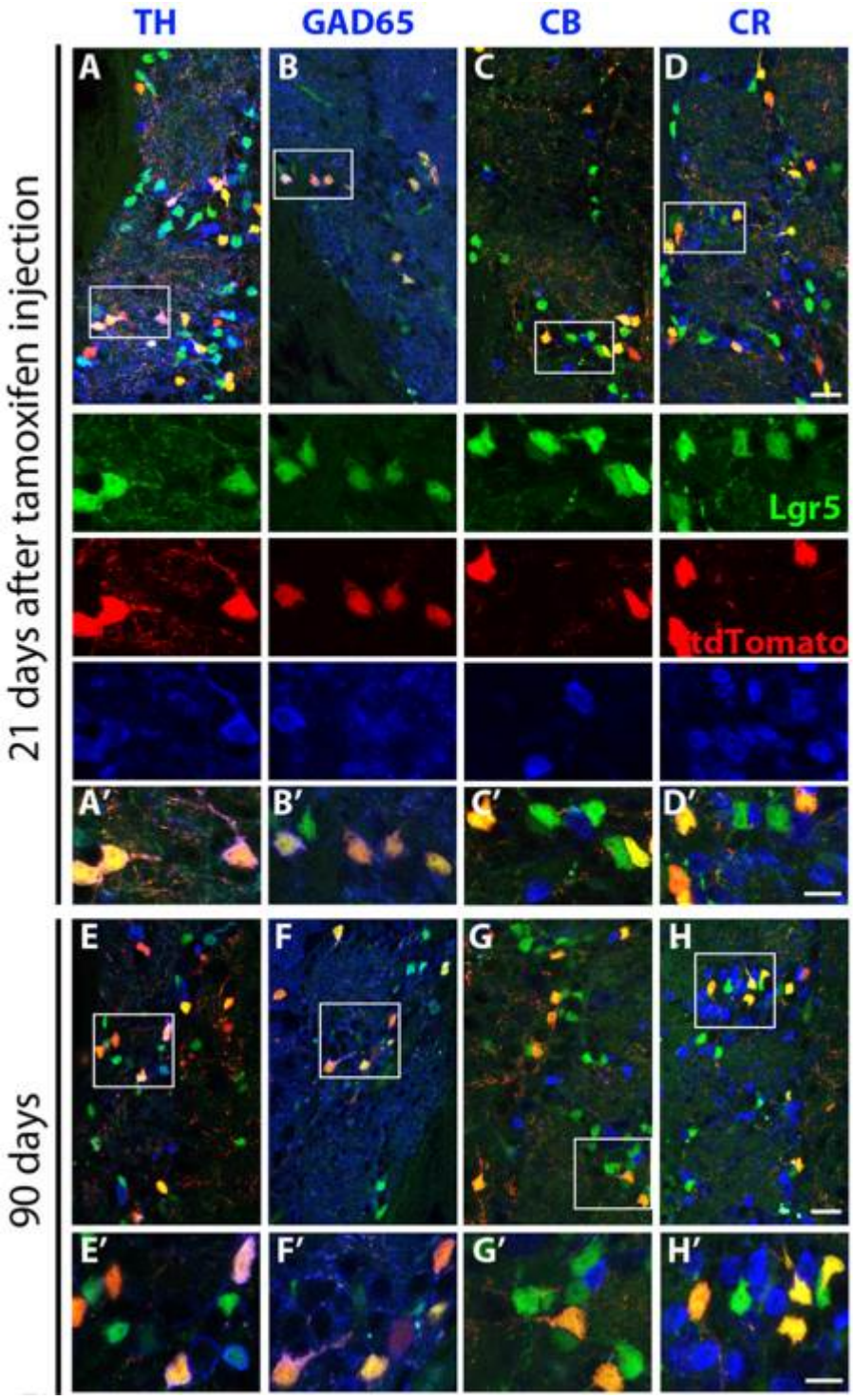
TH
GAD65
CB
CR
21 days after tamoxifen injection
90 days
A
B
C
D
Lgr5
tdTomato
A′
B′
C′
D′
E
F
G
H
E′
F′
G′
H′

**Figure A.6. Lgr5-EGFP$^+$ cells in the OB are at different stages of maturation.** (**A**, **B**) A subset of Lgr5-EGFP$^+$ cells (in green) coexpress DCX (red) in both the GL (15%, **A**) and MCL (10%, **B**). Enlarged images within the rectangles are shown in **A'** and **B'**. (**C**, **D**) in the GL, a subset Lgr5-EGFP$^+$/TH$^+$ cells coexpresses DCX (arrowhead, 21%) (**C**) or NeuN (arrowhead, 30%) (**D**). The arrows mark Lgr5-EGFP$^+$/TH$^+$ cells that do not express DCX (**C**) or NeuN (**D**). Scale bars: 20 μm in **B**, and 10 μm in **B'** and **D**.

**Figure A.6.**

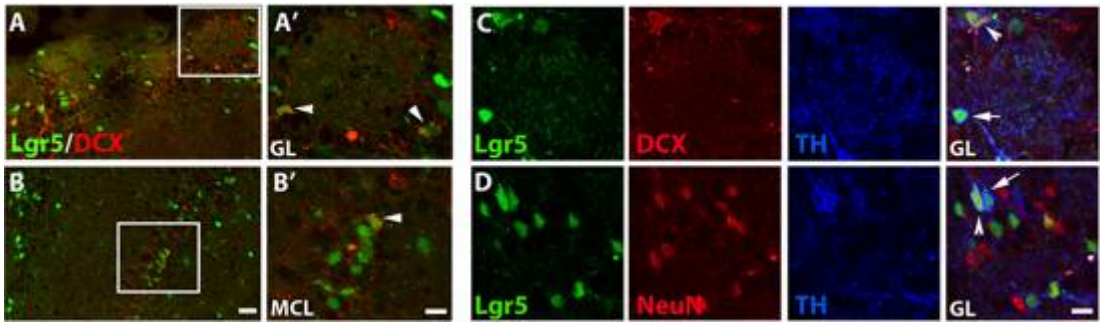

**Figure A.7. Lgr5 expression is independent of sensory inputs.** (**A**) Sensory deprivation did not alter the number of Lgr5-EGFP$^{+}$ cells in the GL (25 ± 2/glomerulus in the open side, n = 24 sections; 26 ± 3/glomerulus in the closed side, n = 24 sections, MCL (24 ± 3 cells/300 µm linear length in the open side, n = 24 sections; 22 ± 3 on the closed side, n = 24 sections, or GCL (25 ± 3 cells/ 100x100 µm$^2$ in the open side, n = 24 sections; 25 ± 4 in the closed side, n = 24 sections). (**B1**-**B3**) The percentage of Lgr5-EGFP$^{+}$/TH / Lgr5-EGFP$^{+}$ cells in the GL decreased in the closed side (**B1**, 35 ± 4%, n = 21 sections) compared to the open side (**B2**, 55 ± 6%, n = 21 sections), data summarized in **B3**. (**C1**-**C3**) The percentage of Lgr5-EGFP$^{+}$5T4$^{+}$ / Lgr5-EGFP$^{+}$ cells in the closed MCL (**C1**, **23** ± 5%, n = 21 sections) decreased compared to the open MCL (**C2**, 39 ± 6%, n = 21 sections), summarized in **C3**. (**D1**-**D5**) Expression of DCX was increased in the closed GL (**D1**, 33 ± 4%, n = 24 sections) and GCL (**D3**, 19 ± 4%, n = 24 sections) compared to the open side (**D2**, 22 ± 3% in GL and **D4**, 11 ± 3% in the GCL, n = 24 sections), summarized in **D5**. Scale bar: 10 µm.

**Figure A.7.**

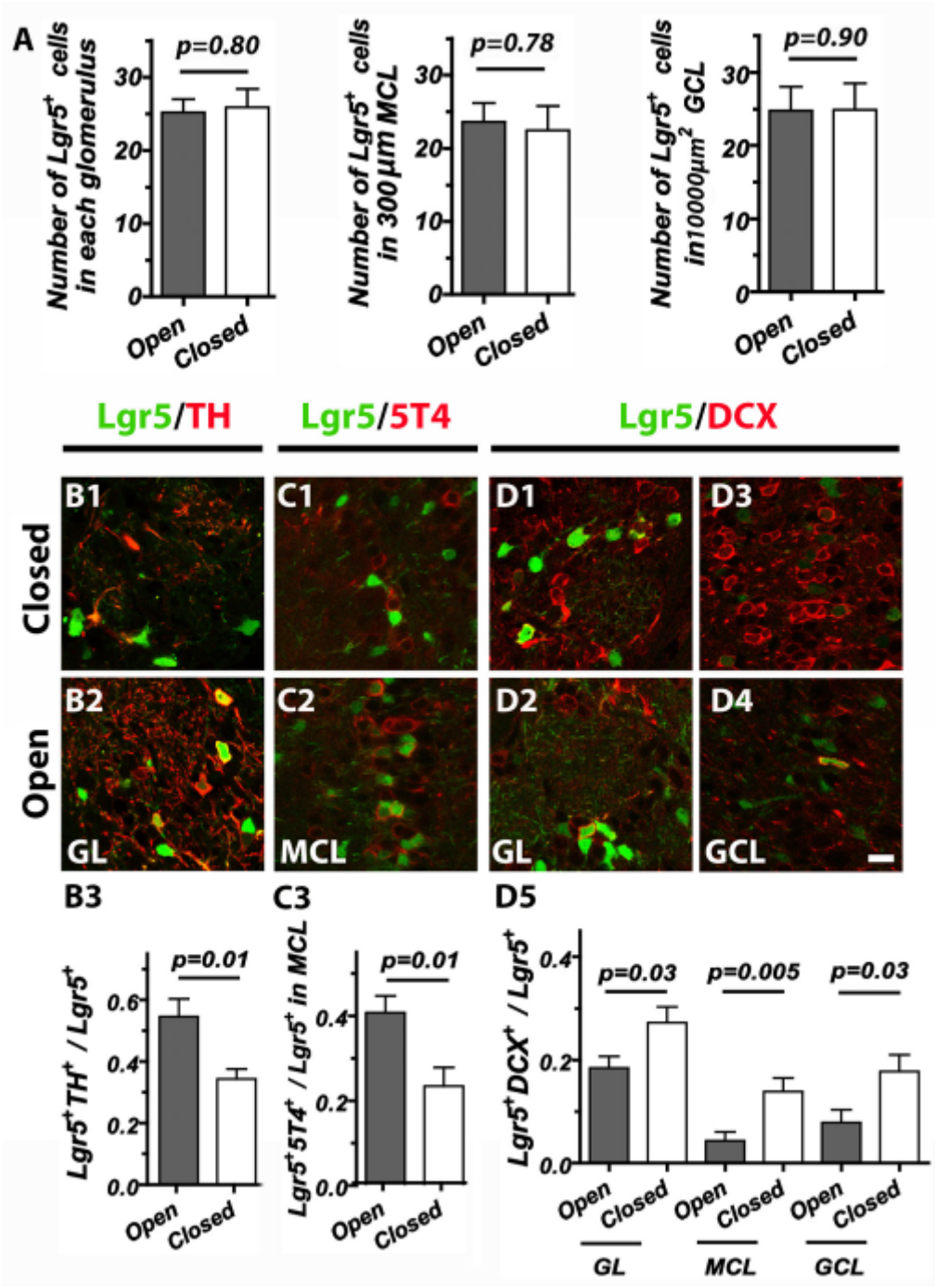
A
Number of Lgr5+ cells in each glomerulus
p=0.80
Number of Lgr5+ cells in 300μm MCL
p=0.78
Number of Lgr5+ cells in10000μm2 GCL
p=0.90
Open
Closed
Lgr5/TH
Lgr5/5T4
Lgr5/DCX
B1
C1
D1
D3
B2
C2
D2
D4
GL
MCL
GL
GCL
B3
C3
D5
Lgr5+TH+ / Lgr5+
Lgr5+5T4+ / Lgr5+ in MCL
Lgr5+DCX+ / Lgr5+
p=0.01
p=0.01
p=0.03
p=0.005
p=0.03
GL
MCL
GCL

**Figure A.8. Whole cell patch clamp recordings reveal the electrophysiological properties of Lgr5-EGFP$^+$ cells in the GL.** (**A**) Fluorescent cells in the GL were observed in OB slices from adult Lgr5-EGFP mice and targeted for whole-cell patch clamp recordings. Scale bar: 50 µm. (**B**) Representative current-clamp recordings from Lgr5-EGFP$^-$ and Lgr5-EGFP$^+$ cells in the GL. These diverse firing patterns were representative of juxtaglomerular neurons. (**C**-**E**) Voltage-clamp recordings ($V_{hold}$, -70 mV) demonstrated that both Lgr5-EGFP$^-$ and Lgr5-EGFP$^+$ cells receive synaptic inputs in the form of excitatory postsynaptic currents (sEPSCs). (**D**) While the frequency of sEPSCs were not different between the two groups (Lgr5-EGFP$^-$, 7.3 ± 1.4 Hz vs Lgr5-EGFP$^+$, 9.1 ± 2.3 Hz), the amplitude (**E**) was significantly higher in Lgr5-EGFP$^+$ (164 ± 30.5 pA, n = 13) compared to Lgr5-EGFP$^-$ cells (93 ± 8.6 pA, n = 17).

**Figure A.8.**

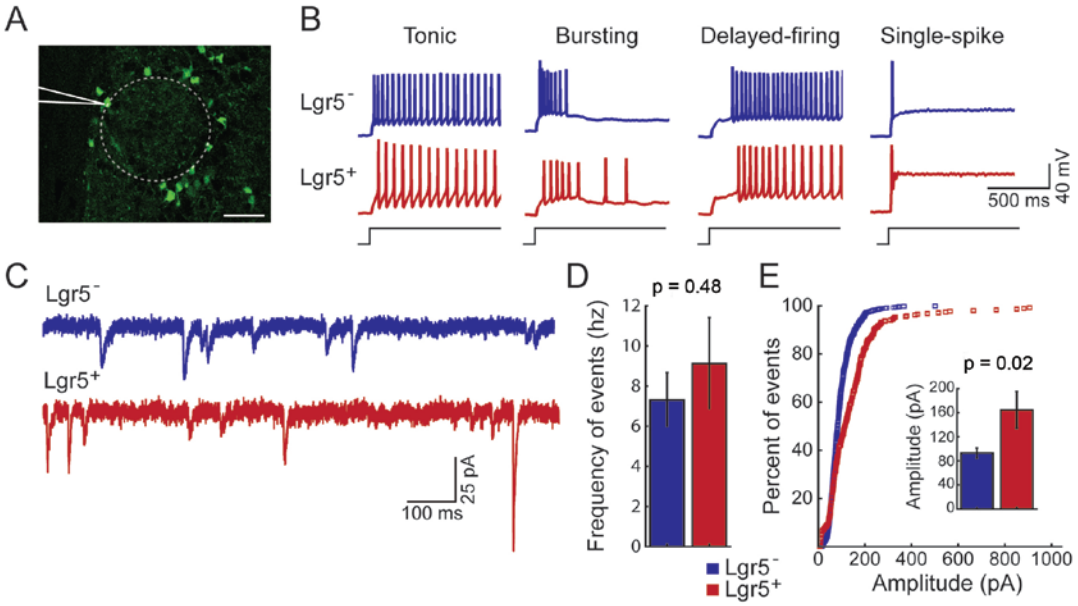
A
B
Tonic
Bursting
Delayed-firing
Single-spike
Lgr5⁻
Lgr5⁺
500 ms
40 mV
C
Lgr5⁻
Lgr5⁺
25 pA
100 ms
D
p = 0.48
Frequency of events (hz)
Lgr5⁻
Lgr5⁺
E
Percent of events
Amplitude (pA)
p = 0.02
Amplitude (pA)

**Figure A.9. R-Spondin 3, a ligand for Lgr5, is expressed in the olfactory bulb**. (**A**) In situ hybridization of R-spondin 3 in the olfactory bulb. Image was taken from the Allen Developing Mouse Brain Atlas. Scale bar: 100 µm. (**B**) Double in situ hybridization using *lgr5* (green) and *R-spondin*-3 (red) riboprobes showed expression of the two genes in the OB. Arrowheads mark co-stained cells. For both (**A**) and (**B**), the results were from one-month old mice. Similar results were obtained from two-month old mice. Scale bar: 20 µm. (**C**) Bath perfusion of R-Spondin 3 did not change the resting membrane potential (RMP), sEPSC frequency or sEPSC amplitude. Each red line connects values pre- and post-application of R-spondin 3 from a single cell. The data for the RMP were obtained from perforated patch clamp while those for sEPSC were from whole-cell patch clamp. Additional cells recorded in perforated patch clamp configuration also showed no alteration is sEPSC frequency and amplitude after R-Spondin 3 application.

**Figure A.9.**

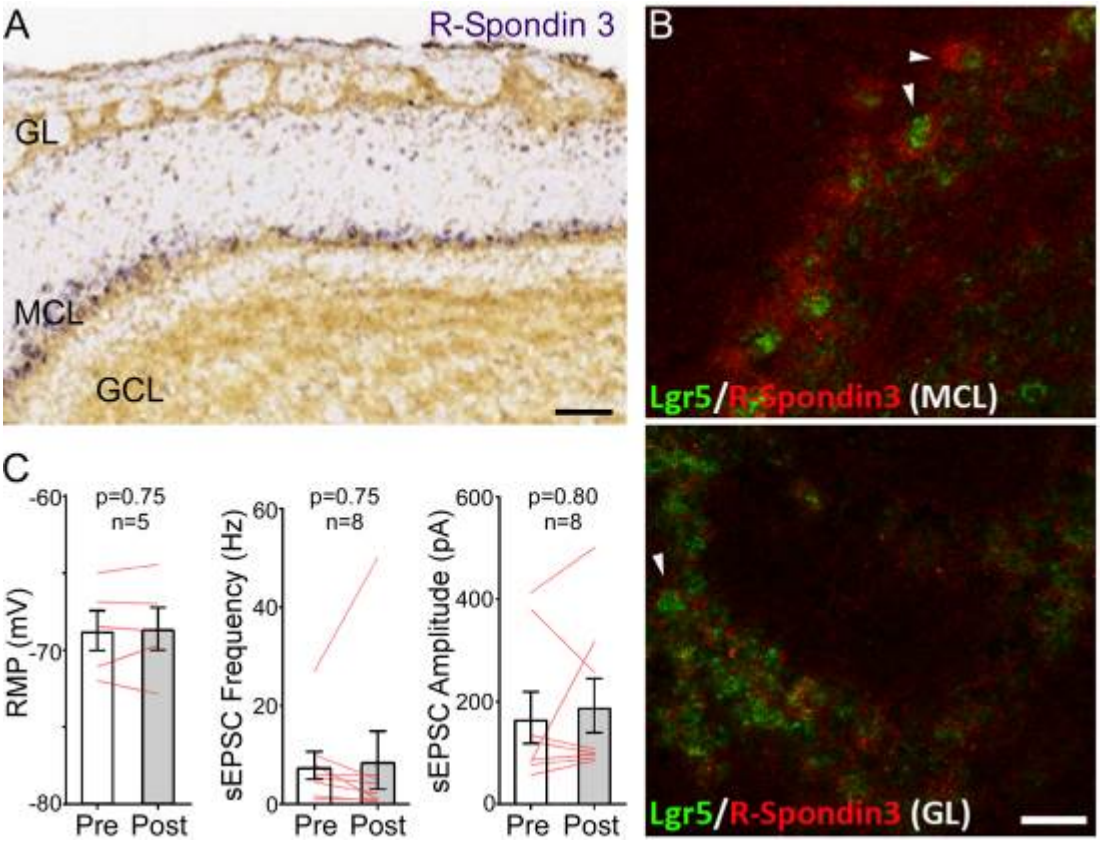
A
R-Spondin 3
GL
MCL
GCL
B
Lgr5/R-Spondin3 (MCL)
Lgr5/R-Spondin3 (GL)
C
RMP (mV)
-60
-70
-80
p=0.75
n=5
Pre Post
sEPSC Frequency (Hz)
60
40
20
0
p=0.75
n=8
Pre Post
sEPSC Amplitude (pA)
600
400
200
0
p=0.80
n=8
Pre Post

## Methods

### *Animals*

Genetically targeted heterozygous Lgr5-EGFP-IRES-cre/ERT2 mice (Jackson Stock No: 008875) harboring a "knock-in" allele that abolishes *Lgr5* gene function and expresses EGFP and CreERT2 fusion protein from the Lgr5 promoter/enhancer elements and Rosa26-floxed STOP-tdTomato mice (Jackson Stock No: 007909) were purchased from Jackson Laboratory. Both male and female mice were used in the study and data from both genders were pooled since no sex differences were evident. All animal and tissue harvesting procedures were approved by the University of Pennsylvania Institutional Care and Use Committee.

For genetic lineage tracing, Lgr5-EGFP-IRES-cre/ERT2 mice were crossed with Rosa26-tdTomato mice. To induce the expression of the reporter gene, a single dose of tamoxifen (Sigma Aldrich, 0.22 mg/g body weight) was injected intraperitoneally at six weeks. Mice were then sacrificed at different time points following induction.

For 5-bromo-2'-deoxyuridine (BrdU) staining, mice were injected with one dose of BrdU (Sigma Aldrich, 50 µg/g body weight) at four weeks and sacrificed 2 hours after injection. For unilateral naris closure experiments, a brief cauterization (~1 s) was performed on one nostril on postnatal day 1 (P1), and mice were examined one month later. Only mice with complete naris occlusion were used for further analysis.

### *Immunohistochemistry*

Mice were deeply anesthetized with intraperitoneal injection of ketamine-xylazine (200/15 mg/kg body weight) before decapitation. The heads were fixed in 4% paraformaldehyde overnight at 4° C, and infiltrated in a series of sucrose solutions before

being embedded in OCT. The frozen tissues were cut into 20 μm coronal sections on a cryostat. After antigen retrieval in a 95° C water bath for 10 min (followed by 10 min in 2N HCl at 37° C in cases of BrdU detection). Tissue sections were blocked for 60 min in 0.3% Triton X-100 in phosphate buffered saline with 5% bovine serum albumin and then incubated at 4° C with primary antibodies overnight. The primary antibodies were goat anti-Sox2 (sex determining region Y-box2, 1:100, Santa Cruz), mouse anti-Ki67 (1:100, BD), mouse anti-Nestin (neuroectodermal stem cell marker, 1:200, Millipore), goat anti-BrdU (1:1000, Chemicon), goat anti-glial fibrillary acidic protein (GFAP, 1:1000, Sigma), mouse anti-NeuN (1:500, Millipore), rabbit anti-tyrosine hydroxylase (TH, 1:500, Millipore), goat anti-glutamic acid decarboxylase 65 (GAD65, 1:100, Abcam), mouse ant-calbindin (CB, 1:500, Sigma), mouse anti-calretinin (CR, 1:500, Millipore), sheep anti-5T4 oncofetal trophoblast glycoprotein (1:200, R&D), goat anti-DCX (1:200, Santa Cruz), or mouse anti-Lgr5 (1:100, OriGene). The secondary antibodies included donkey anti-goat 568, dockey anti-mouse-568, donkey anti-rabbit-568, donkey anti-rabbit 647, donkey anti-sheep 647, donkey anti-mouse 488, and donkey anti-goat 633). Tissues were mounted in VectaShield (Vector Laboratories) and fluorescent images were taken under a SP5/Leica confocal microscope with LAS AF lite software.

***Patch Clamp recordings***

Adult Lgr5-EGFP-IRES-cre/ERT2 mice (4-12 weeks old, either gender) were deeply anesthetized with ketamine/xylazine and decapitated. The brain was dissected out and immediately placed in ice-cold Ringer's solution containing (in mM) 124 NaCl, 3 KCl, 1.3 $MgSO_4$, 2 $CaCl_2$, 26 $NaHCO_3$, 1.25 $NaH_2PO_4$, 5.5 glucose and 4.47 sucrose; osmolality ~305 mOsm and pH 7.4 bubbled continuously with 95% $O_2$ balance $CO_2$.

Coronal slices (300 µm) were cut using a Leica VT 1200S vibratome. Slices were incubated in oxygenated Ringer's solution for 1 h at room temperature before use. For recordings, slices were transferred to a recording chamber and continuously perfused with oxygenated Ringers. $Td^+$ cells were visualized using an Olympus 40X water-immersion objective on a BX51WI upright microscope equipped with epifluorescence. Recording pipettes were made from borosilicate glass with a Flaming-Brown puller (Sutter Instruments). The tip resistance was 5-10 MΩ and the pipette solution contained (in mM) 120 K-gluconate, 10 KCl, 2 MgATP, 0.5 NaGTP, 20 HEPES, 0.5 EGTA, and 10 phosphocreatine di(tris) salt at a pH of 7.4 and osmolality of 300 mOsm. Perforated patch clamp recordings were performed in a subset of cells by adding gramicidin (Sigma Aldrich) in the pipette. Gramicidin was first dissolved in dimethyl sulfoxide (DMSO) to a concentration of 2.5 µg/ml and then diluted in the pipette solution. Before backfilling the gramicidin-containing solution, the electrode tip was pre-loaded with gramicidin-free pipette solution. Reductions in access resistance were monitored and experiments begun when the resistance was stabilized at 50-90 Mohm. Mouse recombinant R-spondin 3 (R & D systems product No: 4120-RS-025/CF) was diluted in Ringer's solution at a concentration of 100 ng/ml (3.5 mM).

***In situ hybridization***

Digoxigenin (DIG) or fluorescein (FITC) labeled riboprobes were synthesized using a DIG or FITC RNA labeling kit (Roche). The template for *lgr5*, vesicular glutamate transporter 1 (*vglut1*), and R-spondin 3 genes were amplified from mouse OB cDNA by PCR and subcloned into vector pGEM-T Easy (A1360, Promega).

Double fluorescent in situ hybridization (FISH) was performed. Briefly, sections were hybridized with 1-2 ng/µl of DIG and FITC labeled riboprobes diluted in hybridization buffer containing 50% formamide, 5XSSC, 0.3 mg/ml yeast tRNA, 100 µg/ml heparin, 1X Dehardt's, 0.1% Tween-20, 0.1% CHAPS, 5 mM EDTA in RNase free $H_2O$ overnight under parafilm at 62° C. The sections were incubated in anti-FITC-POD (1:100 in 0.5% Blocking Reagent, Roche product no: 1142634910) overnight at 4° C. FITC riboprobes were developed using the TSA Plus system (Perkin Elmer). Next, slides were incubated overnight at 4° C with AP-conjugated anti-DIG antibody (1:500 in PBT and 20% lamb serum). DIG-labeled riboprobes were developed using HNPP/Fast Red TR system (Roche). Slides were then rinsed in PBS and mounted with VectaShield.

***Nissl Staining***

NeuroTrace 530/615 red fluorescent Nissl stain (ThermoFisher) was used to stain Nissl substance in OB sections for identifying neuronal cells. NeuroTrace stain was diluted 1:200 in PBS. The sections were covered with NeuroTrace stain and incubated for 20 min at room temperature then mounted in VectaShield.

***Data Analysis***

*Cell counting*: To quantify cell number in different layers of the OB a total of 16 counting squares in a single layer where chosen at random from each section. Unless otherwise specified, for each percentage including no coexpression (0%), a total of 300 to 1000 cells from at least 3 sections of three different mice were counted and included. Juxtaglomerular cells were defined as cells on the edge of each glomerulus. Counting was carried out by experimenters blinded to the experimental design. Averaged data were

derived from all three experimental animals used per group and are expressed as mean ± SEM.

*Statistical analysis*: In naris closure experiments paired Student's *t* tests were performed between the open and occluded sides. For the effects of R-spondin 3 on Lgr5-EGFP$^{+}$ cells paired Student's *t* tests were performed between pre- and post-application conditions. We used unpaired Student's *t* tests in further tests of the electrophysiological differences between Lgr5-EGFP$^{+}$ and Lgr5-EGFP$^{-}$ cells. All statistical analysis was performed in GraphPad Prizm 7 (San Diego, CA) using parametric tests since the data were considered normally distributed (Shapiro-Wilk normality test) with equal variance between groups.

## References


Baker H, Morel K, Stone DM, Maruniak JA (1993) Adult naris closure profoundly reduces tyrosine hydroxylase expression in mouse olfactory bulb. Brain Res 614:109-116.

Banerjee A, Marbach F, Anselmi F, Koh MS, Davis MB, da Silva PG, Delevich K, Oyibo HK, Gupta P, Li B, Albeanu DF (2015) An Interglomerular Circuit Gates Glomerular Output and Implements Gain Control in the Mouse Olfactory Bulb. Neuron 87:193-207.

Barker N, van Es JH, Kuipers J, Kujala P, van den Born M, Cozijnsen M, Haegebarth A, Korving J, Begthel H, Peters PJ, Clevers H (2007) Identification of stem cells in small intestine and colon by marker gene Lgr5. Nature 449:1003-1007.

Barker N, Rookmaaker MB, Kujala P, Ng A, Leushacke M, Snippert H, van de Wetering M, Tan S, Van Es JH, Huch M, Poulsom R, Verhaar MC, Peters PJ, Clevers H (2012) Lgr5(+ve) Stem/Progenitor Cells Contribute to Nephron Formation during Kidney Development. Cell Rep 2:540-552.

Barker N, Huch M, Kujala P, van de Wetering M, Snippert HJ, van Es JH, Sato T, Stange DE, Begthel H, van den Born M, Danenberg E, van den Brink S, Korving J, Abo A, Peters PJ, Wright N, Poulsom R, Clevers H (2010) Lgr5(+ve) Stem Cells Drive Self-Renewal in the Stomach and Build Long-Lived Gastric Units In Vitro. Cell Stem Cell 6:25-36.

Batista-Brito R, Close J, Machold R, Fishell G (2008) The distinct temporal origins of olfactory bulb interneuron subtypes. J Neurosci 28:3966-3975.

Bramhall NF, Shi F, Arnold K, Hochedlinger K, Edge AS (2014) Lgr5-positive supporting cells generate new hair cells in the postnatal cochlea. Stem Cell Reports 2:311-322.

Brown JP, Couillard-Despres S, Cooper-Kuhn CM, Winkler J, Aigner L, Kuhn HG (2003) Transient expression of doublecortin during adult neurogenesis. Journal of Comparative Neurology 467:1-10.

Carmon KS, Gong X, Lin QS, Thomas A, Liu QY (2011) R-spondins function as ligands of the orphan receptors LGR4 and LGR5 to regulate Wnt/beta-catenin signaling. P Natl Acad Sci USA 108:11452-11457.

Cave JW, Baker H (2009) Dopamine Systems in the Forebrain. Development and Engineering of Dopamine Neurons 651:15-35.

Chen MF, Tian SH, Yang XL, Lane AP, Reed RR, Liu HJ (2014) Wnt-Responsive Lgr5(+) Globose Basal Cells Function as Multipotent Olfactory Epithelium Progenitor Cells. J Neurosci 34:8268-8276.

de Lau W, Peng WC, Gros P, Clevers H (2014) The R-spondin/Lgr5/Rnf43 module: regulator of Wnt signal strength. Gene Dev 28:305-316.

de Lau W, Barker N, Low TY, Koo BK, Li VS, Teunissen H, Kujala P, Haegebarth A, Peters PJ, van de Wetering M, Stange DE, van Es JE, Guardavaccaro D, Schasfoort RB, Mohri Y, Nishimori K, Mohammed S, Heck AJ, Clevers H (2011) Lgr5 homologues associate with Wnt receptors and mediate R-spondin signalling. Nature 476:293-297.

de Visser KE, Ciampricotti M, Michalak EM, Tan DW, Speksnijder EN, Hau CS, Clevers H, Barker N, Jonkers J (2012) Developmental stage-specific contribution of LGR5(+) cells to basal and luminal epithelial lineages in the postnatal mammary gland. J Pathol 228:300-309.

Dickins EM, Salinas PC (2013) Wnts in action: from synapse formation to synaptic maintenance. Front Cell Neurosci 7:162.

Glinka A, Dolde C, Kirsch N, Huang YL, Kazanskaya O, Ingelfinger D, Boutros M, Cruciat CM, Niehrs C (2011) LGR4 and LGR5 are R-spondin receptors mediating Wnt/beta-catenin and Wnt/PCP signalling. EMBO Rep 12:1055-1061.

Hirata-Tominaga K, Nakamura T, Okumura N, Kawasaki S, Kay EP, Barrandon Y, Koizumi N, Kinoshita S (2013) Corneal endothelial cell fate is maintained by LGR5 through the regulation of hedgehog and Wnt pathway. Stem Cells 31:1396-1407.

Imamura F, Nagao H, Naritsuka H, Murata Y, Taniguchi H, Mori K (2006) A leucine-rich repeat membrane protein, 5T4, is expressed by a subtype of granule cells with dendritic arbors in specific strata of the mouse olfactory bulb. Journal of Comparative Neurology 495:754-768.

Jaks V, Barker N, Kasper M, van Es JH, Snippert HJ, Clevers H, Toftgard R (2008) Lgr5 marks cycling, yet long-lived, hair follicle stem cells. Nat Genet 40:1291-1299.

Kiyokage E, Pan YZ, Shao Z, Kobayashi K, Szabo G, Yanagawa Y, Obata K, Okano H, Toida K, Puche AC, Shipley MT (2010) Molecular identity of periglomerular and short axon cells. The Journal of neuroscience : the official journal of the Society for Neuroscience 30:1185-1196.

Kosaka T, Kosaka K (2011) "Interneurons" in the olfactory bulb revisited. Neurosci Res 69:93-99.

Kosaka T, Komada M, Kosaka K (2008) Sodium channel cluster, beta IV-spectrin and ankyrinG positive "hot spots" on dendritic segments of parvalbumin-containing neurons and some other neurons in the mouse and rat main olfactory bulbs. Neurosci Res 62:176-186.

Lepousez G, Nissant A, Lledo PM (2015) Adult neurogenesis and the future of the rejuvenating brain circuits. Neuron 86:387-401.

Leushacke M, Ng A, Galle J, Loeffler M, Barker N (2013) Lgr5(+) gastric stem cells divide symmetrically to effect epithelial homeostasis in the pylorus. Cell Rep 5:349-356.

Liu S, Puche AC, Shipley MT (2016) The Interglomerular Circuit Potently Inhibits Olfactory Bulb Output Neurons by Both Direct and Indirect Pathways. The Journal of neuroscience : the official journal of the Society for Neuroscience 36:9604-9617.

Lledo PM, Merkle FT, Alvarez-Buylla A (2008) Origin and function of olfactory bulb interneuron diversity. Trends Neurosci 31:392-400.

McQuiston AR, Katz LC (2001) Electrophysiology of interneurons in the glomerular layer of the rat olfactory bulb. J Neurophysiol 86:1899-1907.

Miller TE, Wang J, Sukhdeo K, Horbinski C, Tesar PJ, Wechsler-Reya RJ, Rich JN (2014) Lgr5 Marks Post-Mitotic, Lineage Restricted Cerebellar Granule Neurons during Postnatal Development. PLoS One 9:e114433.

Ming GL, Song H (2011) Adult neurogenesis in the mammalian brain: significant answers and significant questions. Neuron 70:687-702.

Moberly AH, Schreck M, Bhattarai JP, Zweifel LS, Luo W, Ma M (2018) Olfactory inputs modulate respiration-related rhythmic activity in the prefrontal cortex and freezing behavior. Nat Commun 9:1528.

Ng A, Tan S, Singh G, Rizk P, Swathi Y, Tan TZ, Huang RYJ, Leushacke M, Barker N (2014) Lgr5 marks stem/progenitor cells in ovary and tubal epithelia. Nat Cell Biol 16:745-U342.

Parrish-Aungst S, Shipley MT, Erdelyi F, Szabo G, Puche AC (2007) Quantitative analysis of neuronal diversity in the mouse olfactory bulb. Journal of Comparative Neurology 501:825-836.

Plaks V, Brenot A, Lawson DA, Linnemann JR, Van Kappel EC, Wong KC, de Sauvage F, Klein OD, Werb Z (2013) Lgr5-Expressing Cells Are Sufficient and Necessary for Postnatal Mammary Gland Organogenesis. Cell Rep 3:70-78.

Shi FX, Kempfle JS, Edge ASB (2012) Wnt-Responsive Lgr5-Expressing Stem Cells Are Hair Cell Progenitors in the Cochlea. J Neurosci 32:9639-9648.

Shi FX, Hua LX, Edge ASB (2013) Generation of hair cells in neonatal mice by beta-catenin overexpression in Lgr5-positive cochlear progenitors. P Natl Acad Sci USA 110:13851-13856.

Sukhdeo K, Koch CE, Miller TE, Zhou H, Rivera M, Yan K, Cepko CL, Lathia JD, Rich JN (2014) The Lgr5 transgene is expressed specifically in glycinergic amacrine cells in the mouse retina. Exp Eye Res 119:106-110.

Sun XF, Terakawa J, Clevers H, Barker N, Daikoku T, Dey SK (2014) Ovarian LGR5 is critical for successful pregnancy. Faseb J 28:2380-2389.

Tian H, Biehs B, Warming S, Leong KG, Rangell L, Klein OD, de Sauvage FJ (2011) A reserve stem cell population in small intestine renders Lgr5-positive cells dispensable. Nature 478:255-U148.

Whitesell JD, Sorensen KA, Jarvie BC, Hentges ST, Schoppa NE (2013) Interglomerular Lateral Inhibition Targeted on External Tufted Cells in the Olfactory Bulb. J Neurosci 33:1552-+.

Whitman MC, Greer CA (2009) Adult neurogenesis and the olfactory system. Prog Neurobiol 89:162-175.

Yee KK, Li Y, Redding KM, Iwatsuki K, Margolskee RF, Jiang PH (2013) Lgr5-EGFP Marks Taste Bud Stem/Progenitor Cells in Posterior Tongue. Stem Cells 31:992-1000.

Yoshihara S, Takahashi H, Nishimura N, Naritsuka H, Shirao T, Hirai H, Yoshihara Y, Mori K, Stern PL, Tsuboi A (2012) 5T4 glycoprotein regulates the sensory input-dependent development of a specific subtype of newborn interneurons in the mouse olfactory bulb. The Journal of neuroscience : the official journal of the Society for Neuroscience 32:2217-2226.